Characterization of Micro-Plasma Wire Arc Additive Manufacturing: Anisotropy and Layer Height Investigation

by

Rami Hakim

A thesis
presented to the University of Waterloo
in fulfillment of the
thesis requirement for the degree of
Master of Applied Science
in
Mechanical and Mechatronics Engineering

Waterloo, Ontario, Canada, 2024

Author's Declaration

This thesis consists of material all of which I authored or co-authored: see Statement of Contributions included in the thesis. This is a true copy of the thesis, including any required final revisions, as accepted by my examiners.

I understand that my thesis may be made electronically available to the public.

Statement of Contributions

Chapter 4 from this thesis has been adopted from the journal "Mechanical Anisotropy and Microstructural Characterization of AISI 316LSi Stainless Steel using Micro-Plasma Directed Energy Deposition" published in "Welding in the World" in December 2023, which I co-authored with my colleagues Nazmul Huda, Emanuel Santos, Paulo Assuncao, and my supervisor Professor Adrian Gerlich. In this paper, I was responsible for the experimental work, data analysis, and writing of the paper. Nazmul Huda was responsible for setting up the electron back-scatter diffusion analysis and extracting its results as well as plotting the hardness profiles in Origin. Emanuel Santos and Paulo Assuncao provided guidance with initial parameters of obtaining good bead fusion and dimensions. Adrian Gerlich provided supervision of the work and reviewing and editing the paper.

Nazmul Huda also aided with mounting and polishing of the titanium samples deposited at amplitudes of 100 W with frequency ranges of 100-600 Hz and 4 W with frequency ranges of 50-100 Hz, highlighted in Chapter 5.

Emanuel Santos helped with the development of the MATLAB code regarding the gain and max speed graphs of the automatic voltage control, presented in Appendix C.

Douglas Hirst aided with testing the wrought steel samples while Nivas Ramachandiran aided with vibration polishing of titanium samples.

Abstract

Directed energy deposition describes the process of deposition of molten metal in wire or powder form with a focused energy beam source in a layer-by-layer fashion to create a final part. The use of an arc as heat source and wire as feedstock material for directed energy deposition, also known as wire arc additive manufacturing, has become increasingly popular in recent years due to its high productivity, high versatility, availability, cost, and its ability to produce large and complex parts.

However, due to the additive nature of the process and the high heat input involved, anisotropy is a recurring problem arising in printed parts, which leads to different tensile properties in the travel and build directions. Hence, the first section of this work looks into the mechanical properties and microstructures of a thin-walled AISI316LSi austenitic stainless-steel component fabricated by wire arc additive manufacturing using the micro-plasma arc welding process, which is a low heat input process. While properties were mainly uniform, the effect of anisotropy was found to have a significant influence on the modulus of elasticity, with values ranging from 79.5±6.8 GPa along the build direction to 105.2±20.7 GPa in the travel direction. This difference was found to be due to the strong preferential orientation of grains during solidification along the direction corresponding to the build direction, which was also confirmed by electron back scatter diffraction. This was also confirmed by theoretical calculations.

The second portion of the work deals with the investigation of the effect of vibratory weld conditioning on the grain size for titanium and stainless-steel layers using the current process. This was motivated by the need to break down the orientation of columnar grains witnessed and transform them into random equiaxed grains. Tests were conducted through the deposition of five layers for each material and the use of a shaker device and a signal generator, which was used to conduct tests based on

square waves with different amplitudes and frequency ranges. Results revealed that fine grains were achieved when close to the substate, while only frequency was found to have a significant effect on secondary dendrite arm spacing and grain size for stainless-steel and titanium, respectively.

The final section of this work deals with correcting layer height deviations, which arise as a result of the heat accumulation of the wire arc additive manufacturing process. The performance of the automatic voltage control, which automatically adjusts the Z-position of the torch during deposition based on arc voltage measured, was initially investigated based on gain and correction speed. Results revealed very high correlations between Z-position and bead height, particularly for a gain of 1.0 (R=0.96) and a max speed of 65 mm/min (0.995). This proved the high reliability of the automatic voltage control when maintaining the voltage measured with the desired voltage but still does not account for surface inconsistencies. Hence, layer height deviations were measured and corrected with an accuracy of 0.03 mm through the modification of the wire feed speed, obtained by determining the exact volume of material added during deposition for different wire feed speeds. Also, in this section, optimal bead overlay parameters were determined based on best fusion and flat surface, revealing to be 15 % for substate welding and 25 % for subsequent layer deposition.

Acknowledgments

First, I would like to greatly thank my supervisor Professor Adrian Gerlich for guiding me throughout my studies. He has always given time to make sure we meet every week and provided me with many opportunities such as coordinating the CAMJ seminar and working as the lab instructor for his courses all throughout my degree. His patience and amazing supervision are admirable, always maintaining composure and encouragement in the face of some unusual setbacks during my studies. I am eternally grateful for his guidance and support, which have helped me grow and made me love the research and the welding industry.

I would also like to give special thanks to my former colleague, Nazmul Huda, and my current colleagues, Emanuel Santos, and Paulo Assuncao, who have also been instrumental in my development and providing me with training, guidance, and help when I needed it. I also extend my thanks to my current colleagues Hanwen Yang, Nivas Ramachandiran, and Thomas Burchat who have provided me with many valuable insights and support and with whom I have had the great pleasure of working with. Many thanks as well to all CAMJ professors and members who have been part of my life and whom I have had the privilege of meeting and discussing with.

Many thanks to all faculty of engineering staff, technicians, and lab managers for their prompt disposition to helping with any issues, training, and sample preparation, particularly Douglas Hirst, James Farnsworth, Phil Laycock, Yuquan Ding, Les Ankucza, and Ryan Cadeau. Their help has been amazing, and I greatly appreciate it.

I would also like to thank my former professor Ali Ammouri from the Lebanese American University for providing me with great help during my undergrad.

Dedication

I would like to dedicate this thesis to my dear parents, Nizar, and Randa, and to my sister Carine, who have always supported me and stood by my side. I would also like to dedicate this thesis to my dear friends and family who have supported me during this journey.

Table of Contents

List of Figures

List of Tables

List of Abbreviations

AFSM	Additive Friction Stir Manufacturing
AISI	American Iron and Steel Institute
AM	Additive Manufacturing
ASTM	American Society for Testing and Materials
AVC	Automatic Voltage Control
DCEN	Direct Current Electrode Negative
DCEP	Direct Current Electrode Positive
DED	Directed Energy Deposition
DIC	Digital Image Correlation
EBSD	Electron Back Scatter Diffraction
FDM	Fused Deposition Modelling
GB	Grain Boundary
GMAW	Gas Metal Arc Welding
GTAW	Gas Tungsten Arc Welding
HAZ	Heat Affected Zone
IPF	Inverse Pole Figure
LAWS	Liburdi Automatic Welding System
LPBF	Laser Powder Bed Fusion
LVST	Laser Vision Seam Tracking
MPAW	Micro-Plasma Arc Welding
NTSD	Nozzle to surface distance
PAW	Plasma Arc Welding
RZ	Reheated Zone
SDAS	Secondary Dendrite Arm Spacing
SLS	Selective Laser Sintering
TIG	Tungsten Inert Gas

TS	Torch Speed
TST	Through Seam Tracking
VSR	Vibration Stress Relief
VST	Vision Seam Tracking
VWC	Vibratory Weld Conditioning
WAAM	Wire Arc Additive Manufacturing
WFS	Wire Feed Speed

Chapter 1
Introduction

1.1 History of the Manufacturing Sector

The history of the manufacturing sector can be traced back to the earliest civilizations, in a period characterized by artisan handicrafts and simple methods for the production of goods [1]. However, the significant breakthrough that was made in terms of manufacturing methods and initiated the technological advancements seen in the present time came with the Industrial Revolution, dating back to the 18th century. This was a period marked by rapid industrialization and the mechanization of the production process, replacing manual labor with machines powered by water and steam [2]. During the 19th century, the manufacturing industry experienced further growth and transformation during the Second Industrial Revolution, as innovations such as the steam engine, the power loom, and the Bessemer process revolutionized the production of steel machinery [3]. This period also saw the ascent of mass production, through the use of assembly lines powered by electricity [4]. In the mid-20th century, further advancements occurred with the development of automation in the production sector through the use of robots, computers, and electronics [4]. The introduction of automation marked a significant shift towards efficient manufacturing and laid the foundation for the current trend towards Industry 4.0 and the Internet of Things.

Today, the manufacturing industry continues to evolve and adapt to changing market demands, globalization, and technological innovations. The integration of new technologies such as additive manufacturing (AM), artificial intelligence, and the Internet of Things is leading to more efficient and sustainable production processes and is shaping the future of the industry.

1.2 Additive Manufacturing

AM, also known as 3D printing, describes the process of building a part through the consolidation of material in a layer-by-layer fashion based on a computer drawing. AM can be traced back to the mid-1980s, when the first patent for a rapid prototyping system was filed [5]. This was quickly followed with the invention of fused deposition modelling (FDM) and selective laser sintering (SLS), the latter using a laser as heat source to fuse small particles of ceramics, metals, or ceramics creating 3D objects.

Over the past few decades, the field of AM has experienced significant advancements, as new materials, processes, and technologies have been developed and adopted such as the creation of the first 3D-printed tissue in 1999 [5], which was a breakthrough in the medical field and paved the way for the creation of transplantable organs using 3D printing.

In recent years, AM has gained a lot of attention for fabrication of commercial components for various industries and is increasingly becoming a popular choice among industries because of its various advantages versus conventional subtractive manufacturing methods such as machining. Along with its ability to handle a wide spectrum of materials from metals, polymers, and ceramics, AM offers the ability to produce complex shapes with novel functionality, along with unmatchable accuracy, repeatability and resolution which make it invaluable to the manufacturing sector [6]. *Figure 1-1a* and *Figure 1-1b* show some of the complex components that can be achieved by laser powder bed fusion. Employing AM also enable reduced manufacturing [7] , better buy-to-fly ratio, and reduced process time. Hence, AM parts can be found in many industries including aerospace [8] [9], marine [9], automotive [8], and medical [8]. A study on the forecasted market trends of the global aerospace AM market has shown that the aerospace industry will remain to be the major contributor to the AM market even following the impact caused by COVID-19 [10]. This is due to the large cost savings achieved when implementing AM for titanium alloys for aerospace components, due to their high strength-to-

weight ratio and inherently high material cost especially when employing subtractive manufacturing technologies [6].

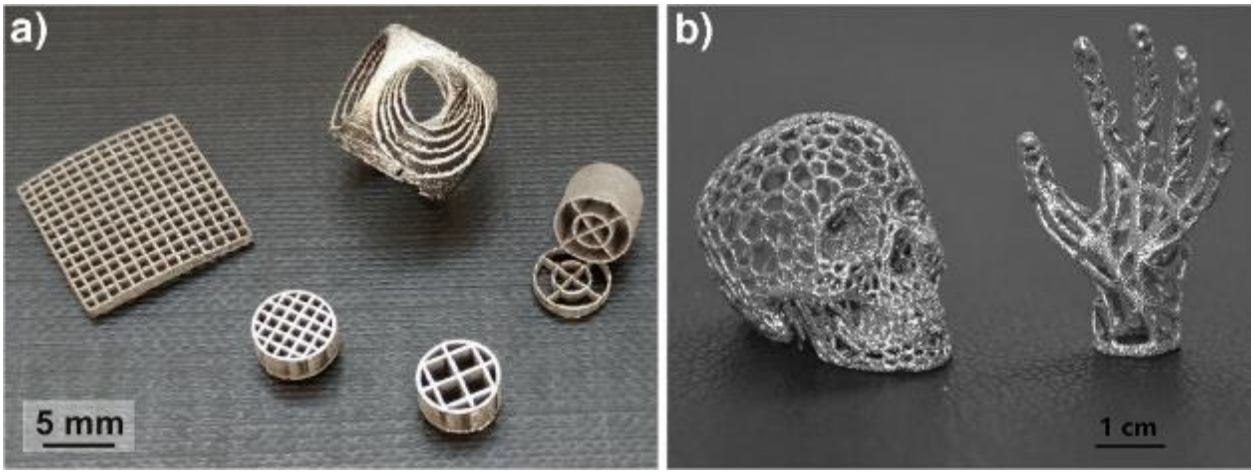

Figure 1-1: Complex components fabricated by laser powder bed fusion [11]

Among the several AM categories to produce metal components, directed energy deposition (DED) is one that uses a heat source to melt a powder or wire that is externally fed as filler metal. Wire arc additive manufacturing (WAAM) is a type of DED process that uses arc welding techniques for the production of 3D printed parts. WAAM typically involves a multi-axis welding robot that deposits material along the build direction from an external wire feeding device, both of which are controlled by the computer, as shown in *Figure 1-2*. *Figure 1-3a* and *Figure 1-3b* highlight large and complex parts fabricated by WAAM.

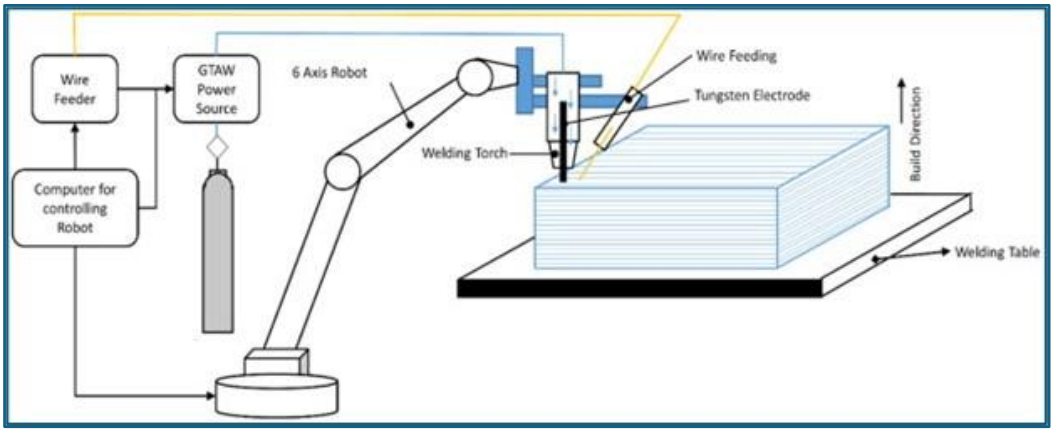

Figure 1-2: Basic overview of the WAAM process [12]

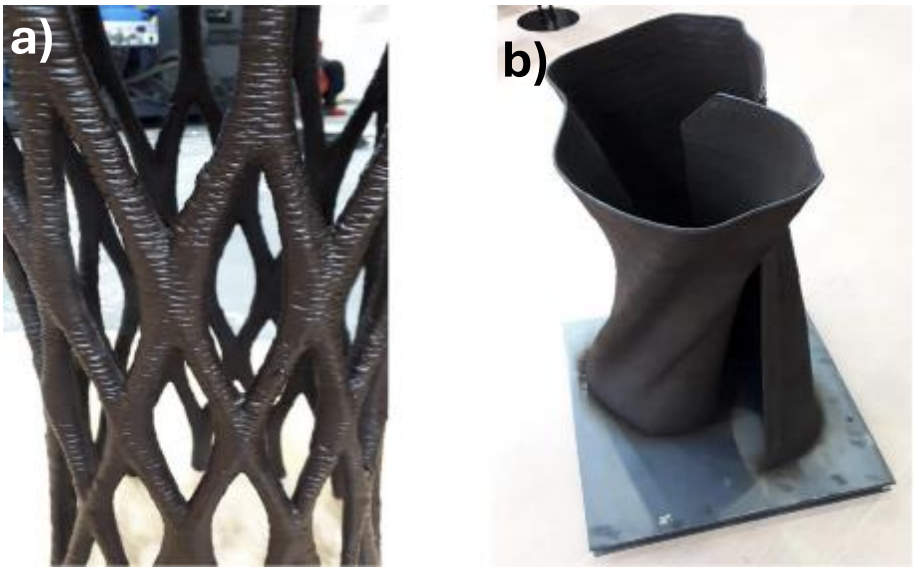

Figure 1-3: Complex large components fabricated by WAAM [11]

1.3 Motivation

The use of arc welding processes for the purpose of AM has garnered increasing attention in recent years, particularly due to its ability to produce large and complex components, high deposition rates and relatively low cost compared to other AM processes based on laser melting of powders. However, the high heat input combined with the heat accumulation associated with WAAM is a problem that affects the geometry of the final component, causing distortion in the desired part. Furthermore, the heat accumulation present in WAAM causes anisotropy within the finished part, with mechanical properties and microstructures significantly different in the travel direction compared to the build direction. This is particularly common for arc welding processes with high heat input such as gas metal arc welding. Hence, the use of a low heat input source for WAAM is worth investigating to analyze the effect of anisotropy in printed components. Significantly lower heat input can be applied using micro-plasma arc welding (MPAW), where electrode current is in the range of 30 A, resulting in more control of the applied heat, less spatter, and higher overall accurate bead geometry. Thus, this process was used for the purposes of this research work.

Despite the low heat input associated with the MPAW process, geometrical inaccuracies within the final generated part will still arise as a result of the heat accumulation. This is particularly due to deviations within the height of individual layers, which ultimately affect the final part. Thus, the need for the development of control strategies for the maintenance of a constant layer height is crucial for proper part generation, thereby greatly aiding in the commercialization of wire arc additive technologies in the manufacturing sector. While layer height can be predicted by modifying process parameters, small deviations in height can still exist due to the additive nature of the molten metal deposition process. That is why this research also focuses on the investigation of the automatic voltage control (AVC) performance for the MPAW process as well as looking into manually modifying specific parameters to have better control over part geometry.

Furthermore, some previous work also focused on the concept of vibratory weld conditioning (VWC), where vibration is applied to the substrate throughout the welding process. This procedure was found to produce finer grain sizes, thereby providing an improvement in mechanical properties. This technique was previously investigated for some welding processes particularly for aluminum. The current research work also focuses on the effect of vibration for titanium and stainless-steel layers using MPAW. This was motivated by the need for a reduction in columnar grains and breaking them down into finer equiaxed grains, ultimately leading to a reduction in anisotropy associated with the WAAM process.

1.4 Objectives

The primary objective of this research is to investigate the effect of anisotropy in a 3D printed wall using the WAAM process with MPAW. The secondary objective is to evaluate parameters to correct deviations in layer geometry through suitable variation of the deposition parameters, as well as to obtain

the optimal overlap parameters for bead-on plate deposition of multiple layers. The final objective is to investigate the effect of VWC on titanium and stainless-steel layers by inducing various frequencies and amplitudes in the melt pool. These were achieved through the experiments highlighted below:

1. The first objective was achieved through building a 130 mm high wall using the WAAM process based on MPAW and investigating microstructures and mechanical properties.
2. The second objective was achieved with starts and stops induced during the deposition for the purpose of creating gaps within the layer as well as obtaining accurate data of volume of material added according to the wire feed speed (WFS).
3. The third objective was achieved through investigation of the microstructures of different deposited layers to look for any potential refinement of grains corresponding to changes in amplitude and frequency.

Chapter 2
Literature Review

2.1 Plasma Arc Welding

2.1.1 Principle of PAW

Plasma is the state of matter that is formed through superheating a gas, to a temperature where electrons detach from the atoms, thus forming an ionized gas [13]. Plasma arc welding (PAW) is an arc welding process that uses a constricted plasma arc to heat, melt, and deposit a metal wire onto a metal base plate, as shown in *Figure 2-1b* [14]. The arc is established between the nozzle and the workpiece after the orifice or plasma gas is ionized due to the heating of the electrode by the current passing through it. The process is similar to gas tungsten arc welding (GTAW) in that both use a non-consumable tungsten electrode. The main difference lies in the placement of the electrode, where it is enclosed inside the nozzle in PAW (*Figure 2-1b*) while in GTAW, it partially sticks out (*Figure 2-1a*). The enclosure of the electrode within the nozzle gives the possibility of achieving very high-power per unit area due to the constraining action of the nozzle, which allows the arc temperature to reach 11,000ºC in PAW.

Initiating the plasma arc requires the prior initiation of a pilot arc, which allows the orifice gas to be ionized and is obtained by supplying the electrode with a small current [14]. The ionization of the plasma gas generates the plasma arc transferred to the workpiece, which provides a low resistance path between the nozzle and the base metal plate. The transferred arc flowing through the nozzle and reaching the workpiece has a very high temperature and velocity due to the constriction provided by the orifice gas on the nozzle around the electrode.

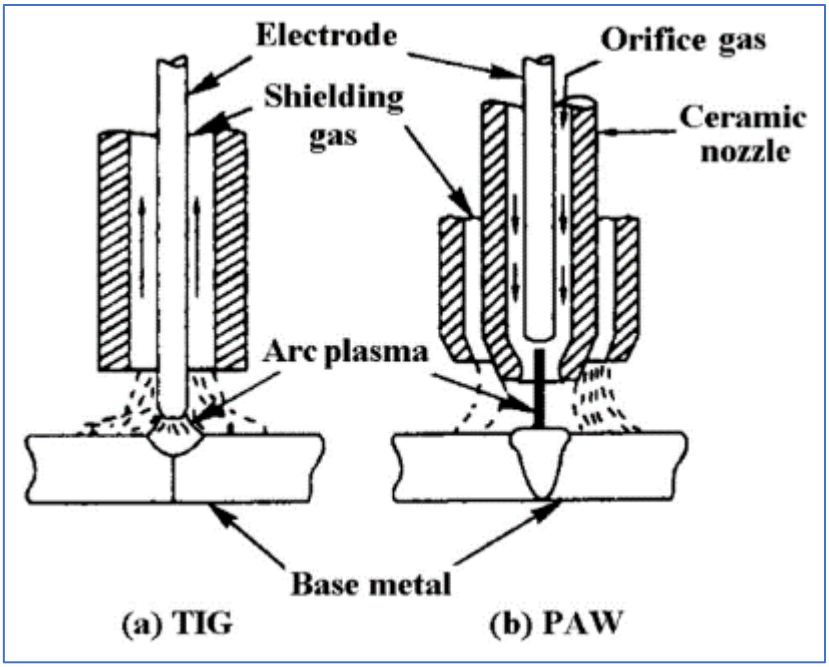

Figure 2-1: Arc plasma difference between Tungsten Inert Gas (TIG) Welding (i.e., GTAW) and PAW [14]

Much higher velocities (300 to 2000 m/s) and heat inputs (10^9 to 10^{10} W/m^2) are achieved in PAW compared to GTAW, which offers many advantages in terms of penetration depth, welding conditions, etc. [14]. Hence, PAW offers greater welding speeds, greater energy concentration, deeper penetration, and higher efficiency. Furthermore, the enclosure of the electrode inside the nozzle increases its service life since it prevents contamination with the atmosphere. The high depth achieved by the PAW process compared to the small width of the weld produced allows the reduction of residual stresses as well as the production of a narrower heat affected zone (HAZ). Although PAW offers many advantages over GTAW, the major problems associated with the PAW process is the complexity and higher cost of the equipment as well as the need to cool the torch using a flow of water, which limits the possibility of minimizing the size of the torch [14]. These problems prevent PAW from fully replacing the GTAW process.

2.1.2 Classification of PAW

The PAW process generally falls under three categories in terms of modes of operation: melt-in, micro-plasma and keyhole modes. These modes of operation are achieved through the careful manipulation of the process parameters such as current, voltage, gas flowrate, and travel speed. This is typically done through the use of sensors and control systems that monitor the welding process and adjust the parameters as needed to maintain the optimal conditions for desired mode of operation.

Melt-in Mode

The melt-in mode is a mode of operation in PAW in which the plasma arc is used to melt the metal parts being welded, joining them together through the solidification of the molten metal in a weld. This type of mode is usually achieved for currents no more than 200 A [14]. Achieving high-quality welds in melt-in mode requires the consistent setting of process parameters such as arc length, travel speed, and WFS. Additionally, the use of shielding gases, such as argon, prevent oxidation and other forms of contamination during the welding process, which can negatively impact the quality of the weld. During the melt-in mode, the electrode is less constricted compared to the keyhole mode and current ranges are lower, resulting in slightly wider beads with a melt pool that is comparable to that in GTAW [14].

Micro-Plasma Mode

The use of high current in PAW results in high thermal distortion and change in the microstructures. Thus, some applications requiring precision in welding employ the use of micro-versions of this process. When the current passing through the electrode generating the arc is lower than 30 A, the mode is referred to as micro-plasma [14]. As a result, the small and high energy dense plasma arc used in MPAW produces a narrow and precise weld bead with a consistent and uniform shape. Through proper process parameter optimization, the plasma arc allows for precise control over the weld location and penetration,

generating a bead with minimal deviations from the desired shape, thereby achieving high welding accuracy well-suited for high-precision welding applications. Furthermore, the high energy density of the arc reduces the HAZ, resulting in less thermal damage and produces a stronger, more durable weld, as well as increases fusion between the melting wire and the substrate.

Keyhole Mode

The welding of higher metal thicknesses (~2.5-6.4 mm) can also be possible by a mode of operation in PAW called keyhole, characterized by full penetration through the thickness of the sheet and high welding speeds [15]. Keyholing can obtained by using a stiff and more constricted arc through an increased setback of the electrode, as well as increasing the current to more than 200 A [14]. The "keyhole" obtained at the leading edge of the melt pool as a result of the very high energy dense plasma arc can be seen in *Figure 2-2*.

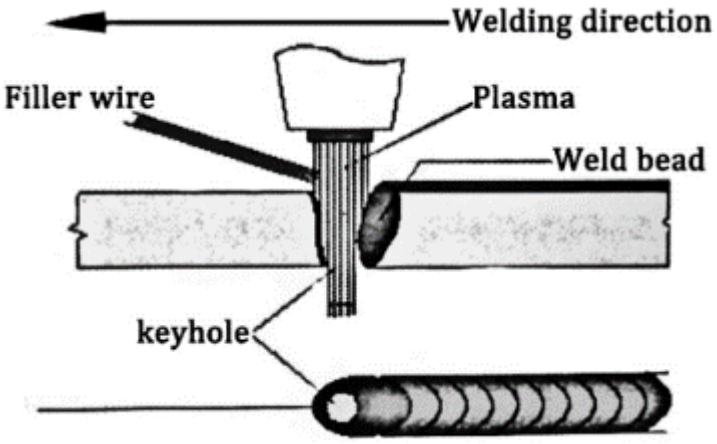

Figure 2-2: Schematic of the keyholing process in PAW [14]

2.1.3 PAW Process Parameters

The quality of the final bead geometry highly depends on the selection and optimization of process parameters and are crucial for the quality of the weld, stable arc, and overall good mechanical

and microstructural properties. The manipulation of these parameters ultimately determines the mode of operation, which plays a key role in the final weld obtained, depending on the application.

i. Wire Feed and Travel Speeds

The WFS is the rate at which filler metal is fed into the welding arc. The filler wire is used to add material to the weld joint thereby filling the gap between the two components being welded and the amount of material deposited is determined by the WFS. The WFS is usually measured in millimeters per minute or inches per minute and is controlled by a motorized wire feeder. An increase in WFS leads to a larger weld width and height but may increase the risk of a lack of fusion between the melted wire and the base metal if the WFS is too high.

The torch speed (TS) is the rate at which the welding torch travels during welding along the joint. Similar to the WFS, the TS is measured in inches per minute or millimeters per minute. Variations within the TS lead to significant changes within the heat input thus greatly affecting the amount of melting and thereby having an impact on the penetration and fusion of the weld with the base plate. If the torch moves slowly, the heat being transferred to the weld bead at a certain location is high and therefore has high penetration. The high heat input also leads to an increase in width due to the high penetration but also due to the greater amount of material that is now being deposited as a result of the slow motion of the torch. Conversely, if the TS is high, the heat input would be low leading to less penetration and a potential lack of fusion of the weld with the base plate. The low melting associated with a high TS generates an increase in the bead height and a decrease in bead width. The change in bead height may not be easily predicted whether the TS is high or low. If the TS is low, the penetration is significant which decreases the bead height. However, the low TS also means that more material is being deposited, as previously mentioned, which leads to an increase in the bead height.

ii. Arc Voltage and Arc Current

The PAW process is a constant current process, meaning the arc current remains constant during welding while the arc voltage varies. Arc voltage is directly proportional to the arc length and arc cone width [16]. As can be seen in *Figure 2-3*, as voltage increases, arc length increases and thereby increasing the arc cone width. Several studies have shown the arc length changes as a result of a change in current. The voltage also plays a role in the heat input transferred to the melt pool based on equation 1.

$$HI = \frac{VI}{TS} \qquad \text{(Eq. 1)}$$

where HI is the heat input, V is the voltage, I is the current, and TS is the torch speed.

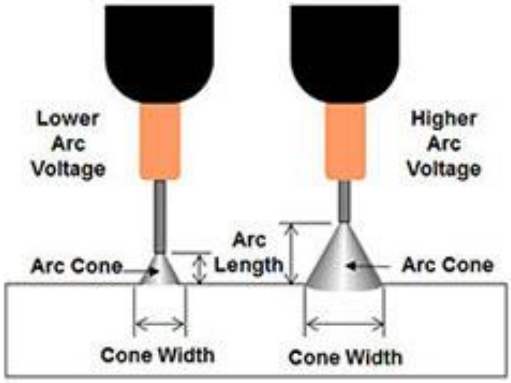

Figure 2-3: Variation of arc length and arc width with arc voltage [16]

The arc current is the welding variable that has the most effect on the weld penetration, as can be seen when comparing the modes of operation of PAW, which differ by the current ranges that are used for each. As the current increases, the weld penetration is greater, and the heat input transferred to the melt pool increases. *Figure 2-4* shows different welds produced for three different current values and the most significant depth of fusion can be seen for a current of 1000 A. Furthermore, an increase

in welding current leads to wider weld beads on both the surface and root sides [14]. However, if the current is too low, then lack of penetration as well as undercutting at the weld toe results while a very high current leads to very flat surface beads [14].

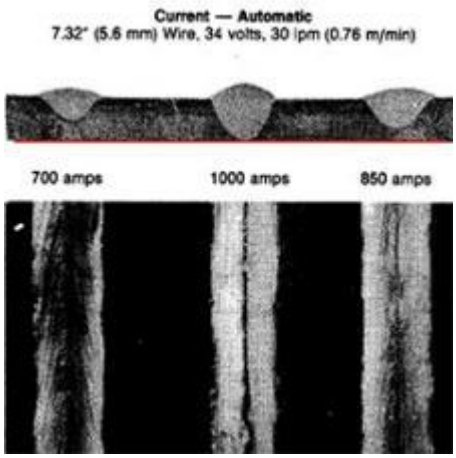

Figure 2-4: Change in weld penetration with increasing current values [16]

iii. Plasma and Shielding Gas

In PAW, the compositions and flowrates of plasma and shielding gases play a crucial role in the bead width, melted zone shape, and welding speed. The plasma gas must be composed of an inert gas to avoid rapid deterioration of the tungsten electrode and reaction of the molten metal with the atmosphere [17]. Pure argon is typically preferred as a result of its low ionization potential which ensures a dependable pilot arc and a reliable start of the arc [17]. However, the plasma gas may also be composed of a mixture of argon and hydrogen. The addition of hydrogen to the argon gas (typically 3-7%) reduces the surface tension of the molten pool as a result of ionized hydrogen molecules contacting the weld pool and increasing its temperature [18]. This leads to higher power density as well as wider beads and higher travel speeds as a result of arc voltage being higher in argon-hydrogen mixtures than in pure argon [18]. In addition, hydrogen also prevents porosity through the reduction of oxides formed when welding stainless steels and nickel alloys as a result of its fluxing effect [18]. When selecting the flowrate

of the plasma gas, it is important to remain within an acceptable range, avoiding too low values, which lead to electrode and incomplete penetration, and excessively high values, which lead to porosity and undercutting [18].

The shielding gas, as its name suggests, protects the molten metal from the atmosphere but also may affect the arc and weld properties depending on its composition, albeit not to the same extent as the plasma gas. While argon-hydrogen may also be used as shielding gas, it is important to monitor the content of hydrogen embrittlement within the weld metal especially when using argon-hydrogen as both shielding and plasma gas. *Table 2-1* shows that while adding hydrogen to both plasma and shielding gases results in hydrogen content in the produced weld, the effect is much pronounced when using argon-hydrogen as plasma gas. Hence, the use of hydrogen-argon mixture is limited to some applications and many resort to the typical use of pure argon for both plasma and shielding gas.

Table 2-1: The hydrogen content of the weld metal produced with different combinations of welding and shielding gases [18]

	Plasma Gas / Shielding Gas			
Plasma and Shielding Gases Compositions	Ar/Ar-H5	Ar-H5/Ar	Ar-H5/Ar-H5	Ar-H10/Ar
Hydrogen Content in weld metal [ml/100g]	<1	2.2	2.4	3.3

iv. Polarity

Polarity refers to the direction of the electrical current flow between the electrode and the workpiece. For any welding process, there are two types of polarities: direct current electrode negative (DCEN) and direct current electrode positive (DCEP). In DCEN, the electrode is connected to the negative terminal of the power supply while in DCEP, the electrode is connected to the positive terminal. Since electrons travel from the electrode tip to the base metal in DCEN, 2/3 of the arc heat is generated

at the base metal while the remaining heat is present at the electrode tip [19]. The concentration of heat at the base metal provides better fusion between the filler metal and base plate, making DCEN particularly suitable for arc welding processes employing non-consumable electrodes such as PAW and GTAW. This is particularly useful for melting thin materials especially when high penetration is not necessary. DCEP is typically used for GMAW, in which high WFSs and high penetration are required. However, DCEP can be used for PAW in only limited cases due to excessive heating of the electrode, and more commonly variable polarity may be applied to balance the heat between the electrode and workpiece. In the case of aluminum welding, the removal of surface oxides is an important step to achieve high quality welds and avoid weld defects such as inclusions and porosities. The much higher melting of aluminum oxides (2050 ºC) compared to aluminum alloys makes them particularly difficult to get rid of [20]. The wide use of variable polarity DCEP for cathodic cleaning of these oxides is mainly reported. Few have reported the use of DCEN for the cleaning of oxides, but it is known to be much less effective than DCEP.

2.2 Wire Arc Additive Manufacturing

WAAM is a DED process which uses an electric arc as a heat source to melt metallic wire feedstock for the purpose of fabricating or repairing components. Depending on the heat source, three main processes of arc based WAAM exist: Gas Metal Arc Welding (GMAW), GTAW, and PAW. *Figure 2-5* shows an overview of a typical WAAM system. The computer interface allows the selection of process parameters and the programming of the experimental processes, while the controller is used for the control of the robot and the welding machine. The latter provides power to the welding torch connected to the robot, establishing the deposition of wire melted by the arc. The deposition process is monitored via a sensor, usually a camera which displays the image on the computer.

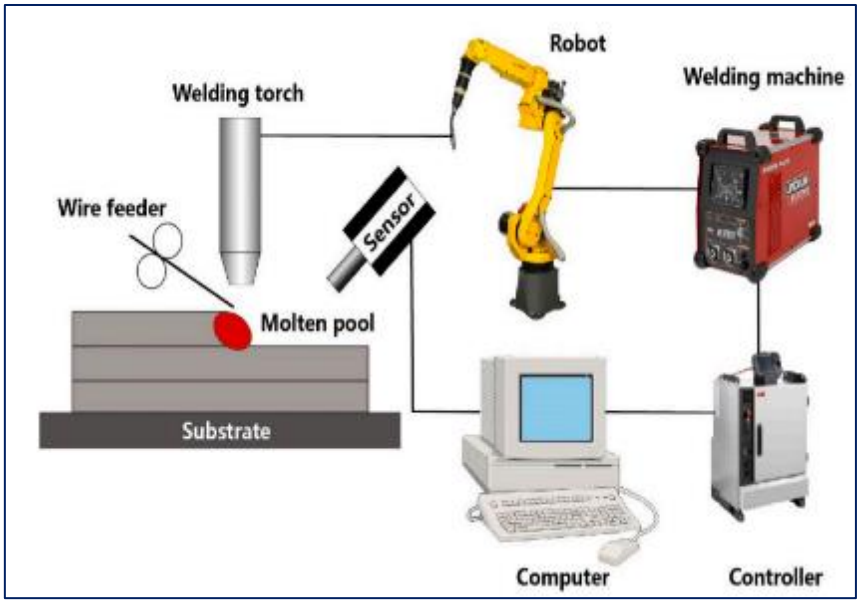

Figure 2-5: Overview of the WAAM system [21]

Compared to other AM processes, WAAM has many advantages, some of which are highlighted in *Table 2-2* based on a comparison with laser powder bed fusion (LPBF). WAAM has much higher deposition rates than LPBF, very high material utilization, and is suitable for the manufacturing of large and complex components due to its ability to be implemented using large-scale robotic manipulators [22]. Hence, WAAM has a broad commercial application especially in the aerospace sector where titanium is widely used and where material utilization is highly important. WAAM also has low equipment cost since it is based on already existing welding technologies and utilizes wire feedstock which is much lower cost compared to powders. It also has a broad range of materials that are suitable to be used by the process.

Table 2-2: Comparison between laser-based powder additive manufacturing and WAAM [11]

	Laser Based Powder Additive Manufacturing	***WAAM***
Deposition Rate	*0.1-0.2 kg/h*	*4 kg/h*
Utilization Rate	*10-60 %*	*90 %*
Manufacturing Cost	*High*	*Low*
Manufacturing Accuracy	*0.05 mm*	*0.2 mm*

However, the main issue in WAAM is the low manufacturing accuracy due to the instability of the process with high heat accumulated layer-by-layer being one of the important factors. This is because of the nature of WAAM incorporating an arc welding process as its main source of energy. Other factors include a more complex programming strategy, unstable weld pool dynamics due to bad parameters setup, and environmental influence such as gas contamination. Residual stress is therefore prominent in fabricated components and may lead to problems such as parts deformation, geometric tolerance loss, delamination of layers during the deposition process, and deterioration of fatigue performance and fracture resistance [21]. *Figure 2-6* highlights the common defects encountered in parts fabricated by WAAM for different materials. In the case of steel, residual stress, deformation, and surface finish are the most common problems encountered and hence require post-process treatments for these to be alleviated, through annealing for example in the case of residual stress.

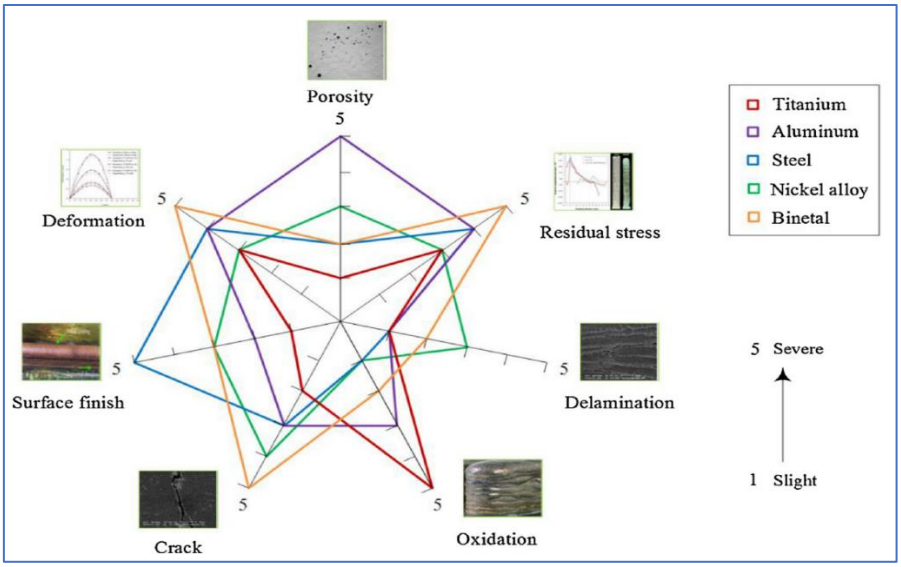

Figure 2-6: Common material defects in WAAM [6]

However, post-process heat treatments are time-consuming and hence several researchers have looked into optimizing the process parameters for low heat input while other methods such as geometrical fixing of layers through feedback control implementation were developed. Despite the disadvantage of WAAM in terms of accuracy, it is important to assess the logic behind the investment in such a technology. *Figure 2-7* shows a comparison of different AM processes in terms of building rate and accuracy. It reveals that DED falls between LPBF and additive friction-stir manufacturing (AFSM) in terms of accuracy and building rate [23]. The building rate of LPBF falls between 0.05-0.2 kg/hr while that of AFSM falls between 0.5-10 kg/hr. Despite AFSM reaching high building rates and avoiding defects such as porosity, cracks, and solidification shrinkage found in DED processes, it lacks the geometrical complexities and capabilities of the latter, proving to be its biggest limitation as shown in *Figure 2-8* [23]. Hence, the use of DED processes such as WAAM for the purpose of 3D printing complex parts would be a wise choice while also maintaining a low heat input to avoid defects associated with fusion processes. The use of MPAW for WAAM would fit into that need and optimizing further the parameters for proper part requirements and heat input is also possible. *Table 2-3* gives a brief

overview of some of the parameters that influence the bead quality. Some of the parameters were already discussed in section 2.1.3 for PAW.

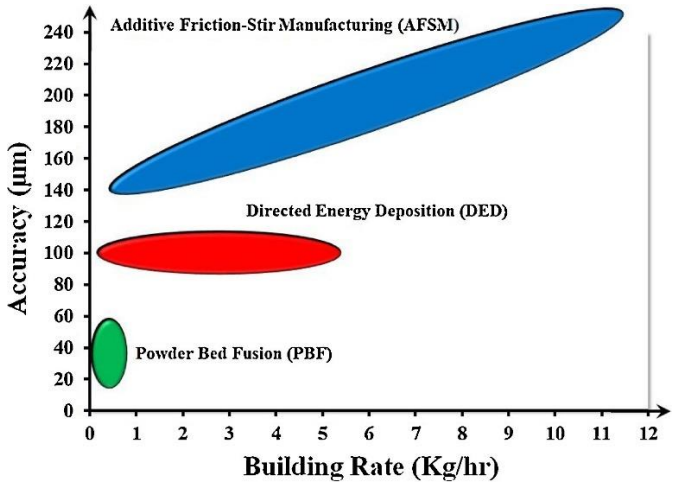

Figure 2-7: Comparison of accuracy and building rate for different fusion and friction-based AM technologies [23]

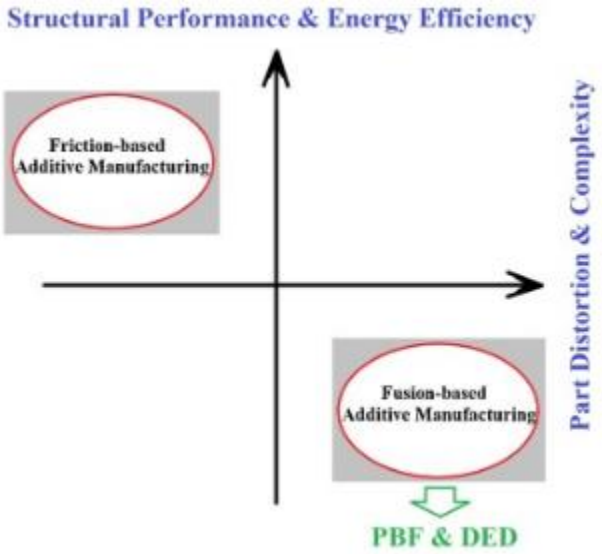

Figure 2-8: Comparison between capabilities of friction-based AM technologies with fusion-based ones [23]

Table 2-3: Parameters affecting bead quality

Parameters	Effect on Additive Part
Heat Input	Controlled by current, voltage, and travel speed. Low heat input results in a more uniform surface. Lower mechanical properties with high heat input.
Current	Large current leads to instability and overflow. Layer height decreases and width increases with increase in current.
Voltage	Increase in voltage causes decrease in layer height and increase in layer width.
Wire feed and travel speeds	Direct effect on layer width and height: Increase in wire feed speed causes more material deposition. Higher torch speed leads to less melting and hence, decrease in width and increase in height.
Substrate temperature	Preheating substrate makes deposition process smoother since high thermal difference is avoided.

2.3 Austenitic Steel Microstructures and Effect of Anisotropy in WAAM

Since WAAM is particularly useful for higher value components, a great deal of work focuses on stainless steel fabrication. Austenitic steels are versatile alloys that find applications in many industries such as marine, construction, and nuclear due to their high corrosion resistance, excellent low- and high-temperature properties, high toughness, formability, and weldability [24]. One of the most studied grades of austenitic steels in WAAM are AISI 316L and AISI 316LSi. The structure of 316L fabricated using WAAM consists of coarse columnar grains oriented along the direction of heat extraction, aligned with the build direction [25]. Studies have shown that the presence of δ in austenitic stainless steel is useful to prevent hot cracking, reduce the segregation of the material during processing, as well as eliminate the formation of low melting point eutectic phases, as demonstrated in prior studies [25] [26]. Chen et al. [26] analyzed the microstructures of an austenitic stainless-steel wall produced by GMAW-based WAAM which consisted of δ (vermicular and lath morphologies), γ, and σ intermetallic phases and showed that the formation of σ phases followed in subsequent layers at the γ/δ interfaces and was a

result of subsequent thermal cycles reaching the precipitation temperature of the σ-intermetallic. Wang et al. [27] carried out WAAM fabrication of AISI 316L stainless steel structures under two different arc modes while keeping the deposition rate constant to analyze the correlation between arc mode, microstructure, and mechanical properties, and optimizing arc mode offers some ability to tailor microstructure and optimize properties in WAAM when using GMAW.

One of the essential features in stainless microstructures is the secondary dendrite arm spacing (SDAS), which is greatly sensitive to heat input. It is often found that the SDAS at the top layer is larger than that of the bottom layer during WAAM, and this is due to the cooling rate [27]. The substrate acts as a heat sink, and hence the cooling rate is higher compared to the top layer. This results in finer solidification structure and smaller SDAS [27]. Typical stainless-steel microstructures of WAAM components can be seen in *Figure 2-9* characterized by skeletal and lathy ferrite, revealing that the SDAS at the top layer is larger than that at the bottom layer. Other studies have also looked at the effect of heat input on WAAM of austenitic AISI 316L. Cunningham et al. [28] analyzed the effects of the interpass temperature and heat input process parameters on the WAAM of AISI 316LSi. The microstructures generally consisted of fine columnar dendrites with lath and vermicular morphologies, while the low interpass temperature and heat input wall specimen displayed the greatest volume of δ-ferrite due to the high cooling rate. Furthermore, Rodrigues et al. [29] investigated the evolution of the microstructure of 316L walls fabricated by WAAM upon the application of different heat treatments and found that with an increase in heat treatment time, ferrite acted as nucleation site for σ-phase to slowly precipitate, with the latter slowly replacing the former. This is shown in *Figure 2-10*.

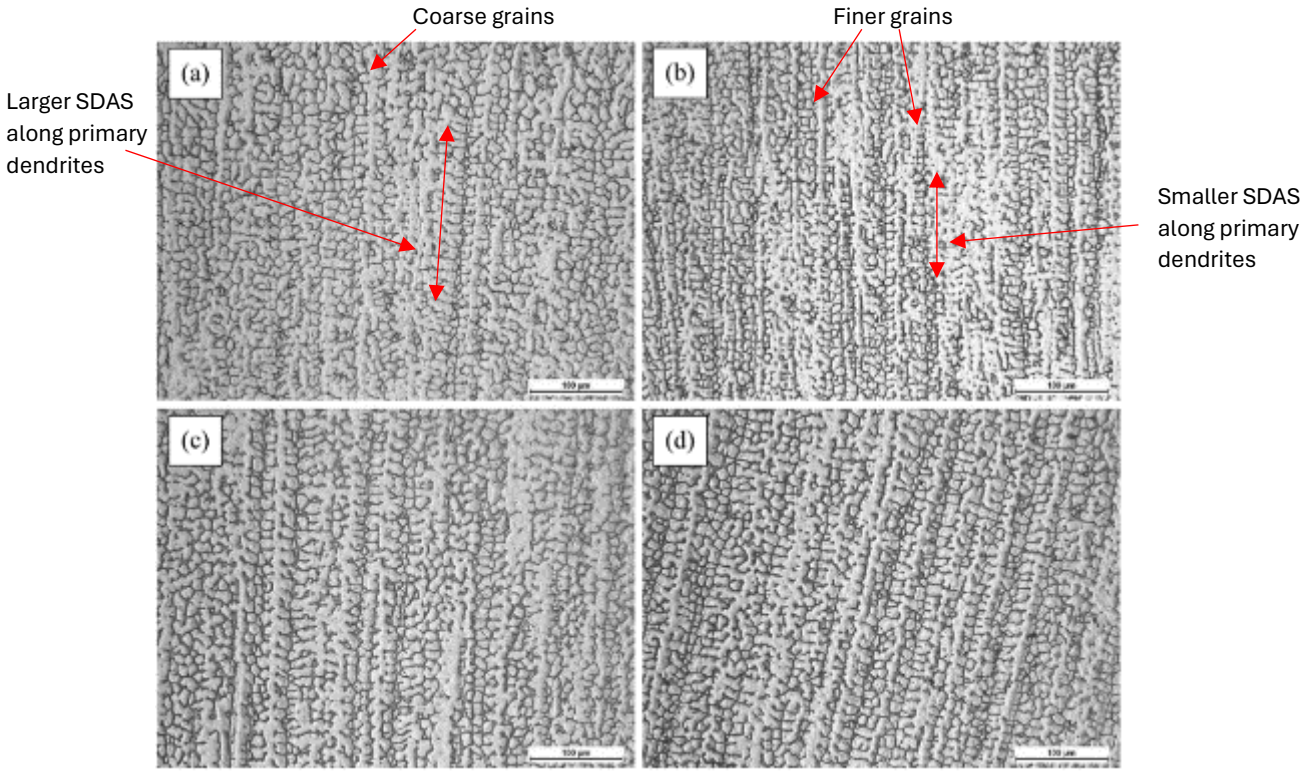

Figure 2-9: Optical micrographs of cross-sections of WAAM 316L components for a) bottom layer at location 1 b) bottom layer at location 2, c) top layer at location 1, and d) top layer at location 2 [27]

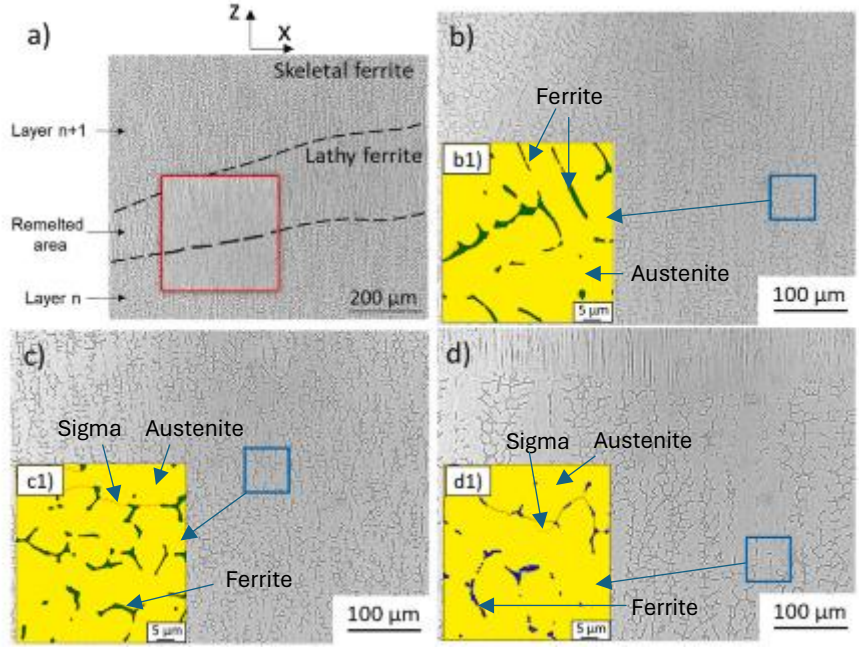

Figure 2-10: Microstructures of a) sample b) as-built c) 400 C heat treated for 1 hour and d) 950 C for 2 hours [30]

Anisotropy is an important phenomenon which can arise in WAAM, since directional solidification can strongly influence the crystal orientation of solidifying metal. Wang et al. [31] studied the microstructure and tensile properties of 316L stainless steel by manufacturing a thick-walled component using cold metal transfer. In the travel direction, the microstructure revealed periodically alternating regions, entitled remelting area and overlapping area. The remelting area presented large columnar grains perpendicular to the fusion boundary while the overlapping area revealed epitaxial growth of grains in the building direction. While this study analyzed the microstructural characteristics of 316L stainless steel of thick-walled components, Belotti et al. [25] analyzed the structure of the same type of component at different scales for the purpose of understanding the effect of spatial variations on the microstructure, which are identified in terms of fusion zone shape, granular structure, texture, and phases present. It was found that the structure of the component exhibited coarse and highly oriented grains as well as a dominant <100> texture in the building direction across the overlapping area between the fusion zones. This is a rather common observation in various AM techniques when producing metals with a cubic crystal structure, since the <100> direction represents the easy-growth direction of the crystal solidification, and this will promote grain growth along the direction oriented with the heat flow. Anisotropy was also reported for titanium alloys using AM such as in the study conducted by Wang et al. [32], which analyzes the anisotropic mechanical properties of a Ti-6Al-4V plate fabricated by electron beam melting. A decrease in yield and tensile strengths was reported along with an increase in the build height of the specimen, which is associated with the increasing α lath as a result of the different thermal histories [32]. Carroll et al. [33] also analyzed the anisotropy in a Ti-6Al-4V component fabricated by laser-based DED-AM. It was reported anisotropic elongation properties as a result of long and thin β grains growing along the build direction, making the ductility significantly higher along the build direction compared to the travel direction. A decrease in the yield and tensile strengths can be

observed along the build direction as a result of the increase of α laths [34]. The disruption of the solidification process may also be achieved by the application of ultrasonic vibration methods with frequencies ranging from 15 to 75 kHz, providing acoustic cavitation. The use of ultrasonic vibration allows greater control of the solidification process than VWC and provides a large and significantly high degree of grain refinement when ultrasonic amplitude is increased [35]. However, ultrasonic methods require the use of an ultrasonic generator and an ultrasonic transducer, both significantly more expensive than the equipment used by VWC.

2.4 Arc Gap Monitoring

2.4.1 Arc Seam Tracking

Arc seam tracking is a technique used in welding that heavily relies on different sensors to monitor the position of the arc in real-time relative to the arc seam. The purpose is to improve the quality of the weld through the future adaptation of control systems based on reliable seam tracking. Seam tracking techniques mainly fall under three major known categories: Through Seam Tracking (TST), Laser Vision Seam Tracking (LVST), and Vision-based Seam Tracking (VST).

TST is a type of 2-axis real-time monitoring system that requires the robot manipulator to weave the weld torch assembly across the weld joint, as shown in *Figure 2-11*, and to subsequently monitor the unregulated variable as function of torch position [36]. In the case of PAW, the unregulated variable is the arc voltage, which varies with arc length. In GMAW, when the torch is at the edge of the weave, welding current peaks leading to the TST to perform necessary corrections to the torch position. Feedback variables for TST in robotic GMAW have been investigated through monitoring with respect to the torch position, revealing that the average current is an effective feedback variable for seam tracking [36]. This would mean that the change in current is an effective monitoring value used to adjust the path of the torch ensuring proper weld position.

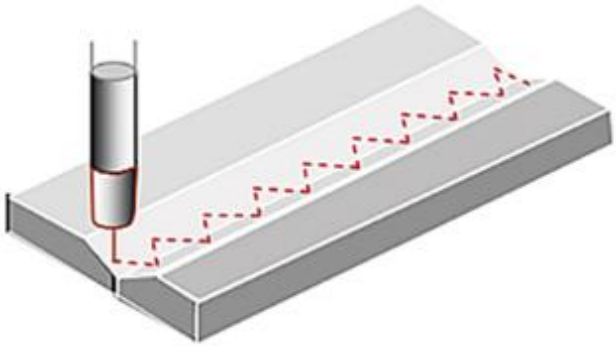

Figure 2-11: Display of the torch weave across the weld in through arc seam tracking [37]

LVST involves the on-line projection of a laser beam hitting the seam and reflecting back to the sensor typically a camera, which provides the accurate location of the seam based on the distortion in the laser line. The principle of the laser line scanner is shown in *Figure 2-12*. This technique is mainly useful for material thicknesses of less than 1 mm, is immune to interference from ambient light, and the camera is free from weld spatter [38]. This method is particularly useful for adaptive control by using the data provided by the seam tracking for adjustments to voltage, WFS, and torch speed. As a result, it has been employed in AM for layer height correction purposes [39] [40].

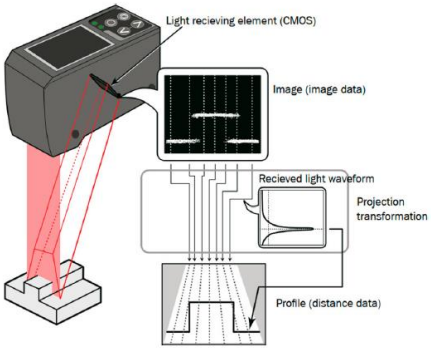

Figure 2-12: Principle of laser line scanner [39]

VST employs the use of vision sensors and relies on image processing software to identify the seam. Applications of vision sensing for real-time seam tracking in GTAW have been developed [41] and monitoring techniques based on vision sensors have also been applied in WAAM and further

advanced. For example, deposition height in WAAM was controlled through the visual inspection of previous and current layers [42]. The information was gathered by a passive vision sensor and greatly increased corrective accuracy compared to simply monitoring the current layer.

2.4.2 Arc Voltage Drop

When measuring the arc voltage, it is important to know at which location the sensor is taking the measurement from due to the different voltage drops that are present within the arc. These voltage drops occur at the contact tip, the electrode extension, the anode fall, the arc column, and the cathode fall. These voltage drops are broken down in *Figure 2-13*. The most significant voltage drops occur mainly along the anode, the cathode, and the arc column and the accurate determination of the anode and cathode fall voltages has been researched for both non-consumable [43] and consumable electrode welding processes [44]. Typically, in constant current processes such as GTAW and PAW, the voltage drops associated with the anode, cathode, and arc column are independent of the current. Therefore, irrespective of the current chosen, it can be expected that the voltage drops will remain the same after they already have been determined. The electrical power being dissipated as heat as a result of the voltage drops can be calculated by the equation $q = IV$ where I is the current and V is the total voltage drop.

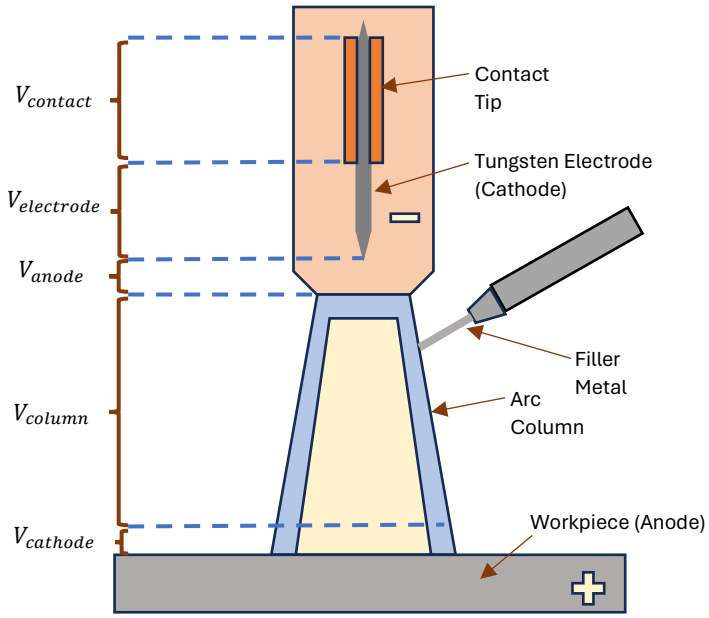

Figure 2-13: Voltage losses across the arc for PAW

2.4.3 Automatic Voltage Control

AVC systems are typically used for constant current arc welding processes such as GTAW and PAW to control and maintain the arc length through adjustment of the arc voltage. Since arc length and arc voltage are directly proportional to each other, any adjustment to the latter will lead to an adjustment in the former. *Figure 2-14* shows a block diagram of a traditional AVC system for GTAW. As the voltage command (V_{ref}) is set, the difference between the actual voltage (voltage telemetry) V_{arc} and V_{ref} will be accounted for by the AVC through K_{arc}, which adjusts arc length L_{arc} though adjustment of V_{arc}.

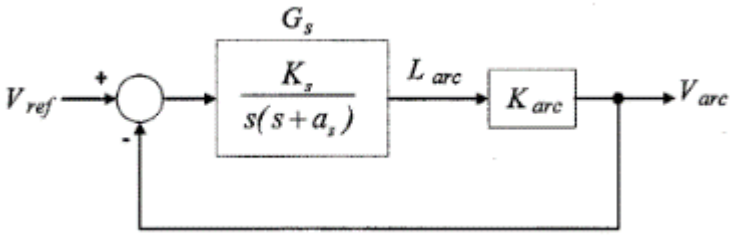

Figure 2-14: Traditional closed loop AVC for GTAW [45]

Although traditional AVCs perform adequately in most circumstances, there are instances in which position control is not adequate. This is a result of the arc voltage-to-arc length gain K_{arc} that varies with nominal of the arc current rather than remaining constant, which means that even if the AVC has a fixed voltage command, the arc length will vary with changes in arc current [46]. This makes traditional AVCs highly unreliable. Hence, different adjustments have been attempted to resolve this issue such as the development of an adaptive voltage controller [45] or the introduction of a filtered current-dependent voltage compensation, which allows the use of an adoption factor that accounts for the fluctuations in arc voltage [47]. The use of AVCs remain commonly used in GTAW and PAW processes as an easy alternative mode of control.

2.5 Control Strategies for Height Control in WAAM

During the deposition process, when the number of deposited layers increases, it is difficult to control the morphology and size of the deposited layer which will affect the geometrical accuracy of the part [48]. Heat accumulation is a concern in WAAM since thermal distortion and residual stresses affect the geometry and properties of the final component. As the part is formed, the heat accumulates thereby reducing the geometrical accuracy of the printed component. Control strategies must thus be implemented without resorting to open loop control which do not help in the elimination of layer geometry variations that result from changes in process parameters. Thus, the need for in-process feedback control in WAAM is crucial in obtaining a smooth and reliable production process. The

implementation of a real-time monitoring system is important for an efficient and break-through stability control of WAAM.

Several research works have been done on the development of a feedback system for increased process stability of several DED processes. Heralić et al. developed a controller based on optical measurements for control of the bead height and bead width in laser metal wire deposition [49]. The monitoring of the previous layer height and width is done through the projection of a laser line in front of the melt pool and through image processing algorithms. While closed loop control is usually most effective for improving the stability of a process, a feed-forward compensator that controls the wire feed speed was used to control the height.

Several papers have proposed different approaches for controlling the height of the layer in WAAM, each employing different control inputs. The idea is to attempt to keep the nozzle to surface distance (NTSD) constant throughout each layer deposition. Control strategies developed for WAAM were a bit more recent with the work presented by Xiong and Zhang, in which they designed an adaptive control system of the deposited height using a passive vision sensor [50].

Furthermore, more recent studies have focused on controlling the height based on new control inputs such as the current due to its major effect on the heat input. Ščetinec et al. implemented an in-process path replanning and online layer height control based on the arc current for a GMAW-WAAM process [51]. Deposition arc current was considered as control variable for layer height control. The authors were able to keep the NTSD constant through testing several controllers. Li et al. developed a self-adaptive control system for wire arc additive manufacturing using double electrode micro plasma arc welding [52]. They were able to reduce the heat input successfully through the implementation of a bypass while controlling the bead geometry height, the latter done through the adjustment of the wire feed speed. Despite these research papers, more work is required in that area for improved accuracy.

2.6 Vibratory Weld Conditioning

Due to the intense heat input associated with arc welding processes as well as the continuous heating and cooling cycles of WAAM during fabrication, the final part created will result in large temperature gradients between the layers close to the substrate and the top layers. The different thermal cycles cause thermal stress to the component, thereby resulting in residual stresses and plastic deformation that leads to distortion. These lead to fatigue damage, stress corrosion cracking, and fracture [53]. Much research has been focused on the elimination of residual stresses in arc welding by employing methods such as vibratory stress relief (VSR) [54], post-weld heat treatment [55], and ultrasonic impact treatment [56]. Specifically, considerable has been put into the application of vibration for an improvement in the process and properties of the final part. *Figure 2-15* shows the different modes of vibration that can be applied on the process, which are the workpiece, the melt pool, power source, welding arc, and electrode [57]. These can be encompassed into two categories: physical vibration of the workpiece and pulsation of current of the power supply. The physical agitation of the workpiece and vibration of the melt pool are closely related to each other since one lead to the other. The pulsing action of the current leads to the oscillation of the arc droplet and the electrode.

Recently, most of the research related to the use of vibration in arc welding has been focused on its application during the process due to the much greater increase in productivity achieved as well as the greater influence on the reduction of residual stresses and improvement in mechanical properties compared to post-weld vibration. This method is called VWC or vibratory assisted welding, which relieves stress in the welding components, where vibration would be applied to the substrate during the welding process [58]. The purpose of VWC lies in the elimination of residual stresses and improvement in the microstructure and mechanical properties through the refinement of grains [57]. Through the vibration of the workpiece during welding, the solidification process in the melt pool is affected and

hence, the grains are broken down and prevented from forming oriented large columns thus leading to nucleation sites for the formation of finer grains as well as a uniform distribution of grains.

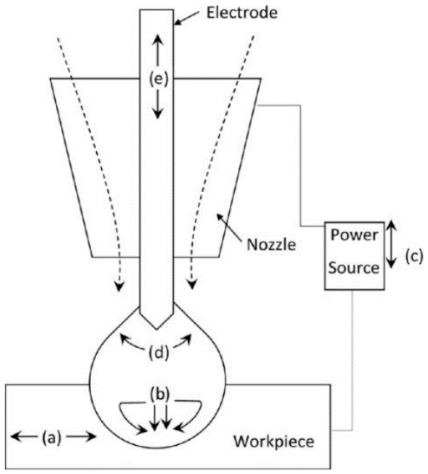

Figure 2-15: a) Vibration of workpiece b) weld pool oscillation c) vibration through pulsing of current d) welding arc oscillation e) electrode vibration [57]

The reduction in residual stresses through employing VWC has been reported in many research papers. Xu et al. investigated the effect of VWC on the residual stresses and distortion in multipass girth-butt welded pipes and found a reduction in residual hoop stress at the outer surface by 30 % [53]. Other studies have reported on the change in mechanical properties as a result of VWC. Kalpana et al. investigated the effect of VWC on the tensile strength of welded joints and found an increase in tensile strength as a result of an increase in amplitude [59]. More recent work involved looking into the effect of harmonic vibration with a frequency just below the resonant range on the mechanical properties of aluminum alloy parts fabricated by GMAW [58]. Vibration was subjected at 50 Hz below the natural frequency of 83 Hz while investigating the microstructures and mechanical properties at different vibration forces (400, 750, and 1000 N). They reported a decrease in grain size as the vibration forces increased, as shown in *Figure 2-16*. The decrease in grain size is evident in the microstructures presented in *Figure 2-17*, especially when comparing the case of no vibration, which presents large coarse grains (Fig. 6d) to that of a 1000 N vibration force, which presents fine equiaxed grains in a more uniform

distribution. The changes seen in the microstructures lead to increases in yield and tensile strengths as well as a decrease in elongation. The investigation of refinement of grains was also performed using the application of ultrasonic vibration on the melt pool with the purpose of inducing acoustic cavitation and streaming effects thereby affecting the solidification process and grain growth. However, the use of ultrasound vibrations requires an ultrasound generator as a transducer, making it a more expensive approach than VWC.

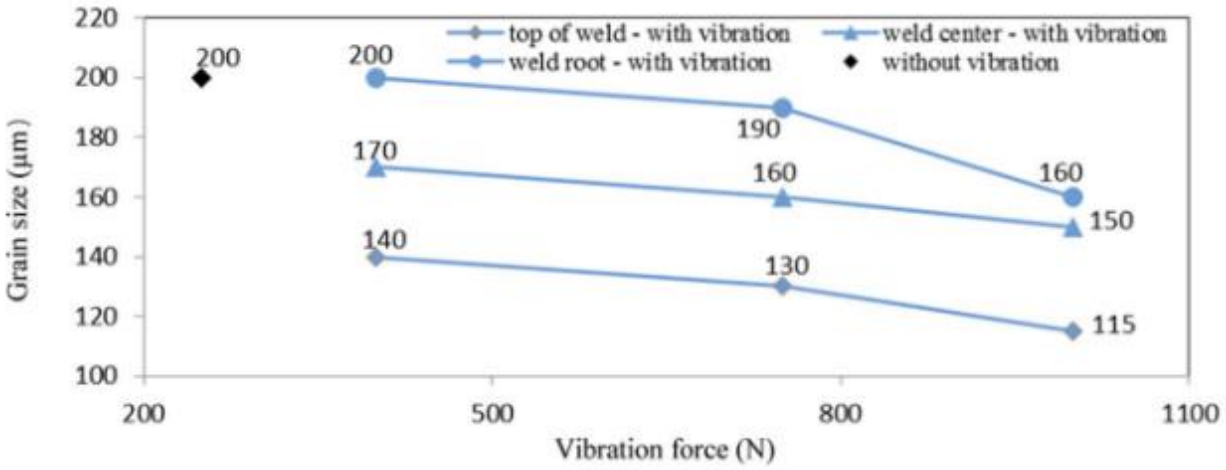

Figure 2-16: Variation of grain size with increasing vibration force [58]

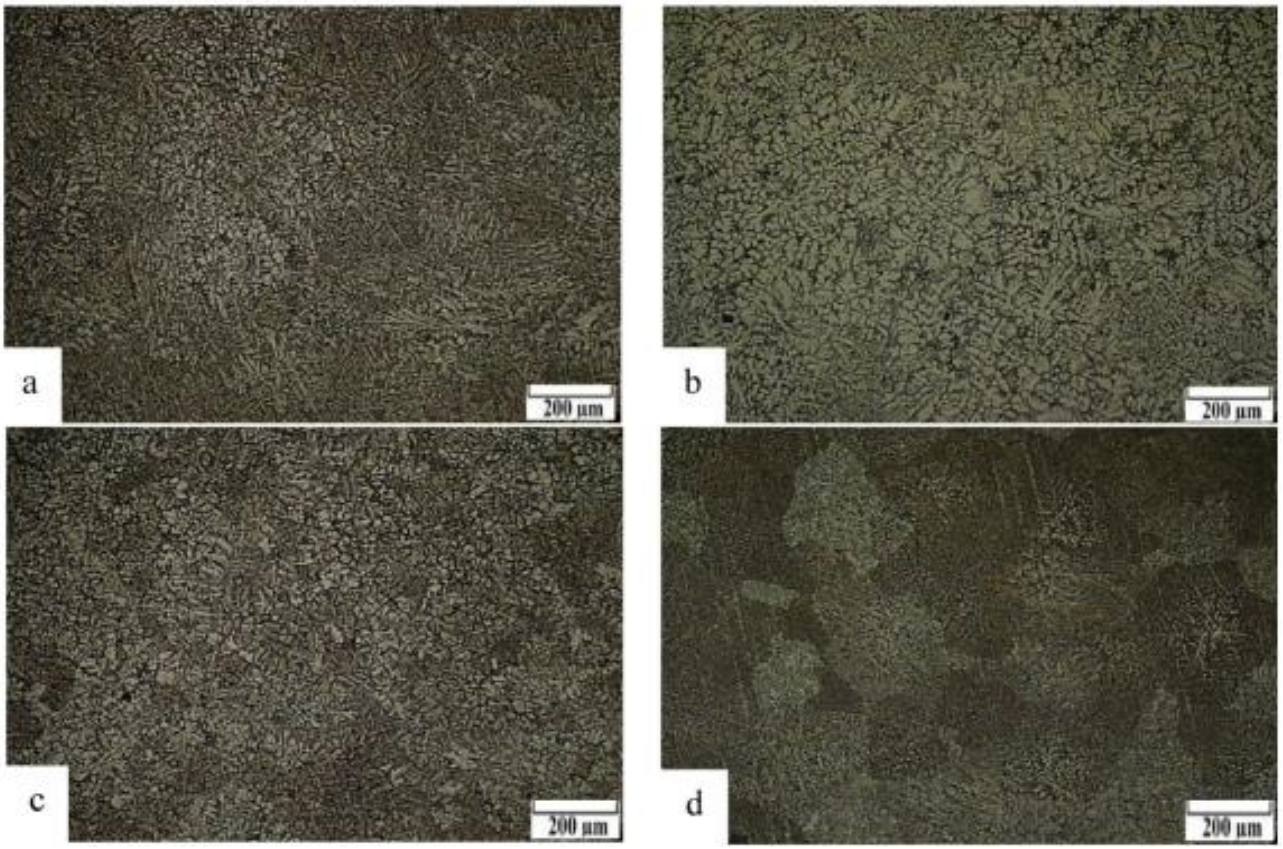

Figure 2-17: Microstructures of the region near substrate for vibration forces of a) 400, b) 750, and c) 100 N. The case of no vibration is also shown in d [58]

Chapter 3
Experimental Methods

This chapter discusses the different materials, methods, and experiments that were used for each study. The equipment and setup are also highlighted in this section as well as the different process parameters and characterization methods. Each section in this chapter includes the methods used for each different chapter in the thesis.

3.1 Anisotropy in Wire Arc Additive Wall

3.1.1 Wall Fabrication

The fabrication of thin-walled structures was performed using a Liburdi Automatic Welding System (LAWS) 1000 developed by Liburdi Automation. The system uses the MPAW process with a Liburdi LP50 Pulseweld power supply with a maximum current of 50A, a plasma torch, which creates an arc through the ionization of a shielding gas, an external wire feeder, and monitoring camera. The system is able to achieve heat inputs of 0.15-0.2 kJ/mm and the maximum torch speed possible without inducing lack of fusion and discontinuities and while maintaining this heat input is 180 mm/min. The welding setup and front camera view are shown in Figure a and b respectively. The wall was created by depositing 0.9 mm AISI 316LSi stainless steel wire fed at the leading edge, in a layer-by-layer manner linearly to produce a wall with dimensions of 150 mm × 130 mm × 4.5 mm, consisting of a total of 300 layers as shown in *Figure 3-1c*. Each layer was created by a single continuous deposition track. Uni-directional deposition was used throughout the entire build process. While this approach may result in higher fabrication times, it is ideal for improved control and stability of the process. The AVC feedback system was enabled throughout the fabrication process, which would aid in maintaining an optimal nozzle to surface distance. The nominal chemical composition of the wire material in wt% is 19Cr-12Ni-2.5Mo-0.8Si-Fe for AISI316LSi alloy, where the Si is added to improve the wetting of the molten pool, and a maximum carbon content of 0.03 wt% is allowed based on the L designation. The cooling time

between each layer deposition was kept between 4 to 6 minutes such that the layer temperature was always below 107ºC before initiating the arc again. The cooling time increased from 4 to 6 minutes as heat input increased. The layer temperature was monitored using a temperature indicating crayon, which melts if the weld has a temperature greater than 107ºC. This interpass temperature was chosen based on taking the average of the low and high interpass temperatures in the work of Cunnigham et al. [28]. The base plate used is made of AISI 1020 cold rolled steel with dimensions of 200 mm × 50 mm × 10 mm. Shielding gas consisted of 99.999 % pure argon throughout the arc welding process, with a flow rate of 19 L/min. Furthermore, different process parameters were used for the initial beads as compared to those for subsequent layers. For the first 2 to 3 beads, higher heat input was used to obtain more melting and thus wider beads through setting the voltage and current at 22 V and 25 A, respectively. The WFS was set at 250 mm/min while the TS was set at 50 mm/min, thus reinforcing the melting of the layer, and providing wider initial beads. For subsequent beads (4^{th} and above), voltage was kept within the range of 19-20 V while the current was set within 21-23 A. The WFS was kept constant throughout the entire fabrication process while the TS was now set at 80 mm/min to reduce the heat being transferred to the melt pool. The process parameters can be found in *Table 3-1*.

A range of welding parameters were tested before reaching the optimal parameters to achieve consistent bead shape and adequate weld quality based on visual inspection. Different TSs were initially tested, and it was found that a TS of 50 mm/min yielded too much melting while a value of 100 mm/min yielded little material deposition. A WFS of 250 mm/min was found to yield an optimal material deposition, avoiding any lack of fusion while also depositing a significant amount of material. The voltage is directly proportional to arc length, therefore as the voltage increases, the arc length increases. Hence, the voltage values were chosen according to the most optimal arc length. The optimal arc length was found to be 2.25 to 3 mm.

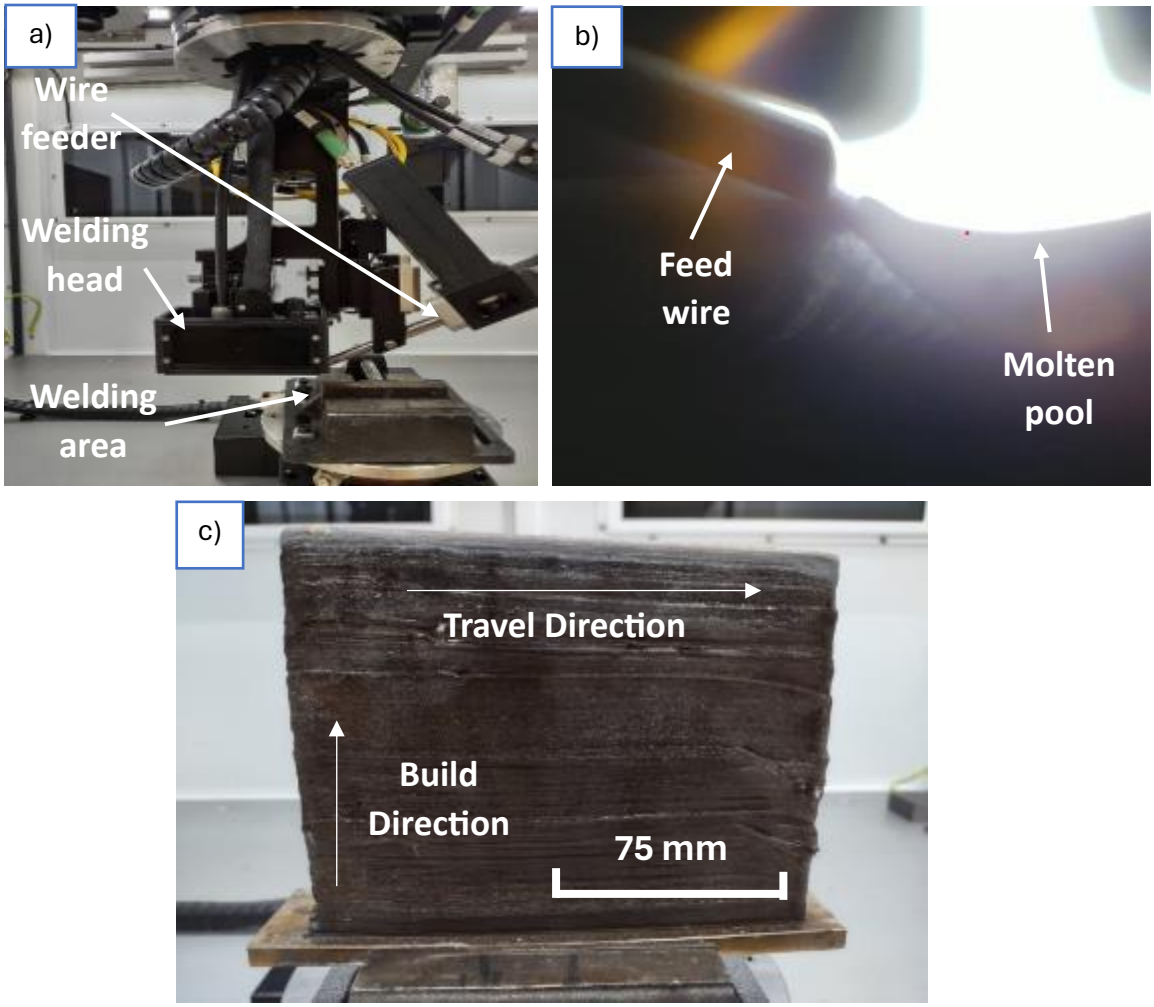

Figure 3-1: a) LAWS 1000 experimental setup b) Monitoring camera view c) Final wall component fabricated by WAAM

Table 3-1: Process parameters for wall creation

Parameters	Current (A)	Voltage (V)	Travel Speed (mm/min)	Wire Feed Speed (mm/min)	Shielding Gas	Wire
1st layer	25	22	50	250	Argon (99.999%)	316LSi (0.035'')
Next layers	21-23	19-20	80	250		

3.1.2 Microstructural Characterization

To examine the overall microstructure of the thin-walled structure, cross sections in both the build and height direction were prepared. The cross section of the specimens is shown in *Figure 3-2a*.

In *Figure 3-2b*, the Y-axis and Z-axis are parallel to the travel and build directions, respectively. Samples M1 and M2 were prepared from the XZ plane, which correspond to the build direction, while samples M3 and M4 were prepared from the YZ plane, which correspond to the travel direction, all of which are highlighted in *Figure 3-2b.*

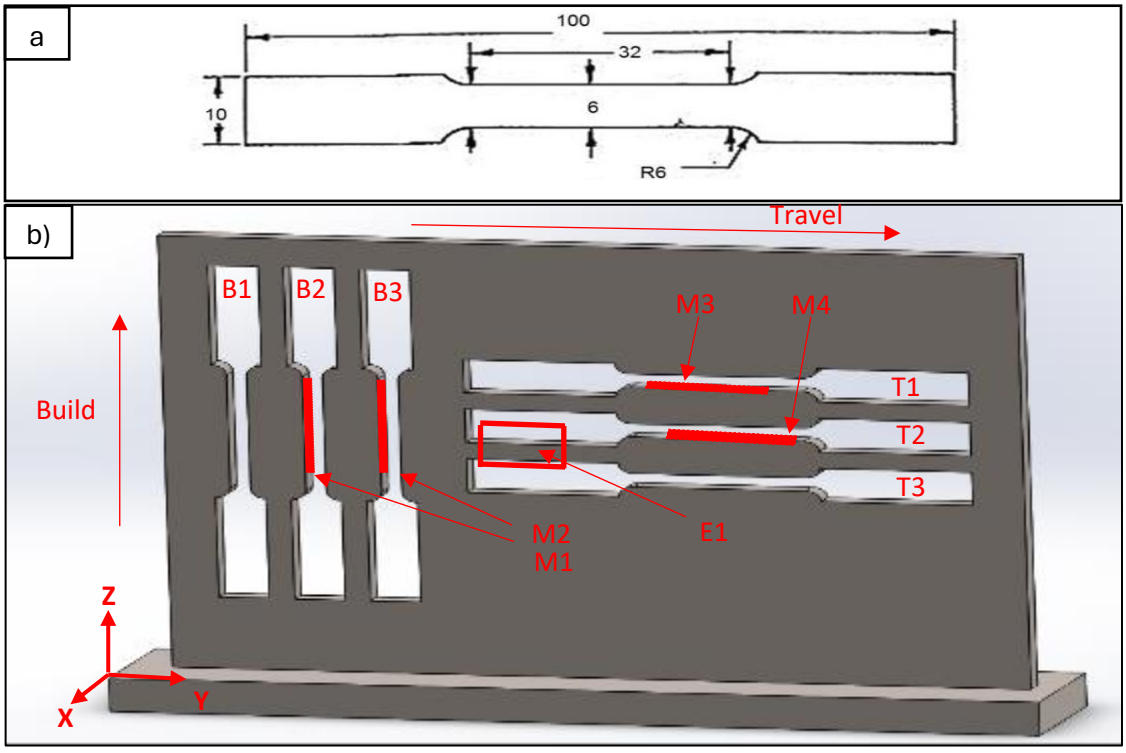

Figure 3-2: Tensile coupon dimensions according to ASTM E8 "subsize" specimen specification b) Tensile and metallographic sample locations. The dimensions are in millimeters

Samples M1 and M2 were taken from different locations along the travel direction (XZ plane) while samples M3 and M4 were taken from different locations along the build direction (XY plane). This was done to assess the changes in microstructures along each direction. Initially, tensile samples were cut. The cross section of samples was cut in close proximity of tensile specimen locations using a conventional bandsaw after the tensile samples were extracted. The specimens for metallography were prepared using conventional sandpaper grinding with 1 μm final stage diamond polishing. The samples were immersed in oxalic acid (10 g Oxalic, 100 mL H_2O) and electro-etched at room temperature using an austenitic stainless-steel cathode at 6 V for 90 seconds. The microstructural observations were made

using a Zeiss AX10 optical microscope. Vibratory polishing was performed for three hours using 0.04 µm colloidal silica suspension before subjecting the samples to electron backscatter diffraction (EBSD) analysis. EBSD was used to obtain grain orientation information of the sample microstructures on a TESCAN VEGA3 scanning electron microscope equipped with a Bruker EBSD detector with a step size of 0.5 µm. The EBSD sample used is highlighted in *Figure 3-2b* as E1.

3.1.3 Mechanical Tests

To study the mechanical properties of the thin-walled component, the three tensile coupons from the build and travel directions shown in *Figure 3-2b* were tested. Tensile coupons were cut using abrasive waterjet cutting with dimensions according to ASTM-E8 sub-sized specimen specification. Tensile tests were performed using a Tinius Olsen HK10T servo-mechanical tensile machine frame of 10kN capacity with a crosshead speed of 1 mm/min at ambient temperature. The initial strain rate was therefore around 0.0005 s^{-1} similar to rates found in literature [60]. Mechanical properties were determined by taking the average of the three tensile samples in each direction. Furthermore, a digital image correlation (DIC) technique from Correlated Solutions was used to monitor strain, and VIC3D software was used to analyze the local strain in the transverse plane of the tensile coupons during uniaxial tensile loading using step size 29 and subset 7. Strains were obtained using the extensometer feature of DIC. Prior to starting the tensile test, the transverse planes of the tensile samples were spray painted with a white background followed by spray painting fine black speckles. The Vickers microhardness was tested across the shown surfaces of the four metallographic samples M1, M2, M3, and M4 with a 500 g load and loading time of 10 s. The indentation map covers the entire samples with a 250 µm × 200 µm step size. The average hardness values across 4-5 indentation lines covering the entirety of each sample were calculated to analyze the microhardness distributions. The mean hardness of the weld metal was then given by averaging the hardness of 290-300 points located across the

samples, depending on different bead width. The 95% confidence interval was also calculated for a statistical analysis purpose.

3.2 Vibratory Weld Conditioning

The application of vibration on the workpiece was performed using a shaker device bolted into some aluminum 6061 mounting plate, which serves as support for the build area. Aluminum was chosen based on its lower stiffness compared to other materials. The setup is shown in *Figure 3-3a* and *Figure 3-3b*. The aluminum plate used has a width of 15.5 cm and a thickness of 7.9 mm. The build area lies at the end of the plate 25 cm from the center onto which the aluminum plate is bolted, with the shaker underneath it, as shown in the *Figure 3-3a*. The setup (material and dimensions) was done such that the oscillations within the melt pool vibration would be maximized. The build area consists of a plate, mounted in the aluminum plate and onto which the wire would be deposited. Two different materials were investigated at different vibration parameters: titanium (Ti 5553) and stainless steel (316LSi). The travel direction of deposition is shown in *Figure 3-3b*. Titanium was studied on top of stainless steel due to it being a single phase BCC material and as a result, has a less complex microstructure than stainless steel, making it easier to observe changes in grain size. A signal generator was connected to the power supply and provided different square wave intensities based on frequency and vibration amplitude to the shaker device, allowing different vibration conditions to be applied. The TS for these tests was set at 60 mm/min while the WFS was set at 300 mm/min. Cooling time between the deposition of a layer and the next was kept at 2-3 minutes, while pure argon gas was used as shielding gas.

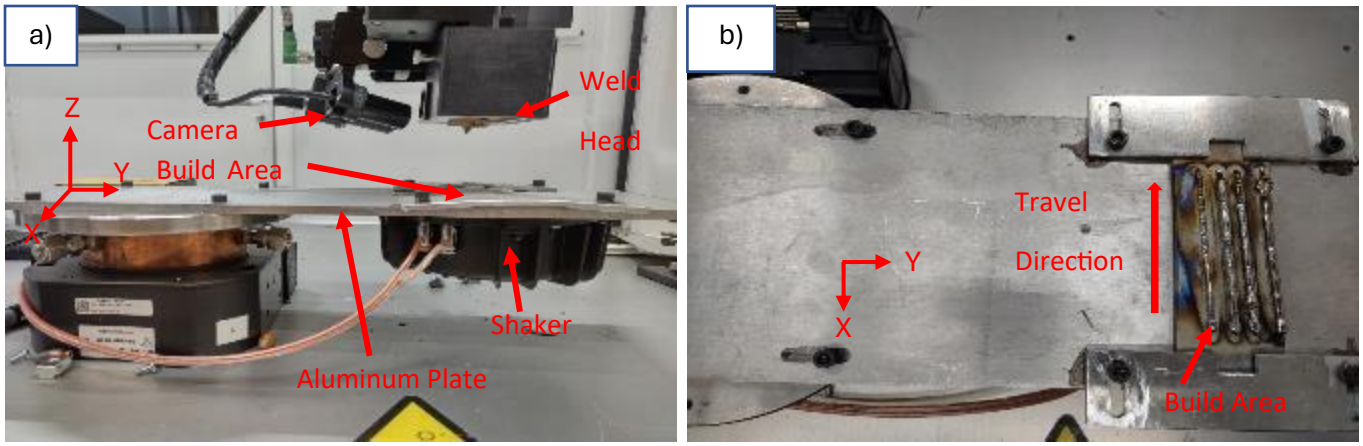

Figure 3-3: Grain Refinement Setup showing a) front and b) top views

3.2.1 Titanium Samples

To compare different frequency and amplitude conditions for vibration for titanium, 4-5 layers were deposited at different vibration conditions. Initial beads were assessed at an amplitude of 100 W and at an increasing frequency from 100 Hz to 600 Hz according to a linear ramp. Subsequent beads were assessed at a ramp for frequency from 50 to 100 Hz at amplitude powers of 4, 25, 100, and 155 W. *Table 3-2* shows all process parameters for the beads created. Microstructures were taken by mounting cross sections of the welds across the X axis corresponding to the travel direction, as seen in *Figure 3-3b.* The specimens were polished using conventional sandpaper grinding for a flat surface followed by 9-, 6-, and 1-µm diamond polishing. Vibratory polishing was performed for three hours using 0.04 µm colloidal silica suspension. Samples were etched using Keller's reagent.

Table 3-2: Process parameters used for titanium beads

Parameters	Frequency (Hz)	Amplitude (W)	Current (A)	Voltage (V)	Travel Speed (mm/min)	Wire Feed Speed (mm/min)	Shielding Gas
Bead 1	600-100	100	25	22	60	300	Argon
Bead 2	50-100	4					
Bead 3	50-100	25					
Bead 4	50-100	100					
Bead 5	50-100	155					

3.2.2 Steel Samples

Similar to titanium samples, 4-5 layers were deposited, and microstructures were taken by mounting cross sections of the welds also across the X axis. Beads were assessed at increasing ramp frequencies from 50 to 100 Hz at amplitude powers of 24.9 and 99.5 W. Frequencies of 100-600 Hz were not investigated for steel after results for titanium samples showed the range of 50-100 Hz to be more ideal for grain refinement. *Table 3-3* shows all process parameters for the beads created. Samples were polished according to the same procedure mentioned in section 3.1.2 for both regular and vibratory polishing. Samples were then etched using Marble's reagent.

Table 3-3: Parameters used for steel welds

Parameters	Frequency (Hz)	Amplitude (W)	Current (A)	Voltage (V)	Travel Speed (mm/min)	Wire Feed Speed (mm/min)	Shielding Gas
Bead 1	50-100	25	25	22	60	300	Argon
Bead 2	50-100	100					

3.3 Dynamic Deposition Height Correction

3.3.1 Height Deviation Correction

The determination of the amount of volume of material being added throughout the deposition process based on variations within the WFS is crucial for the design of a controller that maintains a constant layer height. This is because it provides an idea of the adjustment that the controller will have to achieve with respect to the WFS to fix any height deviations within the layers. To do that, different ranges of WFS were used with respect to the benchmark value set at 250 mm/min. Firstly, ten to twenty layers using a WFS of 250 mm/min were deposited onto a stainless-steel plate. As a follow up to the initial layers, three different values of WFS were then used based on a ±60% variation from 250 mm/min. Hence, the beads now being deposited are divided into three parts based on three different WFS values, which are 100, 250, and 400 mm/min. In total, ten layers, each divided into three segments based on WFS parameters, were deposited on top of the initial ten to twenty layers. This procedure was initially attempted for WFS variations of ±10%, ±25%, ±40% but also for variations of TS.

Cross sections were taken for every segment and were then polished and electro-etched in oxalic acid using an austenitic stainless-steel cathode at 6 V for 60 seconds for microstructural analysis. Height and width measurements were taken for each layer to calculate the corresponding volume of material added for a variation in the WFS. For each of the ten layers for a specific WFS, five different height and width measurements were used and averaged for best statistical accuracy. Vickers micro-hardness tests were also performed to determine any change in the hardness between the three segments due to WFS changes. The volume of material added served as basis for manual fixing of height deviations.

Chapter 4

Anisotropy in Wire Arc Additive Wall

This chapter provides a detailed outline of the investigation of the effect of anisotropy in a printed wall using WAAM for the MPAW process. It particularly discusses its significance on the stiffness and the relationship between the stiffness and the orientation of grains along the build direction.

4.1 Microstructural Characterization

The microstructures produced by WAAM in the thin wall have an elongated secondary dendrite structure as shown in cross sections obtained from locations M1, M2, M3, and M4 as depicted in *Figure 4-1a*, *Figure 4-1b*, *Figure 4-1c*, and *Figure 4-1d*, respectively. The microstructures of the WAAM 316LSi wall consist of austenitic and a small fraction of interdendritic ferritic in well-aligned sub-grains that vertically orient forming large columnar cell structures along the build direction. No porosity was detected in any of the specimens, which is a common feature associated with the MPAW for stainless steel particularly when using shielding gas of the high purity used here. Hence, determining the amount of oxygen in the as-built sample was unnecessary. The presence of sigma phase was not expected considering no annealing or heat treatments were performed nor were the heat input and interpass temperature exceptionally high. Since the interpass temperature was kept low at 107 C, sigma phase was not expected. Recent studies have shown that sigma phase is only likely in this alloy if later heat treatment is applied, however it can be controlled by selecting higher heat treatment temperatures [61]. The microstructures show that the preferential alignment grains and their growth is along the building direction across the XZ plane. Along with the secondary dendrites structure, the optical micrographs also reveal the remelted zones (RZ) at the layer interfaces, as shown in *Figure 4-1b*. The solidification structure of the WAAM mainly consists of γ-austenite and δ-ferrite, the latter present in different

morphologies which vary with the heat flow direction. δ-ferrite is present in columnar (*Figure 4-1a* and *Figure 4-1b*) and vermicular (*Figure 4-1c* and *Figure 4-1d*) morphologies along the build and travel directions respectively.

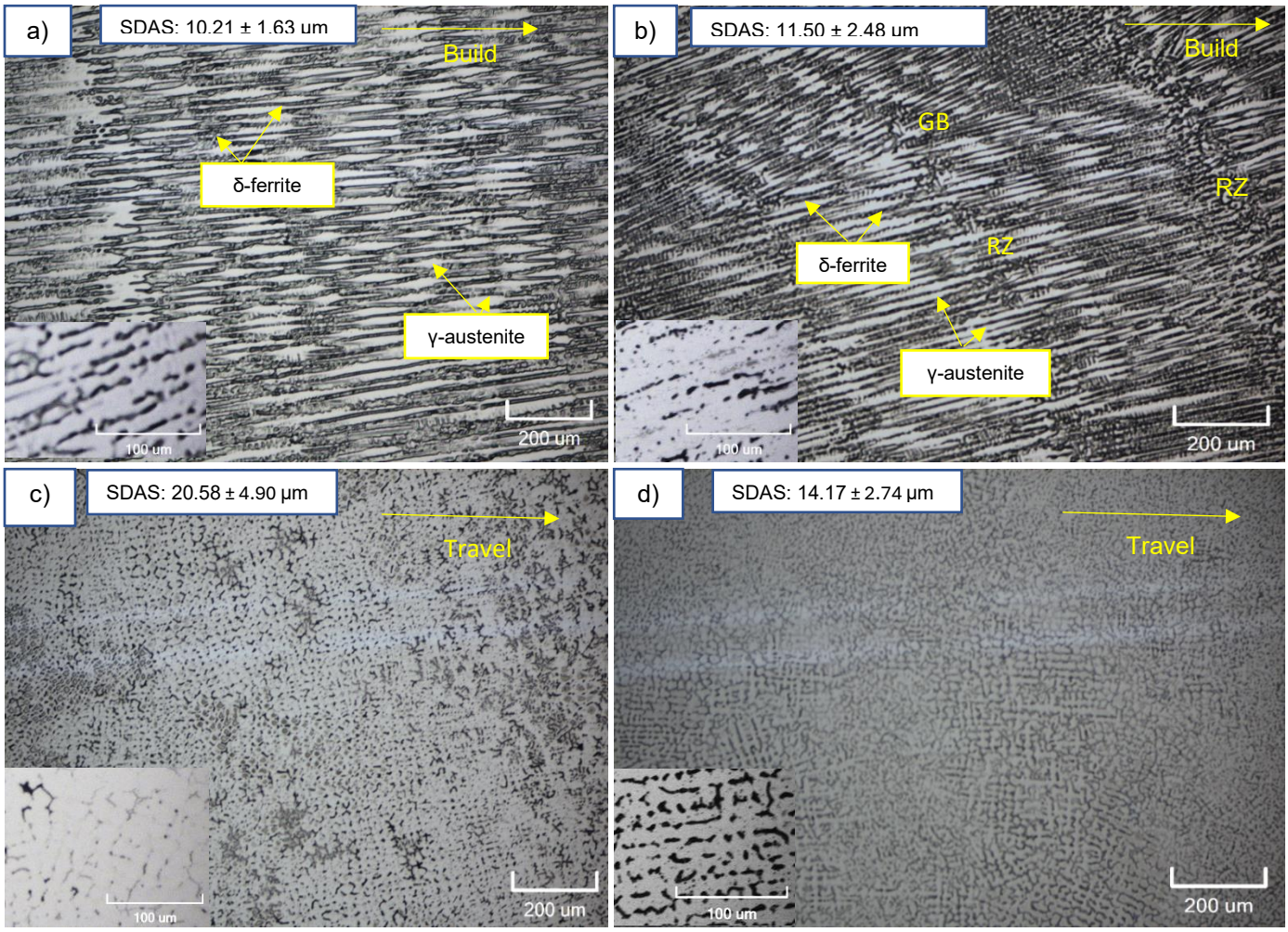

Figure 4-1: Optical micrographs highlighting the microstructures of samples a) M1 b) M2 c) M3 d) M4. b shows the layers of reheated zones (RZ) as well as the grain boundary (GB)

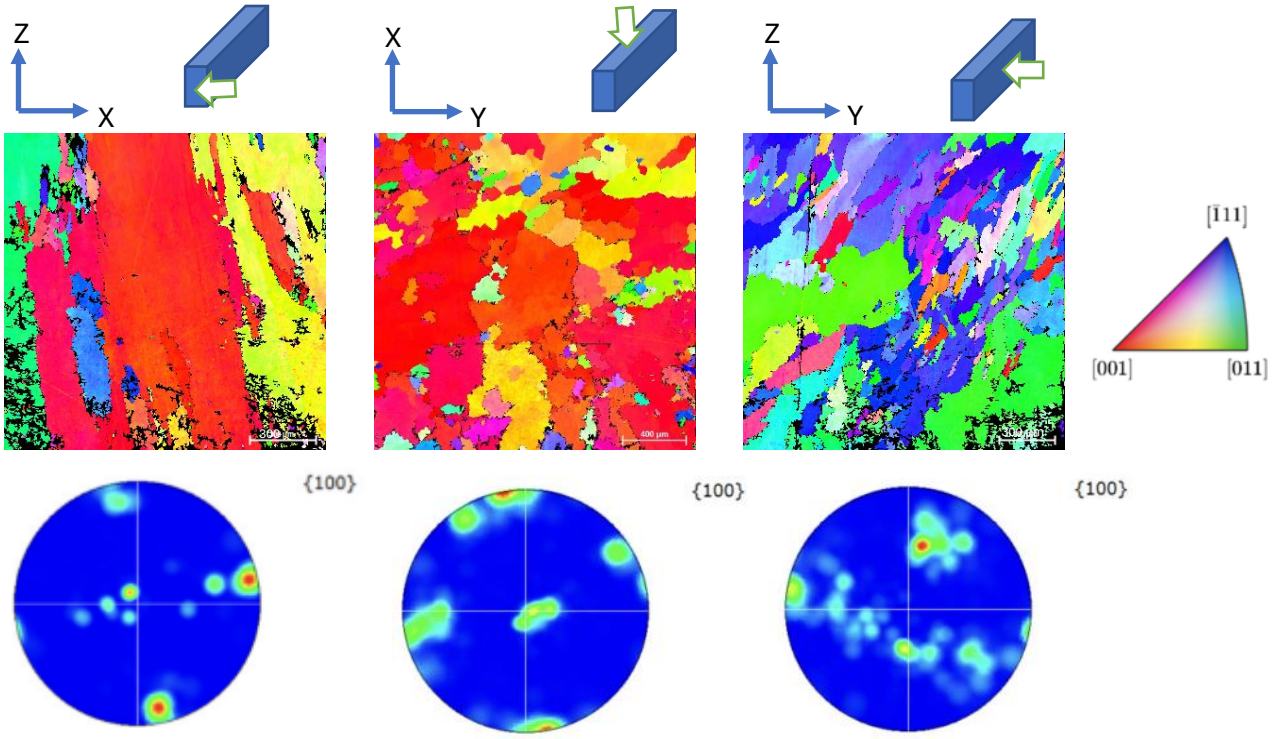

Figure 4-2: Austenitic crystal orientations maps of the a) XZ, b) XY, and c) YZ planes presented as inverse pole figures (IPF) and pole figures related to the austenite phase highlighting the preferential texture in the <100> direction corresponding to the build d

The volume of δ-ferrite was calculated by taking six different micrographs at different locations and using the line point intersection method. The microstructure of sample M4 contains finer cells (with an average SDAS of 14.17 µm) and a higher fraction of δ-ferrite (20.8%) compared to sample M3, which has a ferrite concentration of 17.2% and an average SDAS of 20.58 µm. This is most likely due to small differences in the thermal gradient and the closer distance of M4 to the substrate, which sustain higher cooling rates. Also, analyzing another sample from the top view taken even closer to the substrate, the ferrite concentration was found to be about 25%. This may suggest that as the cooling rate increases, the amount of δ-ferrite increases due to the material being less susceptible to solidification cracking. This is confirmed through the investigation of a different wall produced and analyzing the ferrite content based on three different distances from the substrate at 4 different sections, shown in *Figure 4-3*. This suggestion was also presented in previous work where one research paper compared the ferrite

concentration of different walls with different heat input and interpass temperature [28]. The effect of cooling rate on ferrite content was also seen for Cold-Metal Transfer WAAM [62].

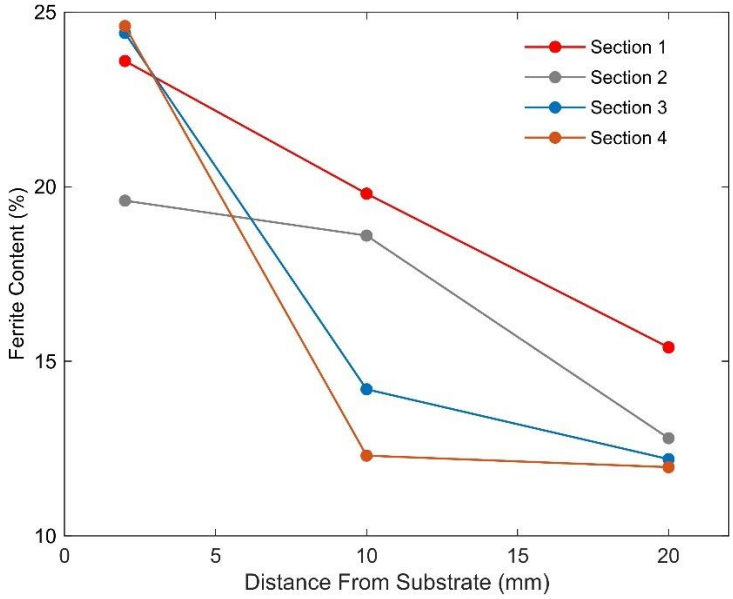

Figure 4-3: Ferrite concentration based on distance from substrate for 15 mm (section 1), 55 mm (section 2), 85 mm (section 3), and 115 mm (section 4) from starting point of deposition

Grain structures produced by rapid solidification in the AM processes often acquire highly oriented structures, which are revealed using microscopy that distinguishes crystal orientation or texture [33] [63]. The orientation of these grains can be clearly revealed by EBSD analysis, and *Figure 4-2a*, *Figure 4-2b*, and *Figure 4-2c* show the γ-austenite crystal orientation map along the building, travel, and transverse directions. The preferred orientation occurs in the <100> direction along the building direction as highlighted by the vertical red columnar grains in the XZ direction as well as the pole figures, particularly confirmed by that of *Figure 4-2b*. As explained by Rappaz and Dantzig [64], this can be explained by the easy growth direction corresponding to the <100> direction for cubic crystal structures, which is also due to the maximum temperature gradient occurring in this direction, hence the presence of large columnar grains. Similar development of this cube texture has been observed in various other AM processes, including in stainless [65] and titanium alloys [32] [66].

4.2 Mechanical Tests

The tensile properties of AISI 316LSi samples fabricated by WAAM were evaluated and stress strain curves were plotted as shown in *Figure 4-4* while the properties data are expressed as mean ± 95% confidence interval for the three samples, as summarized in *Table 4-1*. The stress-strain behavior for both of the orientations measured involves a considerable degree of work hardening which is typical for AISI 316 alloy weld metals.

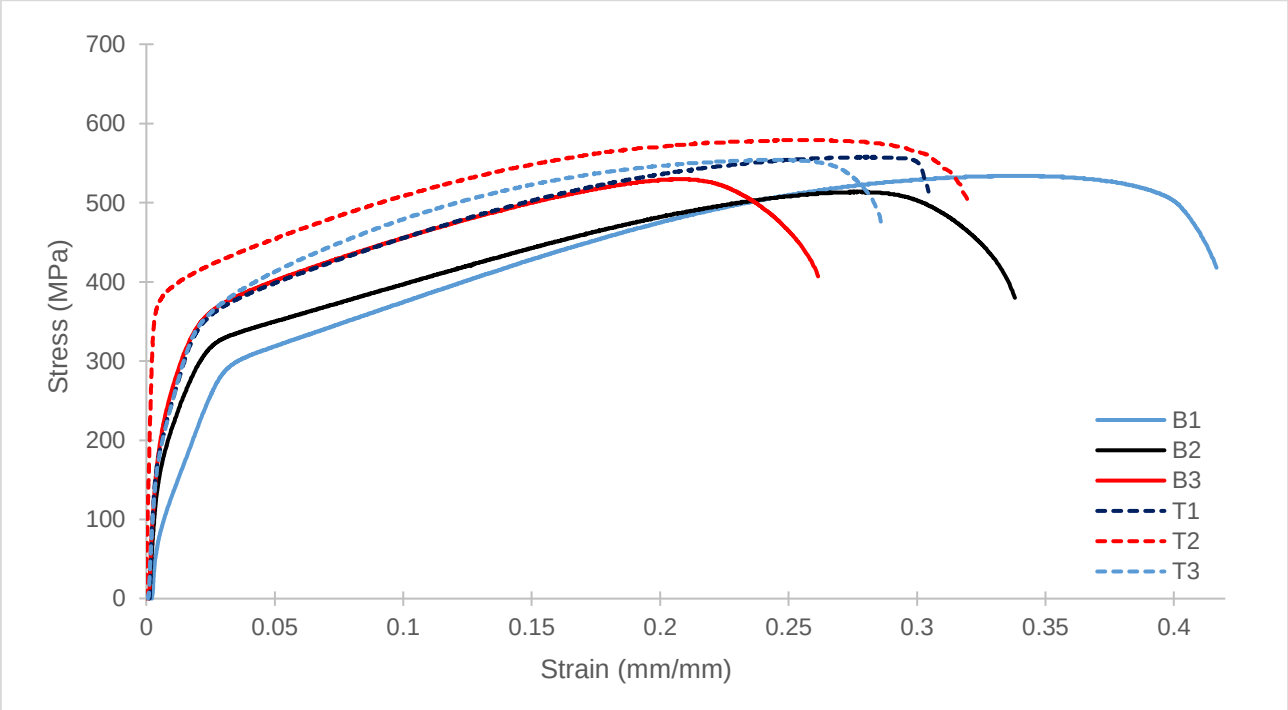

Figure 4-4: Stress-strain curve of tensile samples in build (B1, B2, and B3) and travel directions (T1, T2, and T3)

The statistical analyses revealed that the orientation of the specimens has a significant effect on the mechanical properties of the as-built wall. The samples extracted horizontally, which correspond to the direction of travel of the torch, have better overall mechanical properties than those in the build direction. Samples in the travel direction exhibit a yield stress and tensile strength of 326 MPa and 564 MPa respectively, which are comparable to the values in the build direction (*Table 4-1*). Yield stresses were found to differ by 8 MPa while tensile strengths were found to differ by 38 MPa. Similar

differences and uniformity between the properties were also found in Cunningham's work [28], which also used low currents based on the employed of low heat inputs of 0.26 kJ/mm and 0.47 kJ/mm, close to the heat input used in the present work, found to be 0.31-0.41 kJ/mm. These mechanical properties are comparable to those in the present work particularly for yield and tensile stresses, as shown in *Table 4-2*. Low heat input may play an important role in lowering Young's modulus values, which would explain the lower values of Young's modulus in *Table 4-1*.

Table 4-1: Average mechanical properties of 316LSi in the build and travel directions

	Young's Modulus (GPa)	***Yield Stress (MPa)***	***Tensile Strength (MPa)***	***Elongation (%)***
Build Direction	*79.5±6.8*	*318±23*	*526±10*	*32±7*
Travel Direction	*105.2±20.7*	*326±35*	*564±12*	*30±1.5*

Table 4-2: Mechanical Properties obtained for low and high heat input and interpass temperature [28]

		Young's Modulus (GPa)	***Yield Stress (MPa)***	***Tensile Strength (MPa)***
Low Heat Input – High Interpass Temperature	*Average*	*121.2±16.3*	*308.1±16.6*	*562.2±32.6*
	Horizontal	*130.1±19.1*	*313.8±14.8*	*549.4±34.5*
	Vertical	*112.2±7.7*	*302.4±19.2*	*572.9±32.5*
High Heat Input – Low Interpass Temperature	*Average*	*179.2±42.7*	*320.2±26.9*	*570.9±22.1*
	Horizontal	*192.0±50.6*	*330.7±34.4*	*582.2±21.4*
	Vertical	*166.5±38.9*	*309.8±17.08*	*559.6±19.5*

The specimens in the travel direction have an average elongation of 30% compared to 32% provided by the specimens in the build direction although much greater scatter in the elongation is observed for tests along the build direction. This indicates that on average, greater ductility is associated with the build direction, although there is an increase in scatter. However, it should be noted that at such

large strains, the total elongation may become more sensitive to potential imperfections or discontinuities, which explains the elongation scatter between individual samples. Hence, scatter seen within the elongation of samples is expected. The results align with studies that suggest that higher strength and lower elongation are present when more grain boundaries are encountered [28]. Based on the microstructures shown in *Figure 4-1c* and *Figure 4-1d*, the lack of directional grain growth and hence the random orientation of grains in the travel direction explains the higher number of grain boundaries, which results in higher strength and lower elongation. The slight spread in the elastic regions for specimens may be due to small differences in the gain structure and orientation.

The anisotropic properties of 316LSi wall fabricated by WAAM and reflected through the difference in properties along the build and travel directions can be compared to the work performed by Cunnigham et al. [28], in which higher mechanical properties were observed along the travel direction compared to the build direction. *Figure 4-4* also reveals a negligible increase in strength associated with samples along the travel direction, and this was concluded when comparing individual samples apart from each other further along the travel direction. Thus, sample B3 displays the highest ultimate strength (534 MPa) out of the build direction samples B1 and B2, both of which are behind B3 along the travel direction, while samples T1, T2, and T3 all have higher ultimate strengths than B3 and are further along the travel direction. Furthermore, looking at the stress strain curves of samples B1, B2, and B3, we can see that the ductility of B1 is higher than B2 followed by B3, indicating a decrease in the ductility along the travel direction. This may be associated with the difference in ferrite concentration in samples M1 (17.2 %) and M2 (6.8 %), although this is not evident in the results presented. Overall, the samples in the build and travel direction were found to have very close yield strengths as well as similar elongations and tensile strengths, indicating the uniformity of the fabricated part associated with the low heat input of the MPAW process.

However, significant differences can be noted with respect to the Young's moduli of the travel and build directions. *Figure 4-4* shows that the elastic slope is lowest for B1, followed by B2, and B3, which are then followed by the other three samples, which are further along the travel direction. This suggests an increase in Young's modulus along the travel direction, while the delta fraction decreases along the same direction.

Furthermore, some additional tests were performed for an off-the-shelf 316L steel sheet undergoing hot rolling. Tensile specimens were taken both along the rolling and transverse directions and the ultimate tensile strengths were found to be 678 and 687 MPa respectively. These values are higher than those of the as-built steel, and this is as a result of the finer equiaxed grains obtained through recrystallization in the hot rolling process. However, while WAAM does present lower mechanical properties, it has much greater flexibility in terms of creating complex geometries, something that is not found when using sheet materials. In terms of moduli of elasticity, the steel sheet had an average of 37 and 36 GPa along the rolling and transverse directions, which are significantly lower than those obtained by WAAM.

To quantitively evaluate the stiffness anisotropy, the theoretical value for Young's modulus in the <100> direction was also calculated based on the standard equations using the compliance coefficients of a single crystal below [67]:

$$\frac{1}{E_{hkl}} = s_{11} - 2\left[(s_{11} - s_{12}) - \frac{1}{2}s_{44}\right]\frac{h^2k^2 + k^2l^2 + h^2l^2}{h^2 + k^2 + l^2}$$

where s_{11}, s_{12}, and s_{44} are the elastic compliance constants given by the equations:

$$s_{11} = \frac{c_{11} + c_{12}}{(c_{11} - c_{12})(c_{11} + 2c_{12})} = 0.0127\frac{1}{GPa}$$

$$s_{12} = -\frac{c_{12}}{(c_{11} - c_{12})(c_{11} + 2c_{12})} = -4.83 \times 10^{-3}\frac{1}{GPa}$$

$$s_{44} = \frac{1}{c_{44}} = 7.43 \times 10^{-3} \frac{1}{GPa}$$

The values for the elastic constants of austenite were obtained based on those extracted by Hutchinson et al. [68] using the calculated lattice constants obtained at 927ºC for iron where c_{11}, c_{12}, and c_{44} are 148.81, 91.63 and 134.55 GPa respectively. This leads to an E_{100} value of 78.74 GPa for the Young's modulus along the <100> direction. This theoretical value calculated for the stiffness is quite similar to the measured Young's modulus value along the build direction and confirms the anisotropic stiffness response of the material due to epitaxial growth of grains in the <100> crystals along the build direction.

Furthermore, no significant difference in plastic deformation can be observed between the samples of the build and travel direction. *Table 4-3* shows the ratio of yield strength to ultimate strength for individual samples in the build and travel directions as well as the average in both directions, revealing the almost identical value of the average ratio. Also, R-values based on the plastic region up to the ultimate tensile strength were also calculated for both build and travel directions in *Table 4-4*, revealing a greater deformation in width along the travel direction.

Table 4-3: Yield strength to ultimate tensile strength ratio for samples in build and travel directions

$\frac{\sigma_y}{UTS}$	***Sample 1***	***Sample 2***	***Sample 3***	***Average***
Build Direction	*0.54*	*0.60*	*0.64*	*0.59*
Travel Direction	*0.56*	*0.64*	*0.54*	*0.58*

Table 4-4: R values for samples in build and travel directions

R-Value	*Sample 1*	*Sample 2*	*Sample 3*	*Average*
Build Direction	*0.42*	*0.50*	*0.31*	*0.41*
Travel Direction	*0.86*	*0.73*	*0.32*	*0.64*

The microhardness maps were produced along 3 x 20 mm areas for samples M1, M2 and M4 as shown in *Figure 4-5a*, *Figure 4-5b*, and *Figure 4-5c*. These indicate that the hardness was overall quite uniform in each of the specimens, with an average of 183 ± 1.2, 188 ± 1.7, and 200 ± 1.3, HV respectively. These values are comparable to those of literature used through selective laser melting [63]. It can be seen however that there is an increase along the travel direction since M1, M2, and M4 are successively along the travel direction. This aligns with the tensile results showing an increase in strength along the travel direction. There also seems to be a general decrease in the microhardness along the build direction, as shown by samples M1 and M2 in *Figure 4-5a* and *Figure 4-5b*. This trend can also be confirmed through the findings of Cunnigham et al. [28] which tested the effect of different heat inputs and cooling conditions as well as in the work of Chen et al. [26]. The effect of anisotropy may also influence the hardness values, due to the orientation of the indenter, as this has been found to occur in steel weld metals in prior work [69]. However, due to the complex stress distribution formed around a Vickers indenter, any hardness anisotropy will not be as clear as the observed differences in Young's modulus.

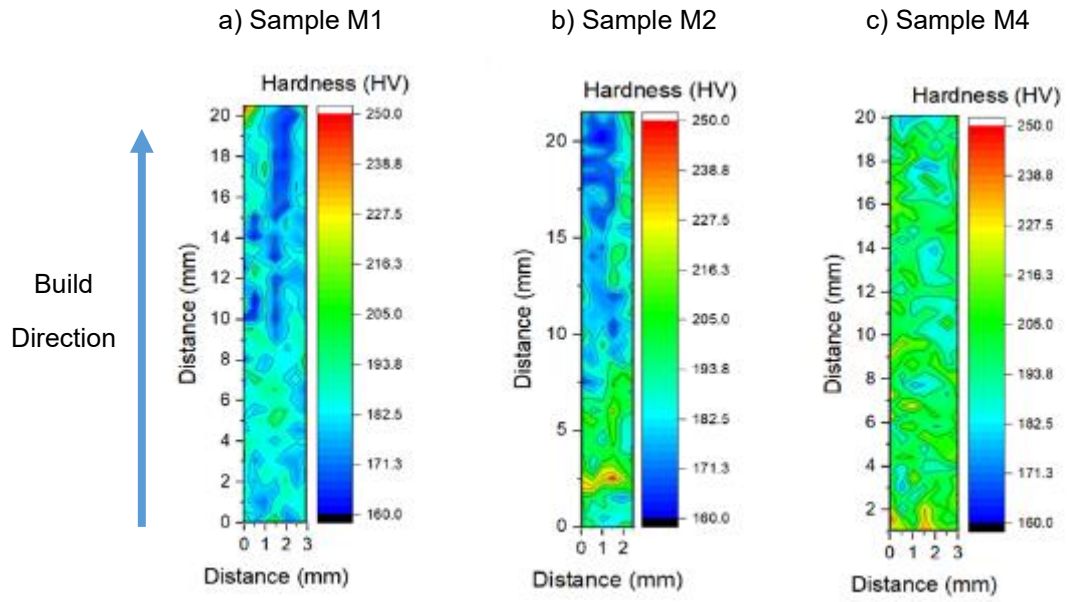

Figure 4-5: Vickers Hardness Profiles versus direction distance from substrate for samples a) M1, b) M2, and c) M4

4.3 Summary

This chapter investigated the capability of additively manufacturing a slender wall structure with nearly uniform properties and no porosity. Hence, although lower in deposition rates than other processes, such a type of process may be suitable for repair of metal parts, in which higher precision and low heat inputs are required. Cooling times to reach an interpass of 150 C were also found to be around one minute as a result of the low heat input, making it especially suitable for part repair applications where embrittled materials are used for example. The strength properties of the fabricated material exhibited nearly uniform yield strength properties of 318 to 326 MPa, and 526 to 564 MPa ultimate tensile strength values for the build and transverse directions respectively. Likewise, the hardness varied from 183 to 200 HV across different locations in the built plate. The uniformity in properties is desirable in part repair applications as well. However, the stiffness of the material exhibited fairly anisotropic properties ranging from 79.5±6.8 GPa along the build direction to 105.2±20.7 GPa in the travel

direction. This stiffness anisotropy was confirmed to be due to the strong preferred orientation of the <001> crystals during solidification along the build direction, which were observed by EBSD analysis and confirmed to have produce a lower stiffness value which correlated well with the observed measurement.

Chapter 5
Vibratory Weld Conditioning

This chapter investigates the effect of vibration of the workpiece during deposition on grain size by varying the frequency and the amplitude for stainless steel and titanium layers.

5.1 Deposition of titanium with vibration

Initially, titanium beads were deposited using a square waveform at an increasing frequency from 100 Hz to 600 Hz at a pulse amplitude of 100 W are shown in *Figure 5-1*. The microstructures revealed increased grain nucleation and finer grains in *Figure 5-1d* compared to *Figure 5-1a, Figure 5-1b*, and *Figure 5-1c*. This occurred close to the 100 Hz range, which led to a focus on the investigation of frequency ranges from 50 to 100 Hz. Microstructures are revealed in *Figure 5-2* obtained at a power amplitude from the signal generator of 4 W and show major breaking down of grains closest to the substrate. Increasing the amplitude to 100 W while maintaining frequency ranges of 50-100 Hz revealed no significant changes in terms of microstructures, as shown in *Figure 5-3*. The same can also be noticed when analyzing the samples at an amplitude of 155 W, as shown in *Figure 5-4*. The increased presence of grain nucleation closer to the substrate was noticed for all amplitudes when investigating the microstructures and the refinement of grains closest to the substrate can be confirmed by the 3D plots shown in *Figure 5-5*, which reveal a clear difference in grain size between distances of 400 and 3000 μm from the substrate. The plots also served to confirm the low effect of amplitude on the grain size while frequency variations revealed significant difference in average grain size for both 400 and 3000 μm distances from the substrate.

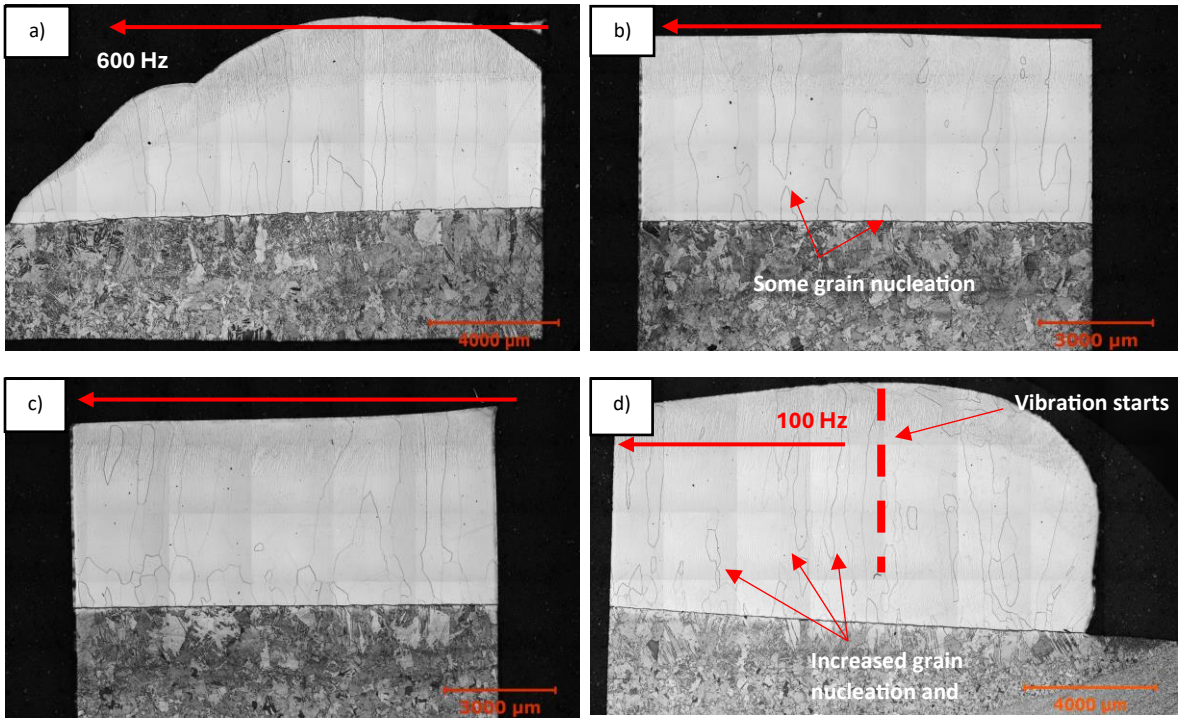

Figure 5-1: Titanium bead composed of five layers. Vibration was applied for frequencies ranging from 100 Hz to 600 Hz in a linear ramp at an amplitude of 100 W per pulse. The sections shown in a, b, c, and d highlight the sample bead in decreasing frequency from 600 Hz to 100 Hz

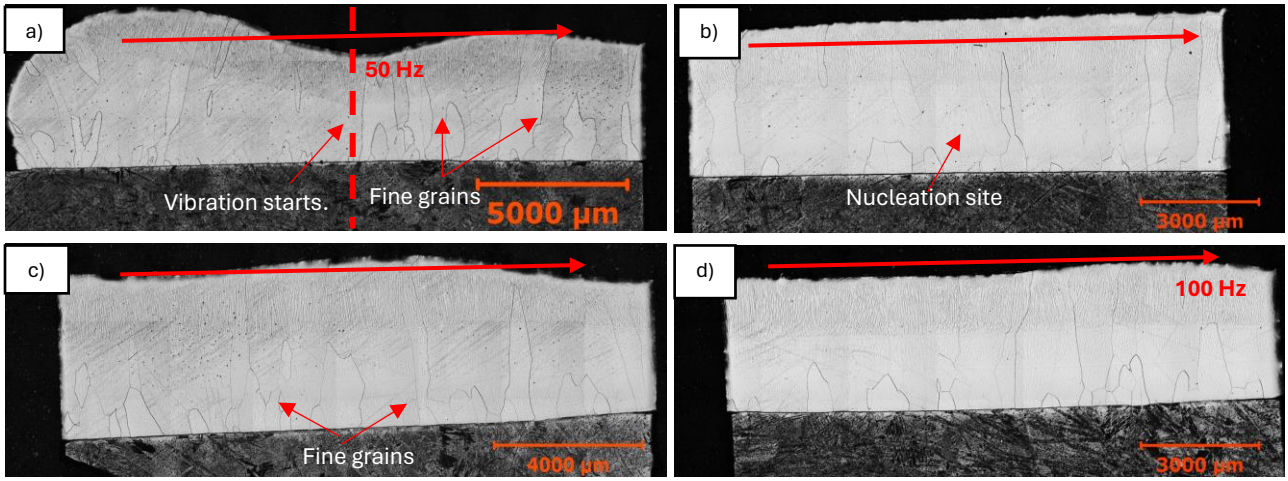

Figure 5-2: Titanium bead composed of five layers. Vibration was applied for frequencies ranging from 50 Hz to 100 Hz in a linear ramp at an amplitude of 4 W per pulse

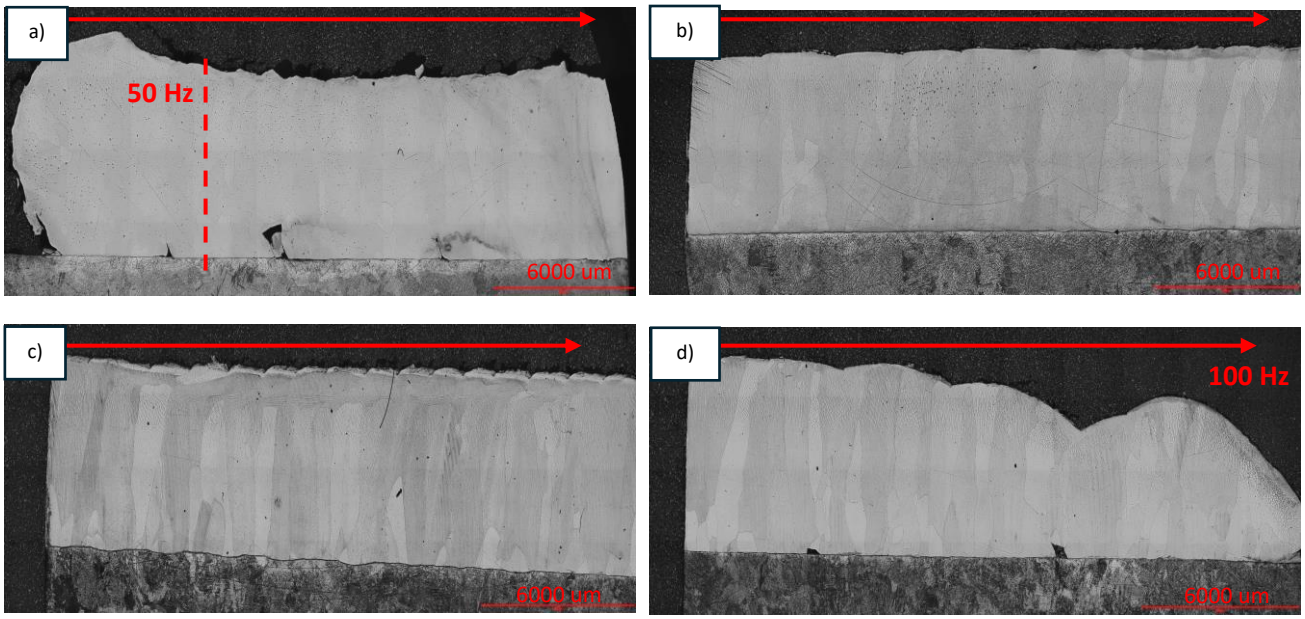

Figure 5-3: Titanium bead composed of five layers. Vibration was applied for frequencies ranging from 50 Hz to 100 Hz in a linear ramp at an amplitude of 25 W per pulse

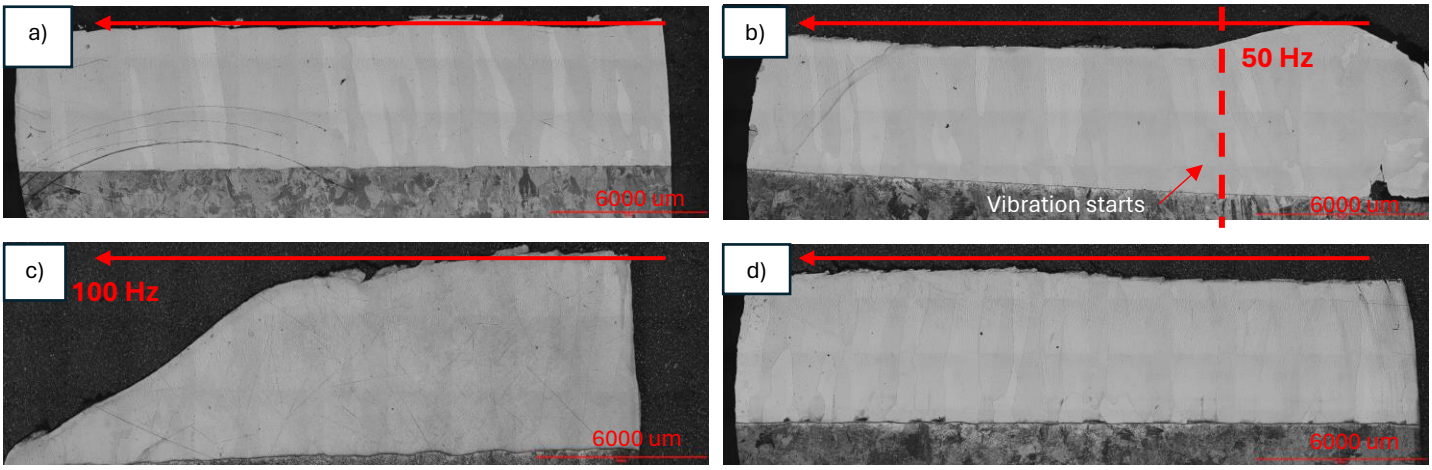

Figure 5-4: Titanium bead composed of five layers. Vibration was applied for frequencies ranging from 50 Hz to 100 Hz in a linear ramp at an amplitude of 155 W per pulse

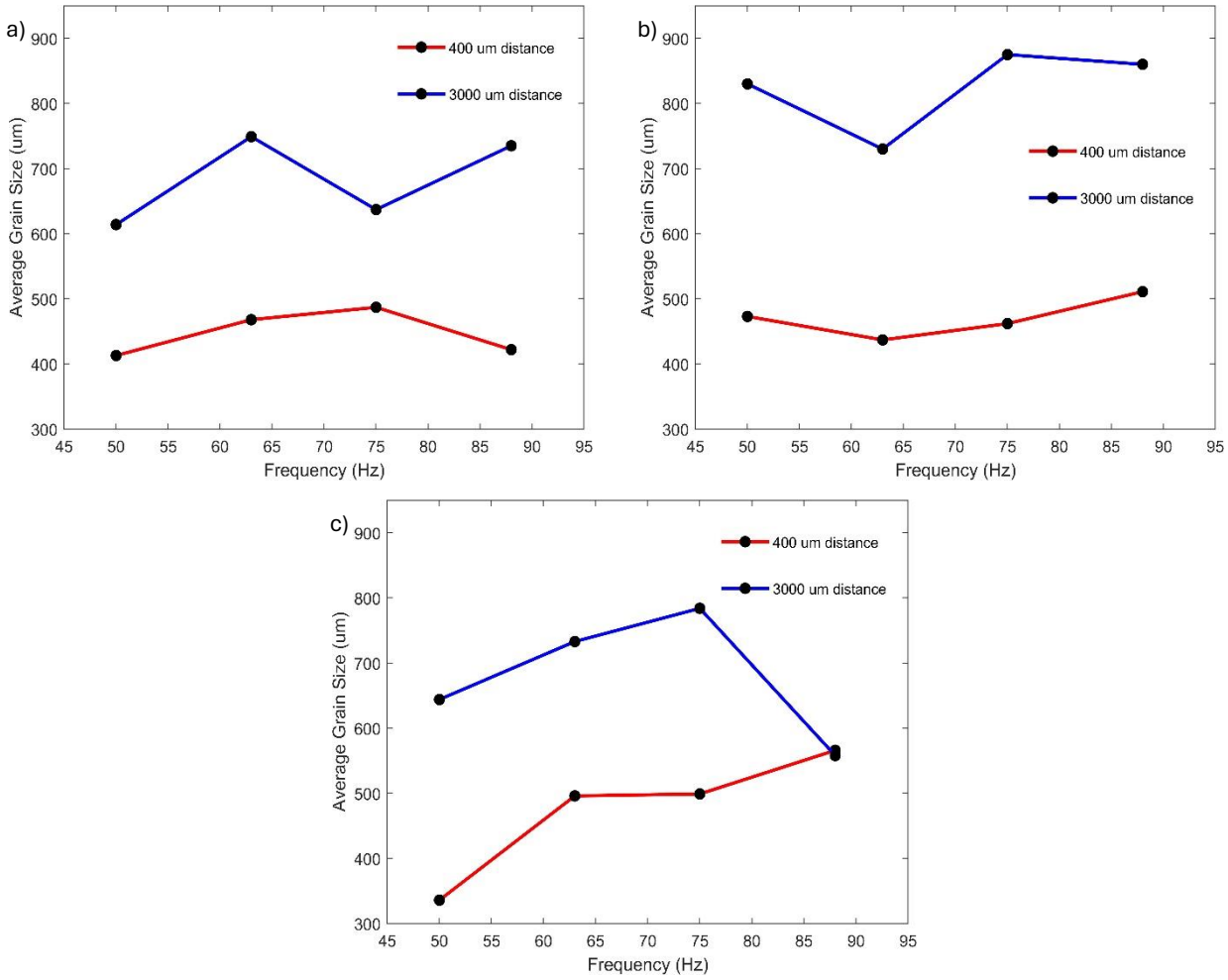

Figure 5-5: Average grain size for titanium layers with respect to distance from substrate and frequency range for amplitude of a) 25 W b) 100 W and c) 155 W

5.2 Stainless Steel Welds

When analyzing stainless microstructures, the determination of the SDAS was used to properly investigate any changes in the sub-grain sizes. *Figure 5-6* and *Figure 5-10* reveal the macro-graphs of the entire deposited material for amplitudes of 25 W and 100 W, respectively. At each amplitude, the top and bottom parts at sections 1, 2, and 3 are highlighted in *Figure 5-6* and *Figure 5-10* and micrographs were investigated. These micrographs are shown in *Figure 5-7, Figure 5-8*, and *Figure 5-9* for an amplitude of 25 W and in *Figure 5-11*, *Figure 5-12*, and *Figure 5-13* for an amplitude of 100 W. Comparing the different SDAS, it can be seen that as the frequency increases from 50 to 100 Hz,

there is no significant change in SDAS at the top layers irrespective of the amplitude chosen. However, the same cannot be said for the bottom layers, in which there is significant difference in SDAS with variation in frequency. This is the case when investigating the micrographs at both 25 W and 100 W amplitude. Comparing the SDAS at the bottom layers for both 25 W and 100 W, all seem to be around the same range of 12-18 µm. Despite the SDAS being slightly lower at 25 W (7-8 µm) than those at 100 W (9-10 µm), the amplitude does not seem to have a significant impact on the disruption of the solidification mechanism. Similar to the case of titanium samples, the frequency has a considerable effect on SDAS size at the regions close to the substrate, which also reveal a greater presence of equiaxed grains compared to the top regions, which reveal more columnar grains. The change in SDAS is summarized in *Figure 5-14*.

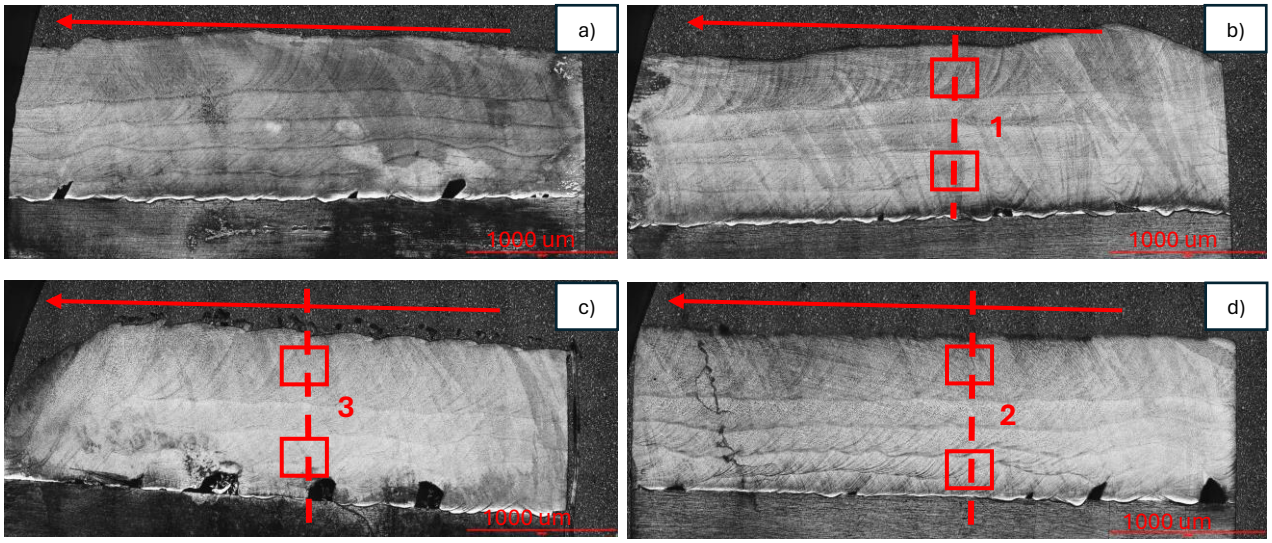

Figure 5-6: Stainless Steel Welds composed each of 5 layers for frequencies ranging from 50 to 100 Hz in a linear ramp increase at 25 W amplitude

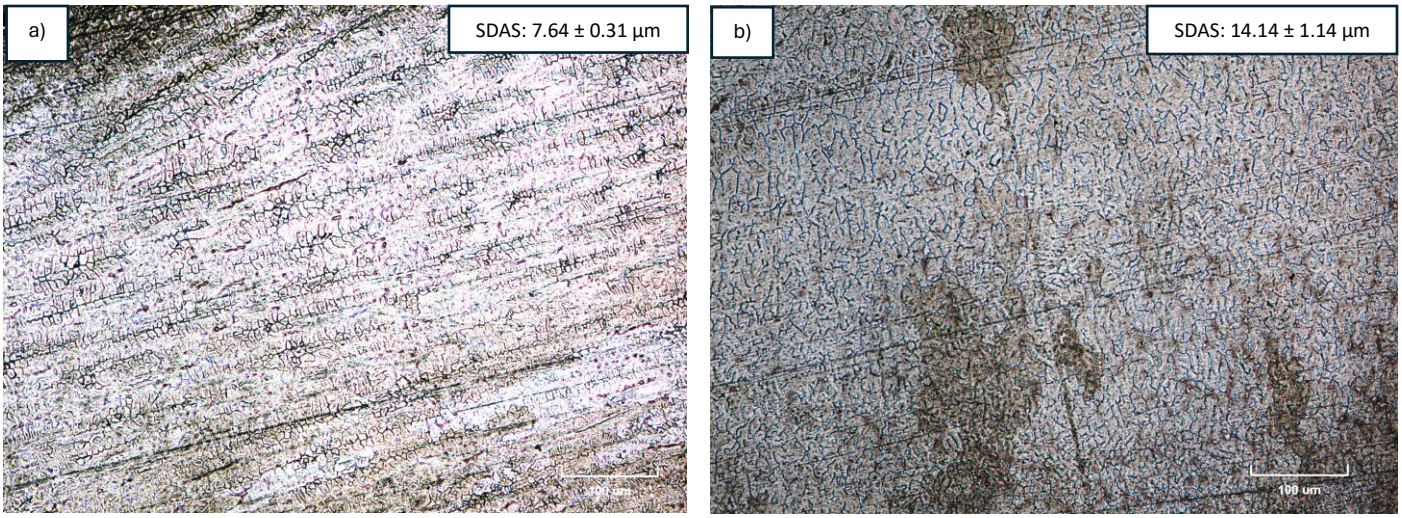

Figure 5-7: Micrographs of a) top and b) bottom sections for taken from section 1 for 25 W amplitude

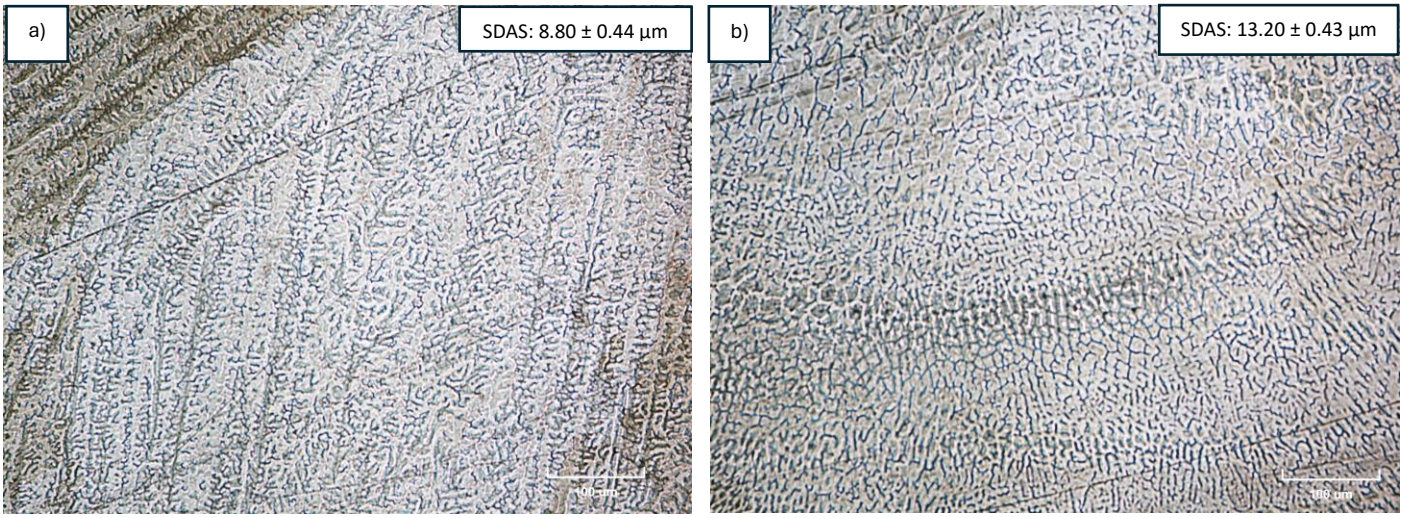

Figure 5-8: Micrographs of a) top and b) bottom sections for taken from section 3 for 25 W amplitude

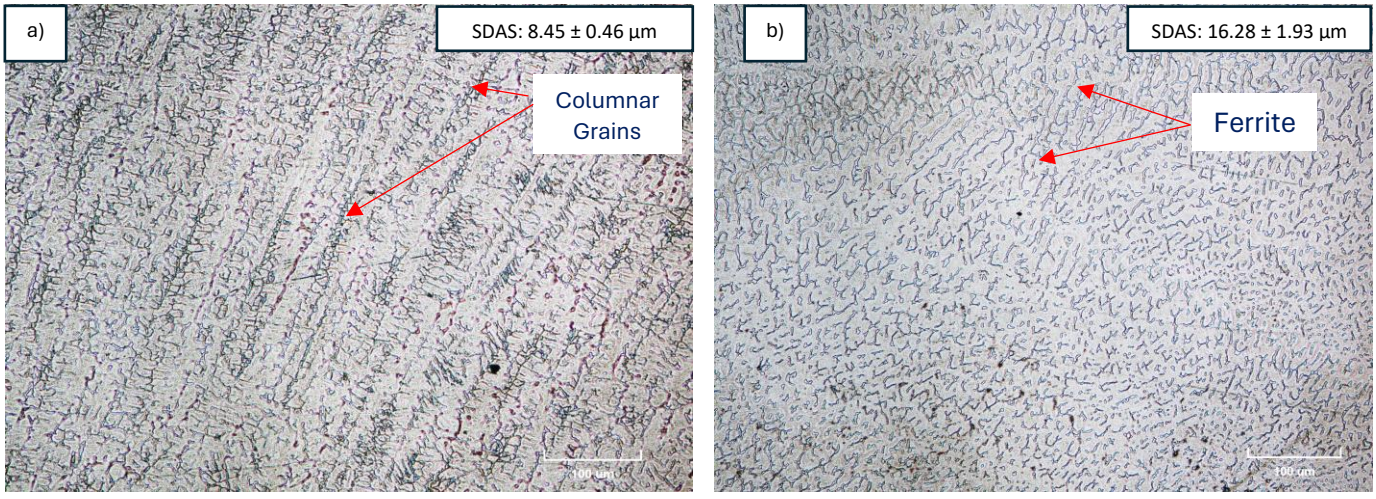

Figure 5-9: Micrographs of a) top and b) bottom sections for taken from section 4 for 25 W amplitude

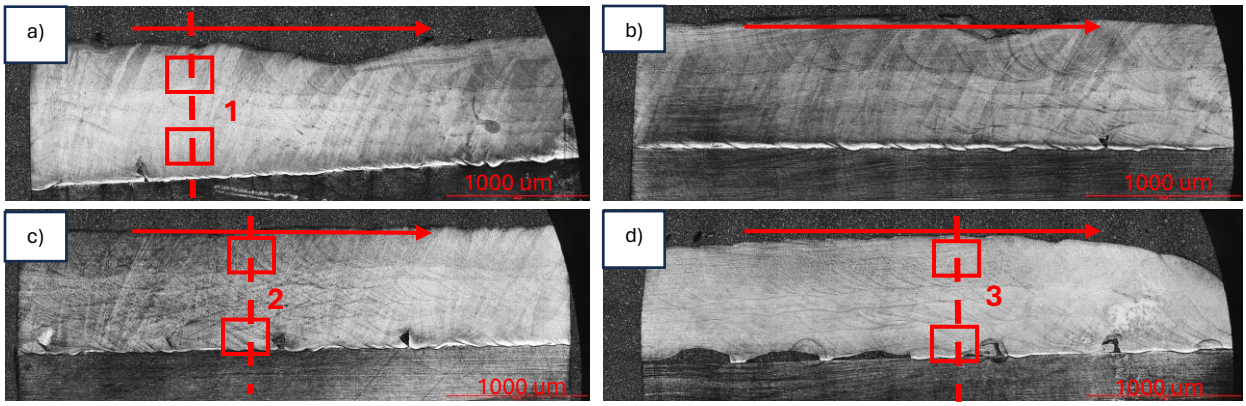

Figure 5-10: Stainless steel welds composed each of 5 layers for frequencies ranging from 50 to 100 Hz in a linear ramp increase at 100 W amplitude

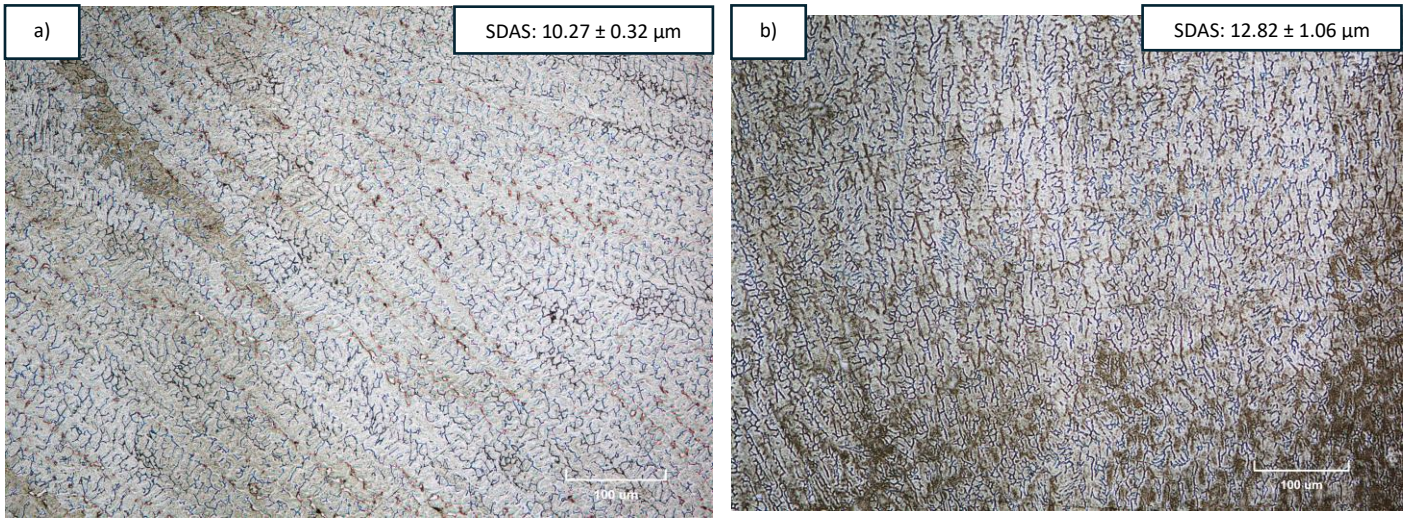

Figure 5-11: Micrographs of a) top and b) bottom sections for taken from section 1 for 100 W amplitude

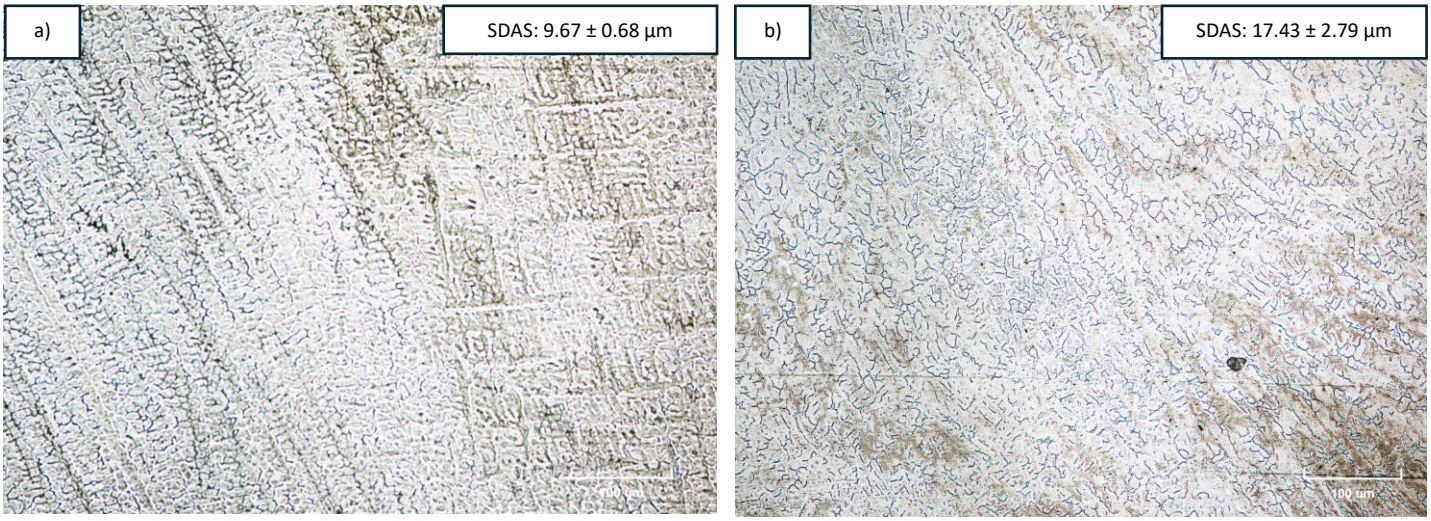

Figure 5-12: Micrographs of a) top and b) bottom sections for taken from section 3 for 100 W amplitude

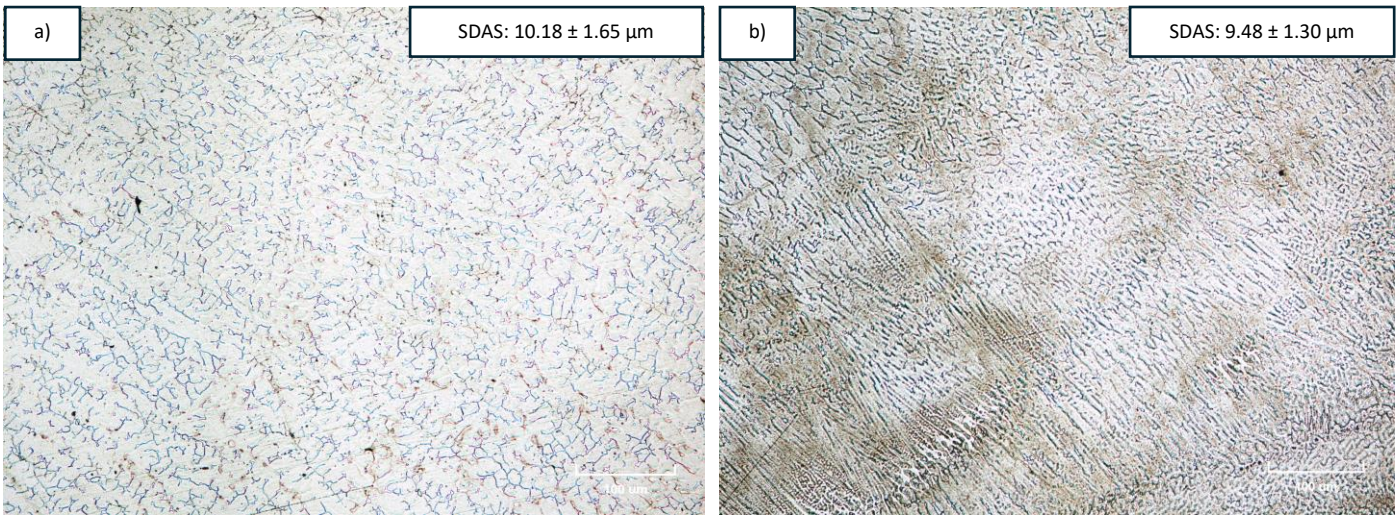

Figure 5-13: Micrographs of a) top and b) bottom sections for taken from section 4 for 100 W amplitude

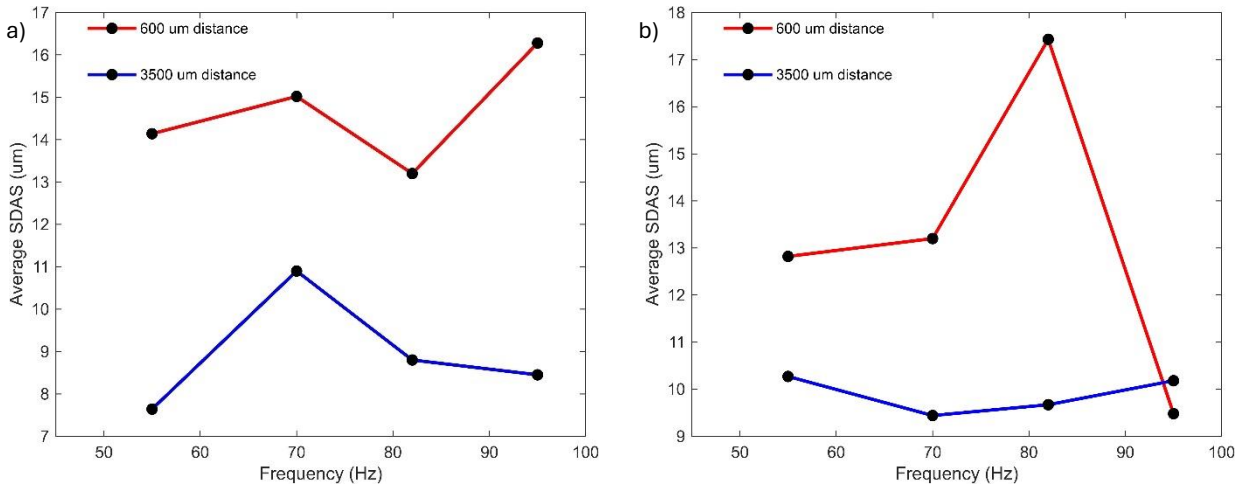

Figure 5-14: Average SDAS at various frequencies and for 600 and 3500 µm from substrate

While tensile samples were not machined and tested in this chapter, the yield strength can be estimated in the case of stainless-steel samples using the Hall-Petch equation, which predicts that the yield strength of a material can be increased with a decrease in grain size. The equation is as follows:

$$\sigma_y = \sigma_0 + \frac{k_y}{\sqrt{d}}$$

Where σ_y is the yield strength, σ_0 is the original yield strength, k is a constant unique to the material, and d is the grain size. In the case of stainless steel, the grain size is replaced with the SDAS. The value

of k was obtained from literature for 316 stainless steels based on the strain rate mentioned in chapter 3.1.3. The values of σ_0 were taken from the average yield strength values obtained in the build direction from Table 4-1. SDAS values were obtained from taking the averages of the yield strength values for the top and bottom sections at amplitudes of 25 and 100 W found in the table. The estimated yield strength values are displayed in Table 5-1.

Table 5-1: Estimated yield strength values obtained by the Hall-Petch equation for the top and bottom sections at amplitudes 25 and 100 W

Location, Amplitude	$\boldsymbol{k\ (MPa \cdot m^{0.5})}$	$\boldsymbol{\sigma_0\ (MPa)}$	$\boldsymbol{SDAS\ (\mu m)}$	$\boldsymbol{\sigma_y\ (MPa)}$
Top, 25 W			8.3	428
Bottom, 25 W	326	318	14.5	404
Top, 100 W			10	421
Bottom, 100 W			13.2	408

5.3 Summary

This chapter investigated the effect of amplitude and frequency of vibrations, applied mechanically to the workpiece, on the melt pool during deposition for both titanium and stainless-steel samples. Results revealed that amplitude had no significant effect on the fragmentation of columnar

dendrites or grain size. This was the case for both stainless and titanium layers. However, frequency around the range of 50-100 Hz yielded fine grains around the substrate, and this was particularly evident by the analysis of the SDAS at the bottom regions for stainless-steel samples.

Chapter 6
Dynamic Deposition Height Correction

This chapter evaluates the performance of automatic voltage control for the MPAW process. This is evaluated by measuring how precisely the WFS can be adjusted to obtain a more uniform layer height. It also looks into the optimal overlap percentage for adjacent beads on a flat surface.

6.1 Wire Feed Speed Variations and Volume Added

Prior to attempting layer height corrections, the amount of metal material being added to the substrate as a result of variations within the WFS were investigated. This knowledge provided an insight into the action that the controller must perform to achieve the desired deposition height. Hence, different WFS ranges were investigated to properly determine the amount of volume added onto the substrate. *Figure 6-1* shows the final part generated based on WFS values of 100, 250, and 400 mm/min and respective cross sections were analyzed. These can be seen in *Figure 6-2a*, *Figure 6-2b*, and *Figure 6-2c* which highlight the first ten layers from the top. For each of these layers, the width was obtained from one measurement while the height was obtained from taking the average of multiple measurements.

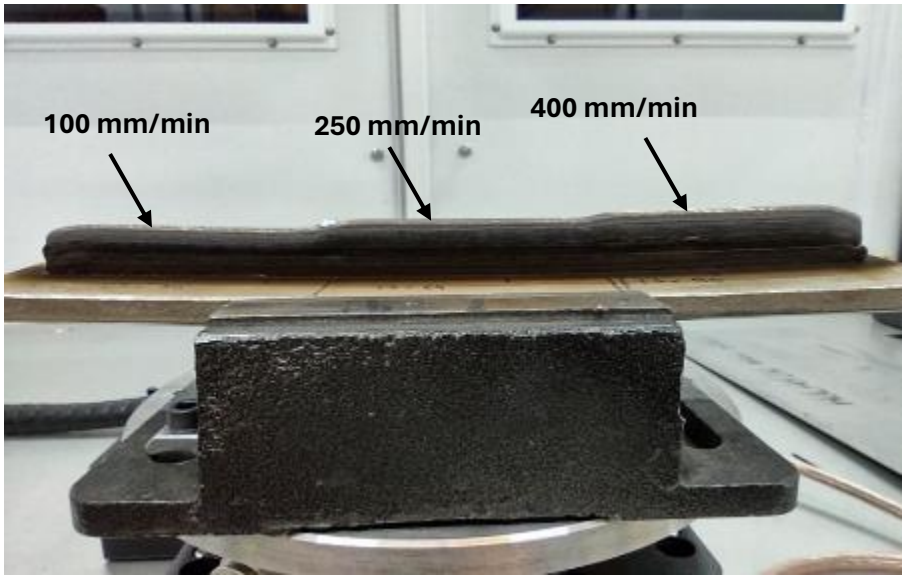

Figure 6-1: Final component generated and divided into three segments based on WFS of 100, 250, and 400 mm/min

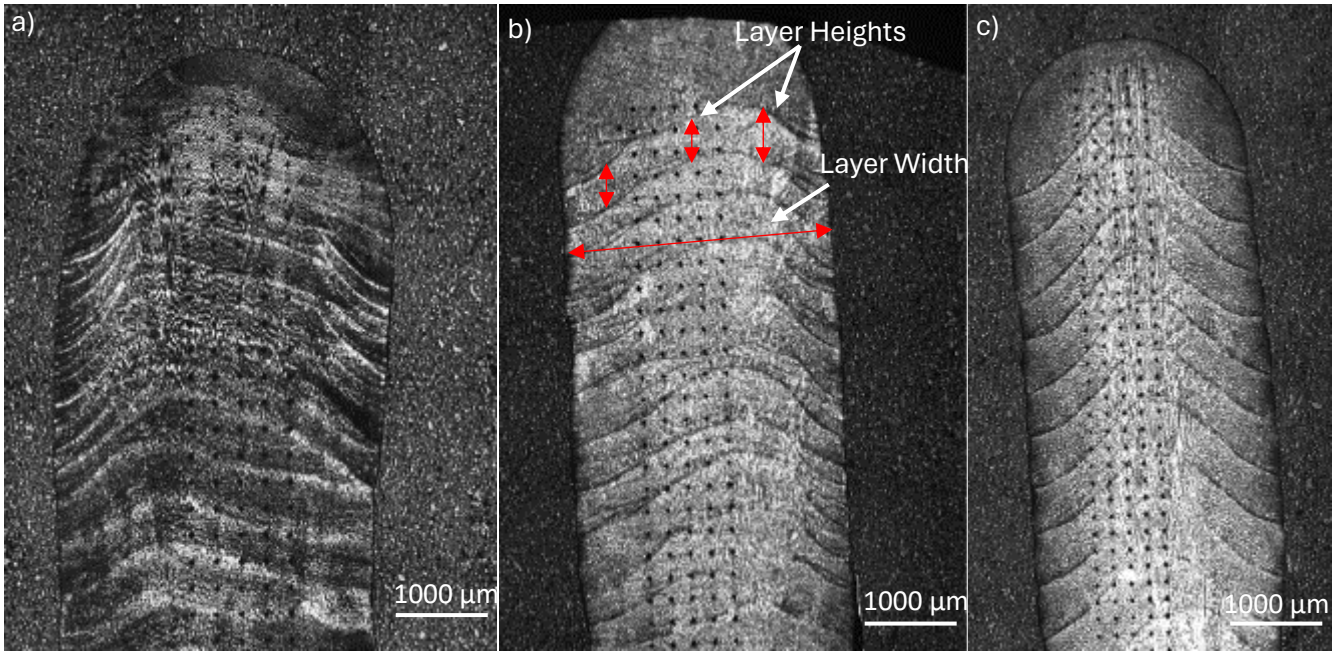

Figure 6-2: Cross sections showing the top ten layers for a WFS of a) 100 mm/min b) 250 mm/min and c) 400 mm/min

Table 6-1: Height and Width Measurements for WFS of 100 mm/min

Layers	H1 (µm)	H2 (µm)	H3 (µm)	H4 (µm)	H5 (µm)	W1 (µm)	W2 (µm)	W3 (µm)	W4 (µm)	W5 (µm)
L1	804	922	1272	1300	1370	2587	3105	3371	3678	3370
L2	224	140	154	119	231	3872	3869	3867	3870	3867
L3	182	161	154	203	147	3863	3856	3876	3868	3869
L4	145	140	119	168	231	3382	3890	3920	3883	3905
L5	224	287	260	252	203	3911	3904	3896	3895	3904
L6	175	161	161	210	140	3889	3889	3882	3882	3896
L7	252	301	210	252	168	3885	3903	3910	3904	3917
L8	189	189	182	154	210	3903	3917	3897	3919	3903
L9	224	203	196	217	224	3891	3877	3884	3889	3875
L10	175	238	210	196	154	3861	3847	3840	3855	3854

Table 6-2: Height and Width Measurements for WFS of 250 mm/min

Layers	H1 (µm)	H2 (µm)	H3 (µm)	H4 (µm)	H5 (µm)	W1 (µm)	W2 (µm)	W3 (µm)	W4 (µm)	W5 (µm)
L1	1489	1620	1450	1100	1554	2849	3276	3567	3696	3739
L2	442	550	475	464	460	3751	3767	3766	3794	3806
L3	356	399	442	442	356	3797	3818	3825	3845	3836
L4	503	615	561	529	561	3847	3890	3901	3835	3876
L5	367	529	604	604	540	3850	3852	3844	3870	3858
L6	388	496	576	594	540	3858	3879	3901	3923	3870
L7	626	460	356	281	489	3903	3913	3944	3925	3912
L8	518	518	575	547	550	3925	3916	3928	3921	3934
L9	460	417	345	345	575	3921	3916	3904	3934	3934
L10	691	590	561	561	460	3876	3856	3816	3869	3826

Table 6-3: Height and Width Measurements for WFS of 400 mm/min

Layers	H1 (µm)	H2 (µm)	H3 (µm)	H4 (µm)	H5 (µm)	W1 (µm)	W2 (µm)	W3 (µm)	W4 (µm)	W5 (µm)
L1	1496	1540	1122	1309	1209	3567	3883	4070	4228	4243
L2	705	676	691	748	777	4199	4257	4272	4286	4228
L3	791	878	748	633	676	4243	4257	4286	4300	4286
L4	633	604	719	734	791	4272	4272	4272	4243	4214
L5	777	820	777	576	849	4200	4300	4387	4358	4315
L6	676	691	734	705	648	4286	4300	4344	4372	4329
L7	748	806	777	763	820	4329	4344	4415	4401	4401
L8	705	705	820	806	820	4373	4373	4430	4387	4373
L9	777	748	604	763	763	4375	4376	4401	4320	4376
L10	791	719	806	863	777	4289	4332	4259	4202	4315

Table 6-4: Amount of Volume Added per layer

Wire Feed Speed (mm/min)	Average Layer Height (µm)	Average Layer Width (µm)	Cross sectional Area (mm^2)	Volume Added (mm^3/min)
100	194	3809	0.74	73.9
250	496	3825	1.90	474
400	743	4283	3.18	1273

Also shown in *Tables 6-1* to *6-4* are the different measurements of height and width that were taken for each layer at wire feed speeds of 100, 250, and 400 mm/min as shown in *Table 6-1*, *Table 6-2*, and *Table 6-3* respectively. These measurements were obtained from different locations for each layer and taken from the cross sections. The amount of volume of material being deposited per minute can be

seen in *Table 6-3* and was calculated by multiplying the average layer height, the average layer width, and the WFS with each other. Microstructures, as shown in *Figure 6-3*, revealed slight differences in terms of the SDAS size as well as the amount of ferrite, which was expected as a result of the difference in cooling rates. There is a clear refinement of the grain structure towards a more equiaxed and shorter grain morphology with higher travel speeds.

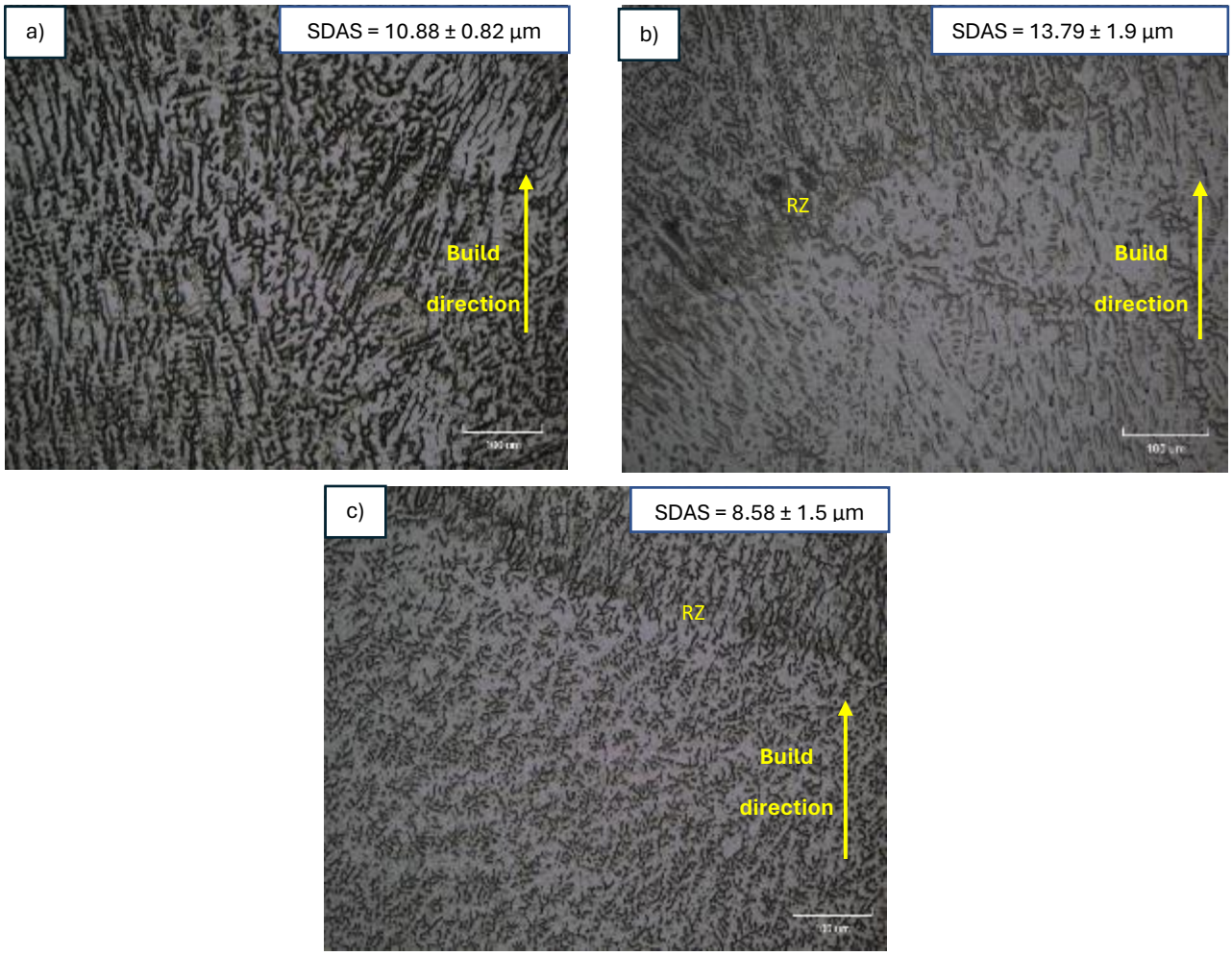

Figure 6-3: Microstructures taken from the middle region of the top ten beads for a) 100 b) 250 and c) 400 mm/min

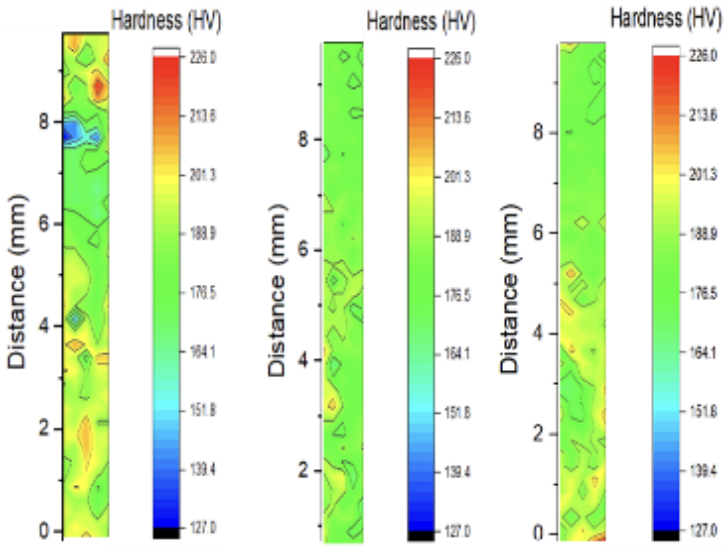

Figure 6-4: Hardness profiles for 100, 250, and 400 mm/min

6.2 Manual Height Deviation Correction

Due to the nature of the additive process, which involves arc welding albeit at low heat inputs, geometrical deviations from the desired part will occur, resulting in layer surfaces that are not flat. These deviations, which are occurring at every layer lead to a significant decrease in part quality upon final completion as a result of the accumulation of all these deviations layer by layer. Prior to the implementation of an automatic controller, which will automatically assist in height deviation correction, the WFS was manually adjusted, based on the height gaps witnessed for an individual layer as well as the calculated volume added per layer corresponding to WFS of 100, 250, and 400 mm/min. *Figure 6-5* shows height deviations that were present after the deposition of six layers. As can be seen in the figure, section "S2" of the bead has a height of 4.93 mm while the sections "S1" and "S3" have heights of 4.49 and 4.69 mm respectively. Hence, the next deposition run should yield a uniform height of 4.93 mm all throughout the bead. To do that, the WFS was modified accordingly in both sections "S1" and "S3" of the bead at the next run, while refraining from welding and depositing in section "S2" to maintain the same height of 4.93 mm. *Table 6-5* shows the calculations that were performed to

determine the appropriate WFS for sections “S1” and “S3”. The required WFS was calculated by first obtaining the weld cross-sectional area difference between S1 and S2 as well as that between S2 and S3. Then, linear interpolation was performed based on the cross-sectional areas obtained in Section 6.1 for WFS of 100, 250, and 400 mm/min, as shown in *Table 6-6*. The WFS required for S1 and S3 were found to be 232 and 128.5 mm/min respectively, which were applied at the next run while avoiding welding in region S2.

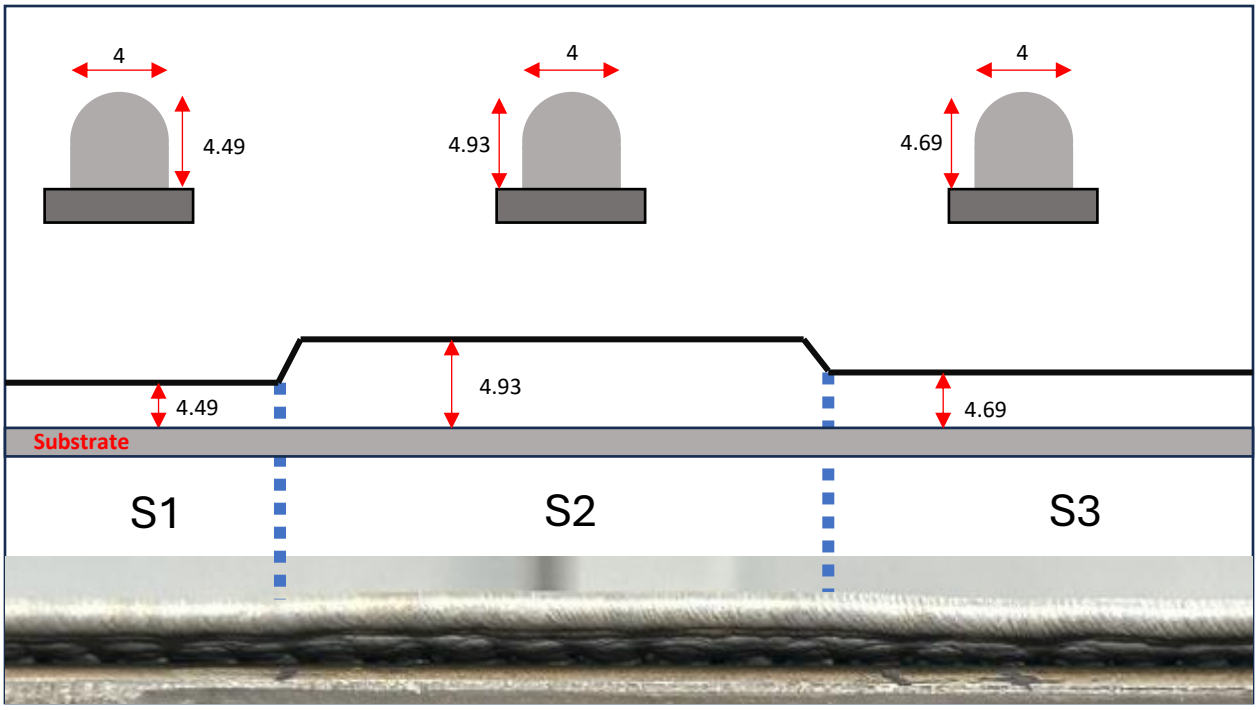

Figure 6-5: Height deviations after deposition of 6 layers. All dimensions are in mm.

Table 6-5: Calculation of required WFS for sections S1 and S3 based on the cross-sectional area difference between S1 and S2 as well as that of S2 and S3

	Bead Height Difference with S2 (mm)	**Cross-Sectional Area (Width*Height) (mm^2)**	**Required WFS (mm/min)**
S1	0.44	1.76	232
S3	0.24	0.96	128.5

Table 6-6: Cross-sectional area of weld beads produced by 100, 250, and 400 mm/min

WFS	Cross-Sectional Area
100	0.739
250	1.90
400	3.18

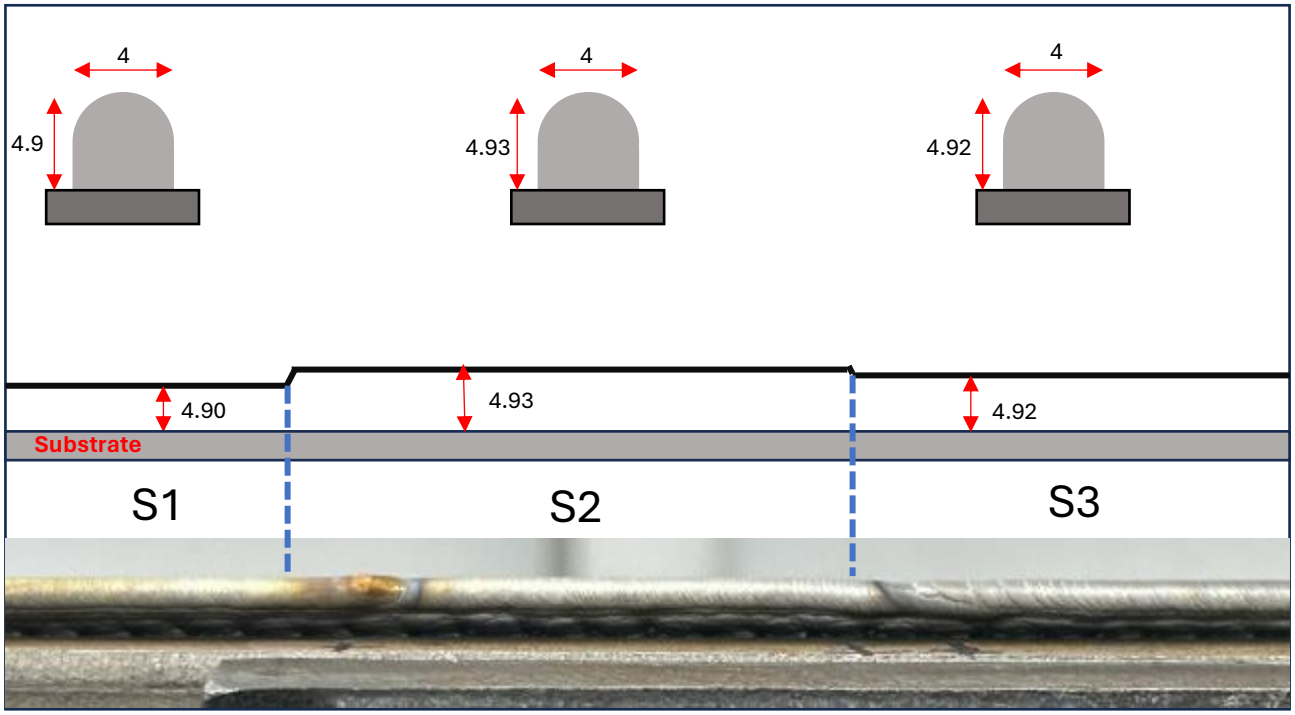

Figure 6-6: Height deviation correction after manual WFS adjustment. All dimensions are in millimeters

Following the deposition of metal in sections S1 and S3 based on the modified WFS, it was found that the heights of the welds were close to that of S2 with an error of no more than 0.03 mm, as can be seen in *Figure 6-6*. However, the start and stop locations of the weld produce some discontinuities, which is the main drawback behind the method used and hence, it is also important to modify the WFS all throughout the same run without any stops. This was also attempted by using the same method. However, it is less accurate since it requires assuming a volume of material for one section and trying to fix the other sections while also considering this new change in height. For example, looking at *Figure 6-7*, some layer height deviations exist after depositing more than 30 layers. For each

deposition run, cross sectional area differences were obtained by also considering the cross-sectional areas added to section S1' for a WFS of 100 mm/min. Final heights for sections S1', S2', and S3' can be seen in *Figure 6-8* after attempting to fix after three passes. Despite calculations performed after three passes and accuracies between the second and third layer, final heights were not all equal, highlighting the difficulty to attempt fixes using the current method for direct deposition over the entire layer.

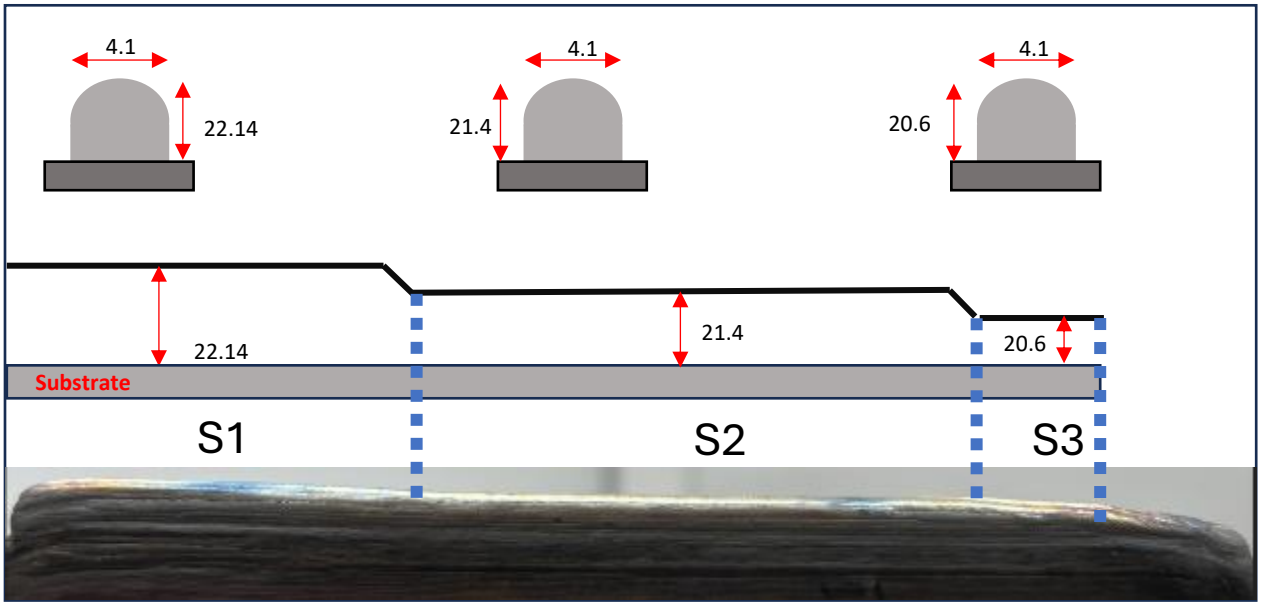

Figure 6-7: Height deviations after deposition of more than 30 layers. All dimensions are in millimeters

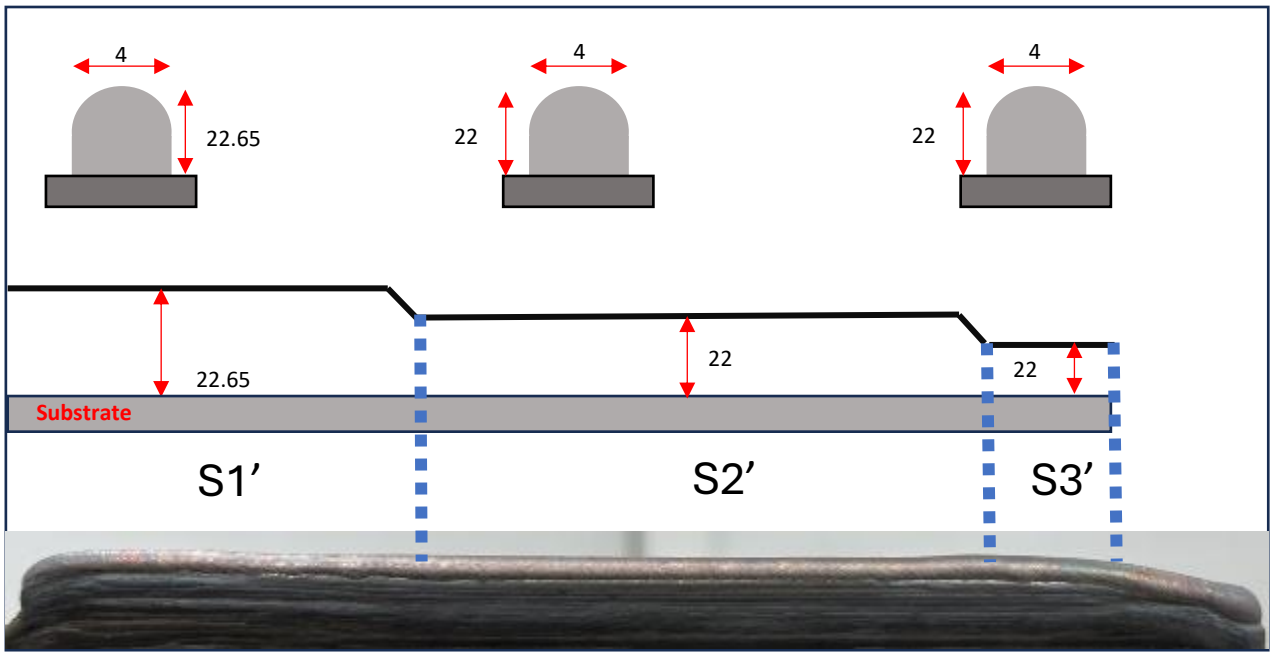

Figure 6-8: Manual correction of deposition height after three passes. All dimensions are in millimeters

6.3 Bead Overlaps

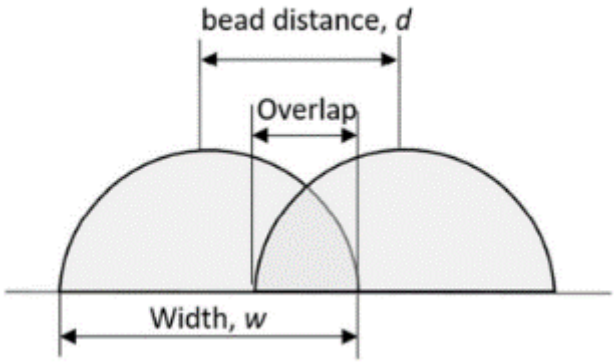

Figure 6-9: Schematic of overlap definition

When depositing multiple single-weld beads for a single layer, the distance between these beads is important when creating solid parts, which causes an overlap between two beads as can be seen in *Figure 6-9*. If the distance is too large, the surface of the layer becomes too uneven and causes lack of fusion when depositing beads for the subsequent layer. If the distance is too small, the overlapping between the beads becomes too large and causes excess material build-up. The overlap percentage is

calculated by subtracting the distance by the width from 1 and multiply by 100, as shown in the following equation:

$$Overlap\ (\%) = \left(1 - \frac{d}{w}\right) \times 100 \quad where\ d\ is\ the\ distance\ and\ w\ is\ the\ width$$

Based on the following equation, different distances were obtained based on different overlap parameters chosen to determine an optimal distance between single-weld beads. Initially, a current of 26 A was used for the first layer weld beads at overlapping percentages ranging from 0 to 75%, as shown in *Figure 6-10*. Beads were found to be too overlapped at 50, 60 and 75% while some improved wettability may be needed for beads overlapped at 10 and 20 %. Subsequently, a current of 35 A was also used for beads on plate at overlap percentages of 20, 50, 60, and 75 %, as shown in *Figure 6-11*. These did not have a flat surface as a result of the high heat input, which affected the first bead when depositing metal for the second bead. Similarly, beads at 50, 60, and 75% were significantly overlapped.

Figure 6-10: Weld beads at a current of 26 A for overlap percentages of 0, 10, 20, 30, 40, 50, 60, and 75 %

Figure 6-11: Weld beads at a current of 35 A for overlap percentages of 20, 50, 60, and 75 % (bottom to top)

Finally, the current was finally set at 30 A for bead on plate overlap testing. Overlap testing was performed through two stages. The first stage involves using a larger current to facilitate wetting between the filler metal and the substrate and hence, obtain the best overlap parameter based on good fusion and flat surface. The second stage involves adding subsequent layers using a reduced current value and obtaining an optimal overlap percentage based on the best fusion between the two beads. The steps can be summarized in *Figure 6-12*, which also shows the different overlap percentages that were chosen for the testing.

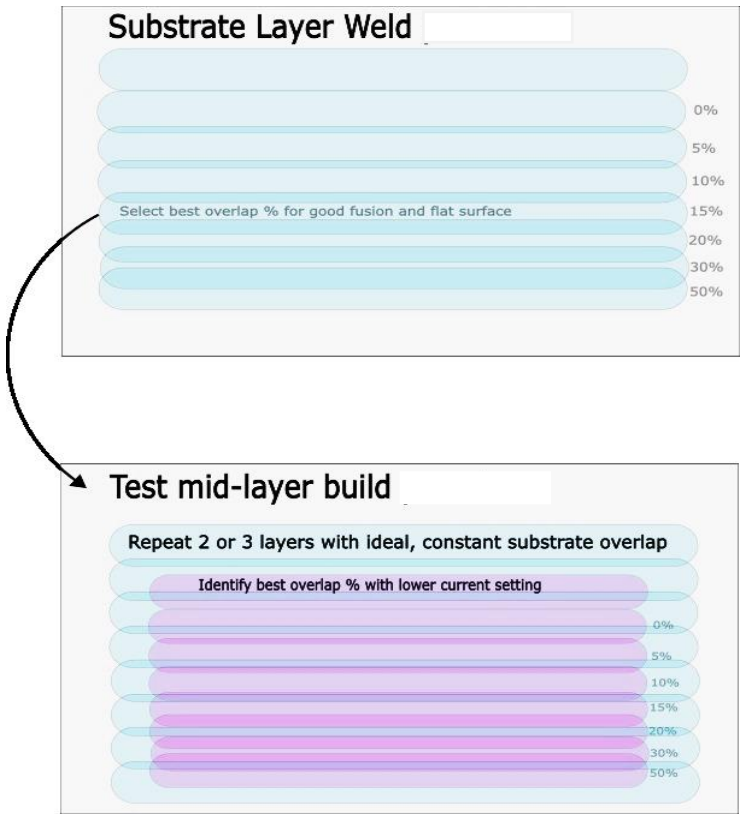

Figure 6-12: Overlap testing stages

Table 6-7 summarizes all the parameters that were used for each weld at all the overlap percentages for both stage 1 and stage 2. As previously mentioned, for the bead on plate (first layer), the current was set at 30 A. However, for subsequent layers, the current was set at 24 A. For stage 2, an additional overlap percentage (25%) was added for testing after noticing that the ideal percentage would fall between 20 and 30 %. Hence, for the first stage 1, it was determined that the ideal overlap percentage is 15%, as can be seen in *Figure 6-13*, while for the second stage, it was set at 25%, as can be seen in *Figure 6-14*. Macrostructures were also investigated to make sure that no lack of fusion existed, as shown in *Figure 6-15*a and *Figure 6-15*b.

Table 6-7: Overlap percentages, initial bead width, and distance for both stages 1 and 2 (3rd bead)

Stage 1	Overlap (%)	Initial Bead Width (mm)	Bead Distance (mm)
Voltage = 21 V	0	3.5	3.5
Current = 30 A	5	3.1	2.94
	10	3	2.7
	15	3.2	2.72
	20	3	2.4
	30	3.07	2.15
	50	3.27	1.64
Stage 2	0	2.25	2.25
Voltage = 21 V	5	2.43	2.31
Current = 24 V	10	2.37	2.13
For bead on plate:	15	2.37	2.01
- **Voltage = 21 V**	20	2.3	1.84
- **Current = 30 A**	25	2.36	1.65
- **Overlap = 15%**	30	2.4	1.68
	50	2.6	1.3

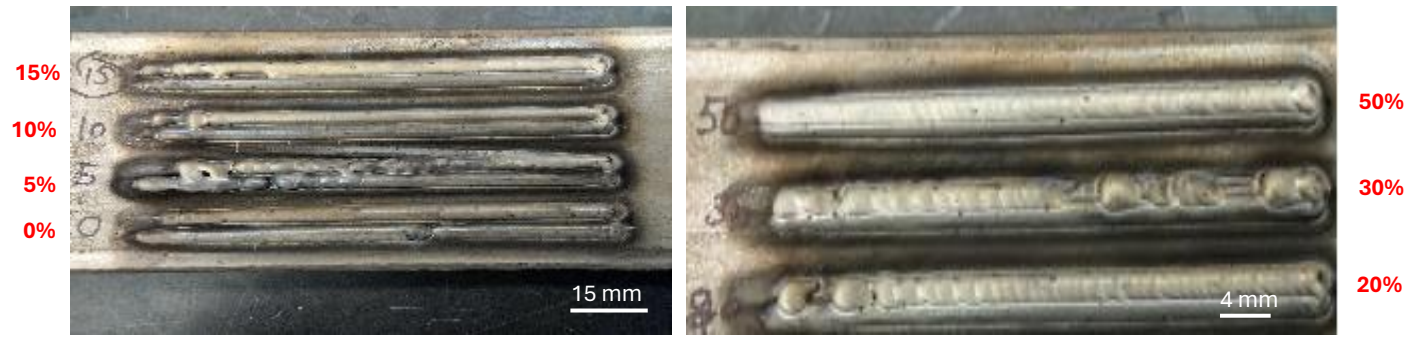

Figure 6-13: Stage 1 of overlap testing performed at percentages of 0, 5, 10, 15, 20, 30, and 50% for beads on plate overlaps

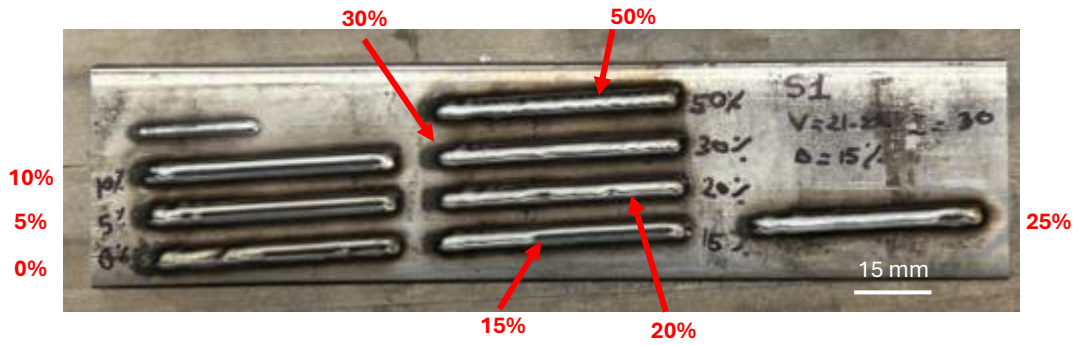

Figure 6-14: Stage 2 of overlap testing performed at percentages of 0, 5, 10, 15, 20, 30, and 50% for stacked beads

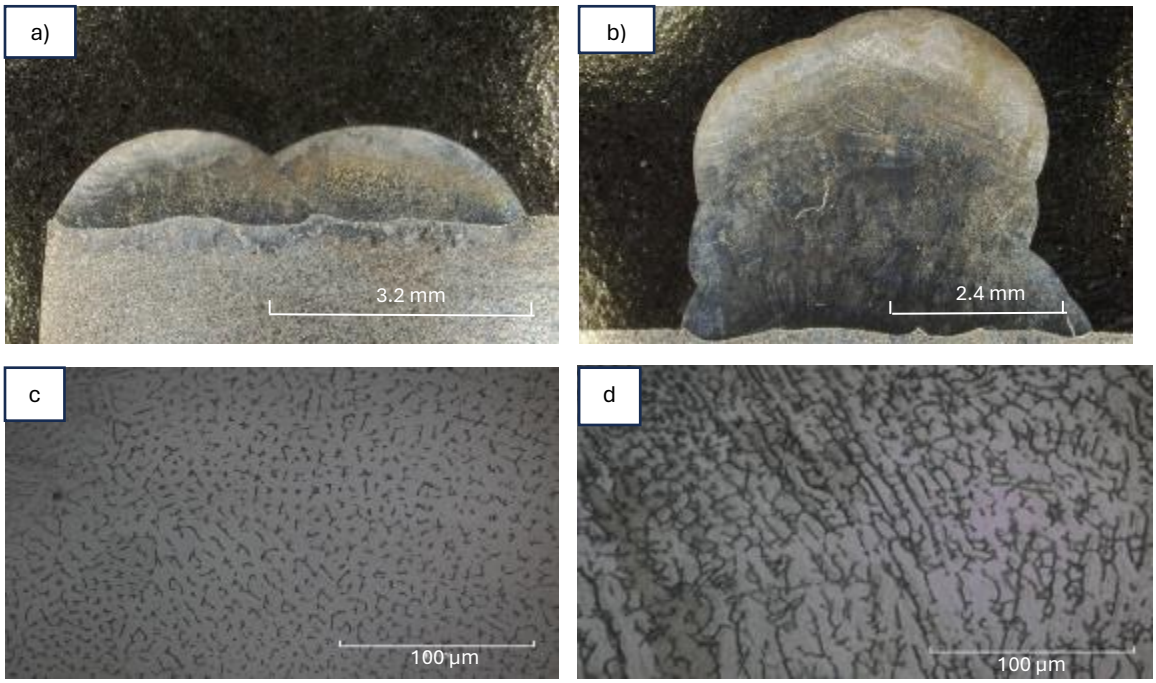

Figure 6-15: Macrostructures of a) 1st layer beads overlapped at 15% and b) third layer beads overlapped at 25%. Also shown are their microstructures at c) 15% and d) 25%

6.4 Automatic Voltage Control Performance

6.4.1 System Overview

The AVC system used relies on the voltage measurement of the electrode tip when welding. As the voltage telemetry or actual voltage varies, the arc gap varies since these parameters are directly proportional to each other in arc welding. The overview of the system is shown as a block diagram in *Figure 6-16*. As welding is initiated, the welding head moves to a certain distance from the melt pool

according to the desired voltage (voltage command). This is adjusted through the AVC that attempts to correct and maintain the arc gap by keeping the actual voltage (voltage telemetry) as close as possible to the desired voltage. Since the voltage is proportional to the arc gap, the AVC measures and adjusts the voltage telemetry through the detection of the surface of the bead and hence through the arc gap. It is also worth noting that the current is always constant throughout deposition. In that case, since arc gap is linearly correlated to the arc voltage, small variations within the power also exist based on the relation of power with voltage and current ($Power = Voltage \cdot Current$).

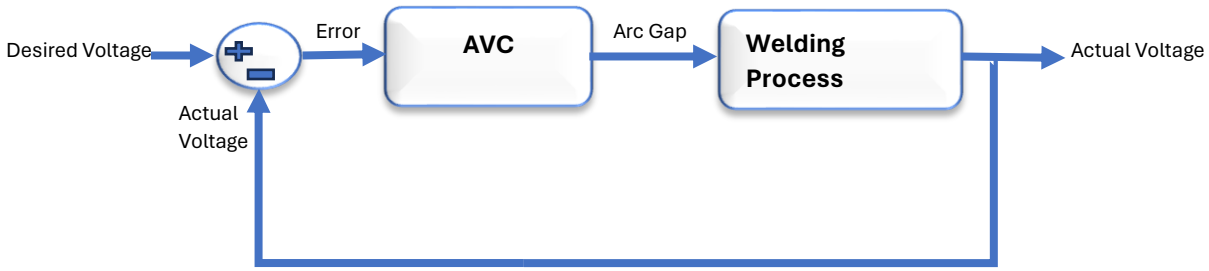

Figure 6-16: Block diagram representing AVC system

There are several parameters that may be used to improve the performance of the AVC, two of which are the gain and the max speed. The gain is the multiplication factor used in the motor loop. In this case, it corresponds to the proportional gain K_p, and usually an increase of the gain amplifies the corrective action, which leads to a faster response of the AVC. However, in the case of the AVC used on the LAWS system, changes in the gain leads to some unknown and unpredictable outcomes due to it being a complex parameter. The max speed determines how fast the AVC will adjust the voltage based on the arc gap. Both the max speed and gain were the parameters that were modified to test the performance of the AVC.

Two other parameters that were unused are the dead band and the distance per voltage ratio. The dead band corresponds to the voltage difference from the desired voltage at which the AVC will be activated. For example, for the performance testing of the AVC system, the dead band was set at 0.1 V

while the desired voltage was mainly set around 20.8 V. This would mean that should the actual voltage be between 20.7 and 20.9 V, then the AVC will be inactive and perform no corrective action.

6.4.2 Controller Feedback Gain Testing

Three different gains (0.8, 1.0, and 1.2) were used in the height feedback controller setting to deposit three welds. For each gain, the Z-position, measured bead height, and voltage (telemetry and command) were plotted versus time to analyze the change in Z-position with respect to the voltage. The bead height was measured from the layer surface to the plate using a caliper. However, due to the heat accumulation during the deposition, the plate underwent slight bending, leading to inaccurate measurements of layer height since the reference is the plate. This was accounted for when plotting the graphs.

Comparing *Figure 6-17, Figure 6-18,* and *Figure 6-19*, voltage telemetry seems to be following voltage command closely for all gain settings while the gain of 1.0 seems to have the steepest initial slope. This slope gives an indication into how quickly the AVC is able to adjust the voltage telemetry with the command, which also explains the increase in Z-position. Average errors between the voltage command and voltage telemetry are 0.0569, 0.0641, and 0.0534 V for gains of 1.0, 0.8, and 1.2, respectively. When comparing the Z-position with the corrected bead height, it can be seen that the former follows the latter very closely through the investigation of matching peaks for both corrected bead height and Z-position, as shown by the dashed lines in *Figure 6-17*. These peaks and hence, large changes in the height of the layer surface during deposition also interpret some larger than average fluctuations in voltage telemetry, particularly at these same dashed lines. The close correlation between the Z-position and bead height can also be seen in *Figure 6-20*, *Figure 6-21*, and *Figure 6-22*, which highlight the linear regression between them as well as the 95% confidence interval. The R-values were

found to be 0.90, 0.96, and 0.87 for gains of 0.8, 1.0, and 1.2 respectively indicating that the bead height was found to correlate most for a gain of 1.0.

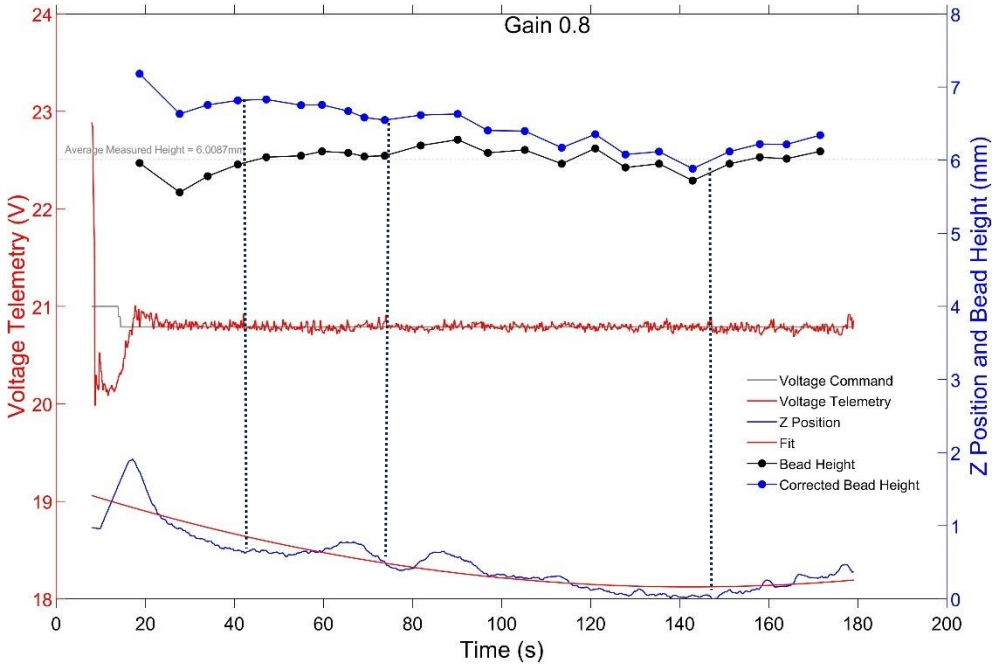

Figure 6-17: Z-position, bead height (measured and corrected), and voltage vs time for gain of 0.8

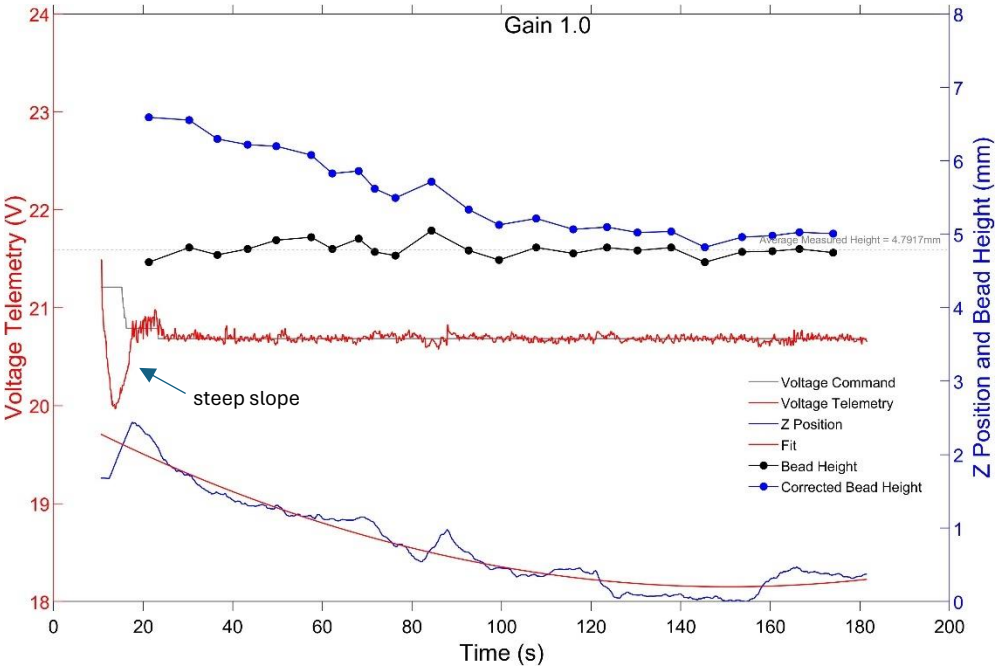

Figure 6-18: Z-position, bead height (measured and corrected), and voltage vs time for gain of 1.0

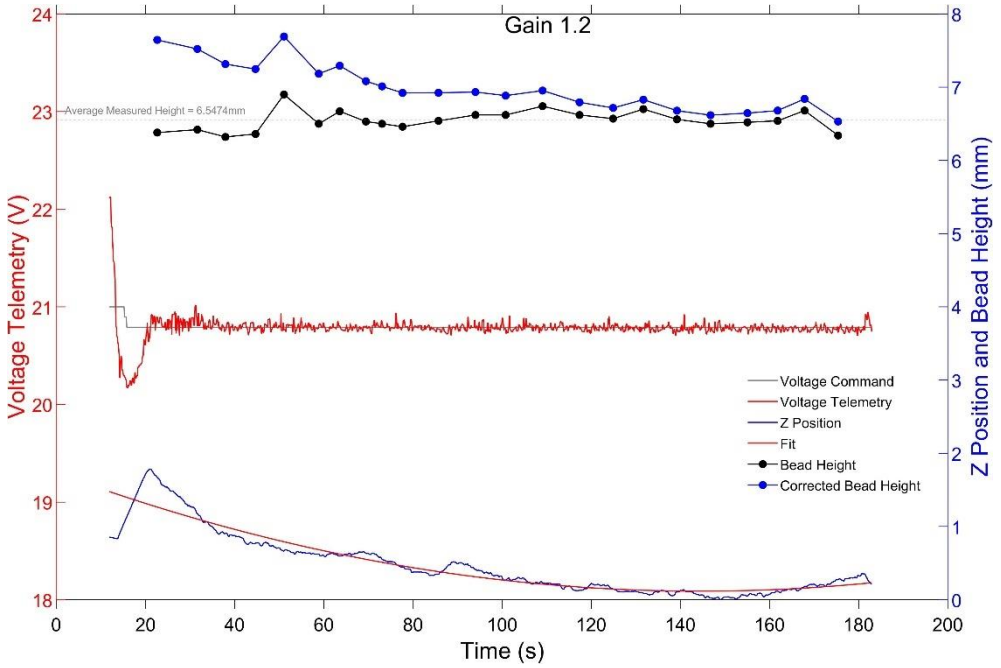

Figure 6-19: Z-position, bead height (measured and corrected), and voltage vs time for gain of 1.2

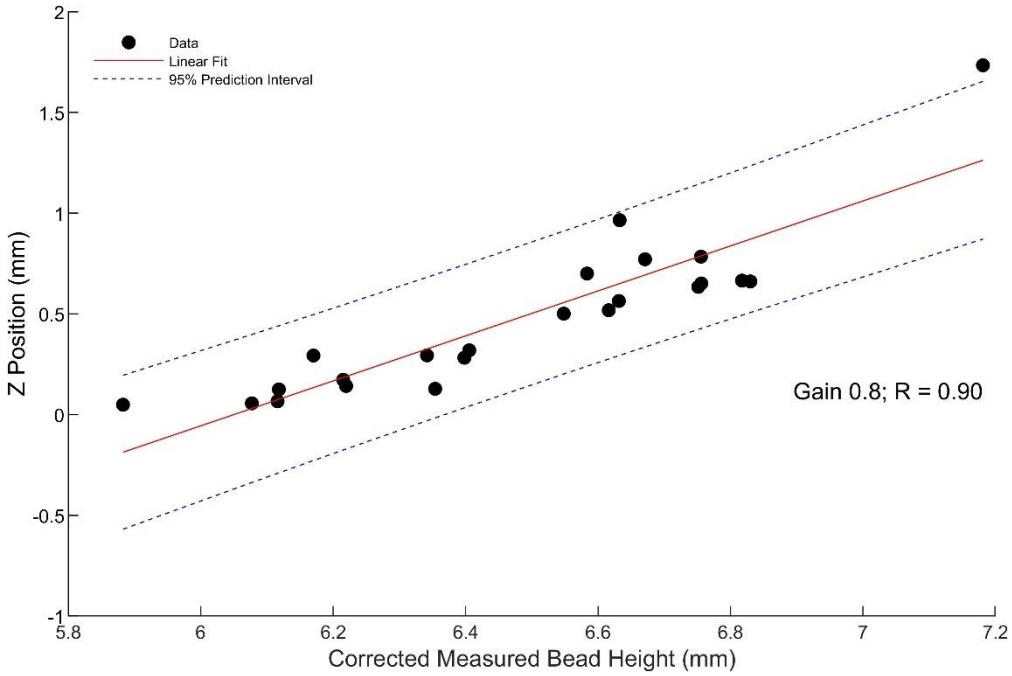

Figure 6-20: Z-position vs corrected measured bead height, showing the line of best fit with a correlation coefficient of 0.90 for a gain of 0.8

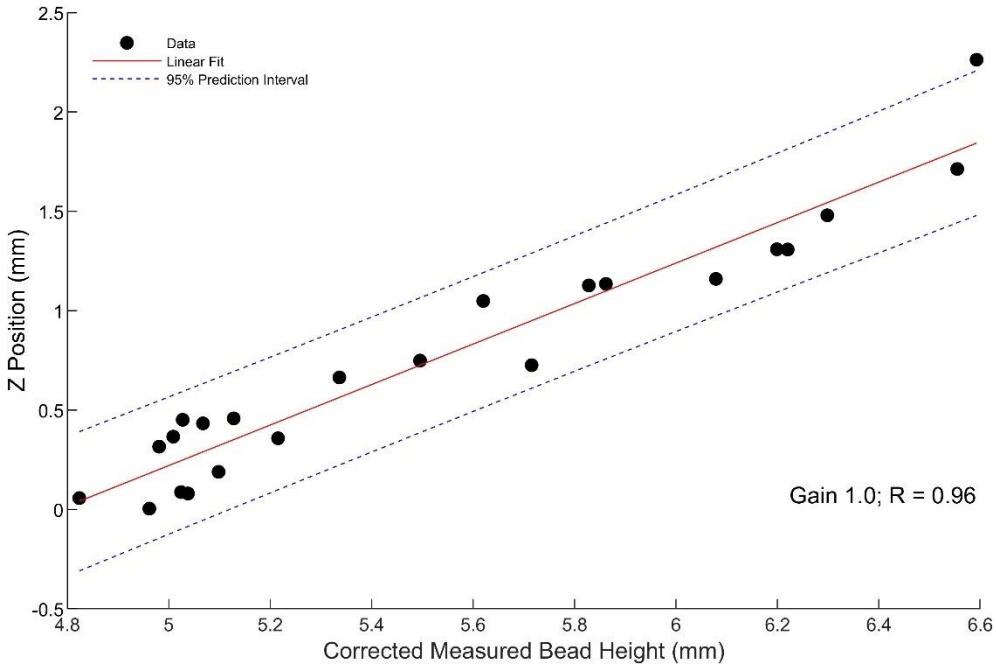

Figure 6-21: Z-position vs corrected measured bead height, showing the line of best fit with a correlation coefficient of 0.96 for a gain of 1.0

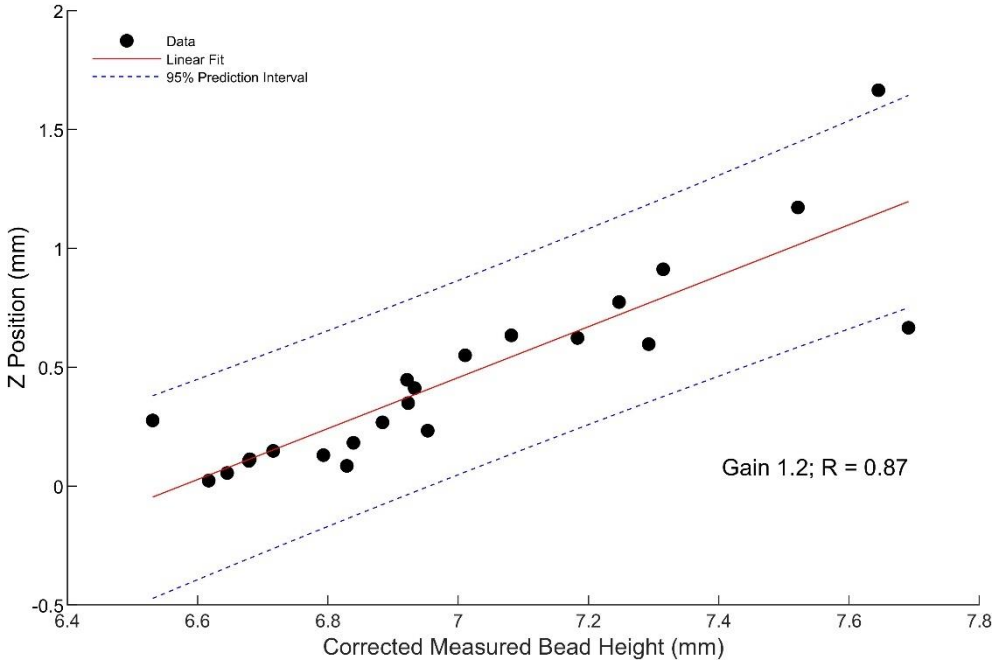

Figure 6-22: Z-position vs corrected measured bead height, showing the line of best fit with a correlation coefficient of 0.87 for a gain of 1.2

6.4.3 Max Speed Testing

Three different max speeds were chosen while maintaining a gain of 1.0 and similar to section 6.3.2, Z-position, bead height and voltage were plotted versus time for max speeds of 50, 65, and 35 mm/min. As expected, when comparing the voltage telemetry with the voltage command in *Figure 6-23, Figure 6-24, and Figure 6-25*, it can be seen that voltage telemetry follows voltage command the most when the max speed is set 65 mm/min, the latter which yields the steepest initial slope (*Figure 6-25*) followed by that at 50 mm/min and that at 35 mm/min. Average errors between voltage telemetry and voltage command are 0.1829, 0.0749, and 0.0534 V for max speeds of 50, 35, and 65 mm/min, respectively. The regression plots between the Z-position and the corrected bead height were also investigated in *Figure 6-26*, *Figure 6-27*, and *Figure 6-28*, revealing highest correlation for a max speed of 65 mm/min, followed by 50 mm/min, then 35 mm/min with R-values of 0.93, 0.95, and 0.995, respectively. This is explained by the faster response of the AVC when increasing the max speed, resulting in a much quicker correction of the Z-position when detecting different height deviations within the surface of the layer.

Overall observations were expected and highlight the higher consistency of the max speed parameter compared to the gain, which revealed ideal results at a value of 1.0. While the AVC may be a reliable control method for arc seam tracking, its purpose mainly falls under stabilizing the arc gap according to the voltage command chosen and is not made for layer height corrections. Hence, there is a need to look into alternative means to develop feedback control of the layer height.

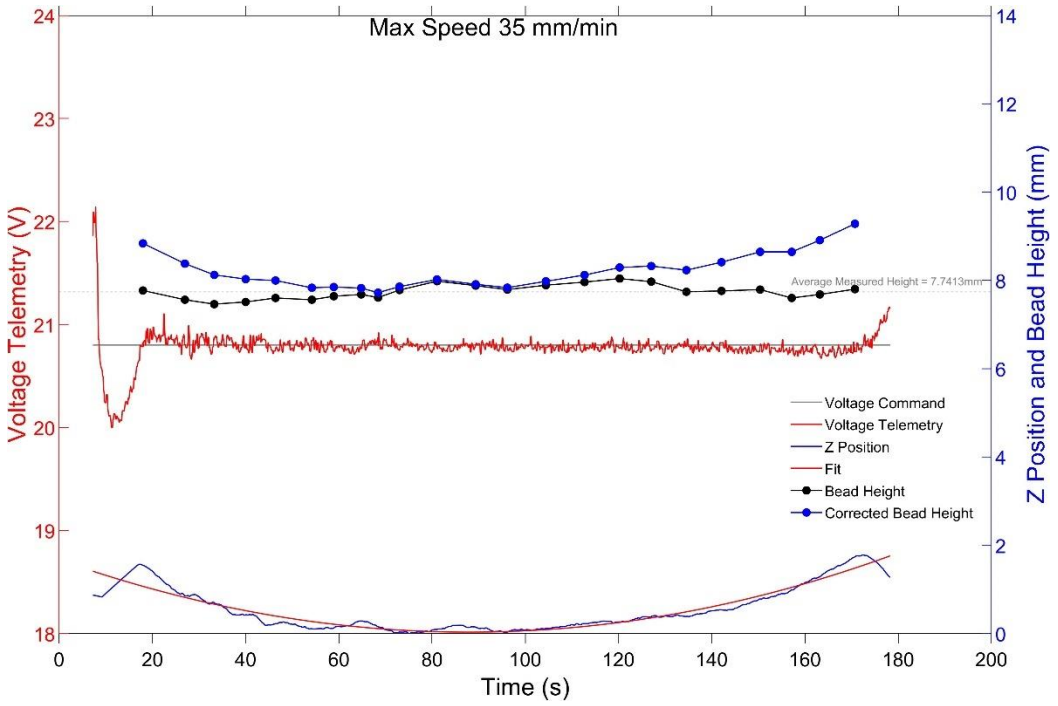

Figure 6-23: Z-position, bead height (measured and corrected), and voltage vs time for max speed of 35 mm/min

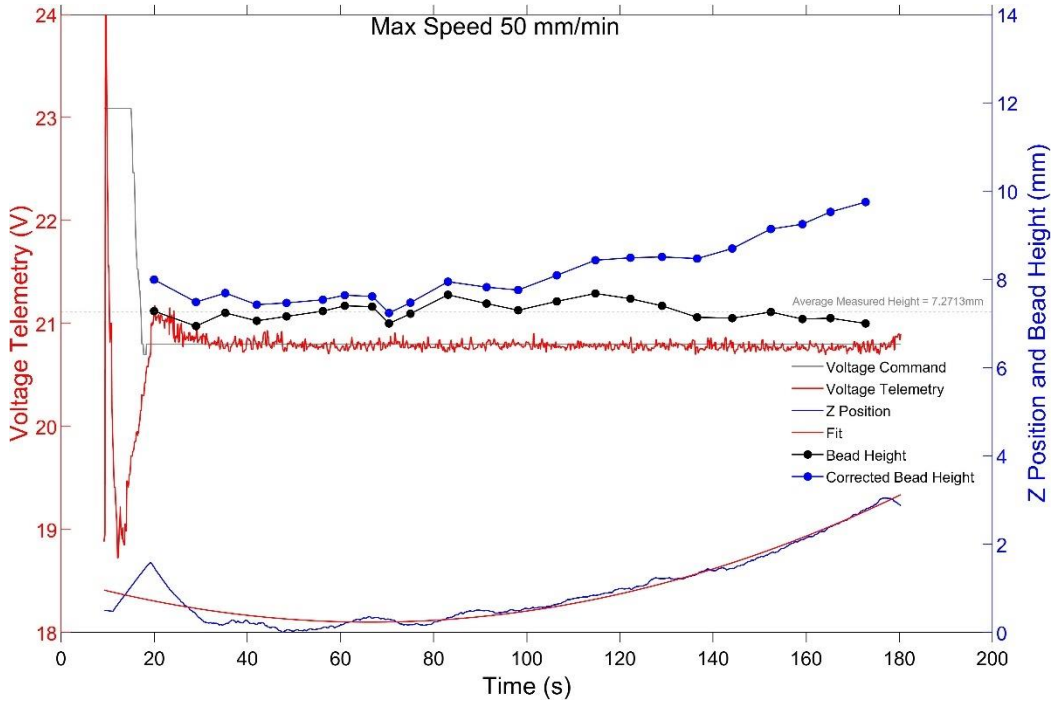

Figure 6-24: Z-position, bead height (measured and corrected), and voltage vs time for max speed of 50 mm/min

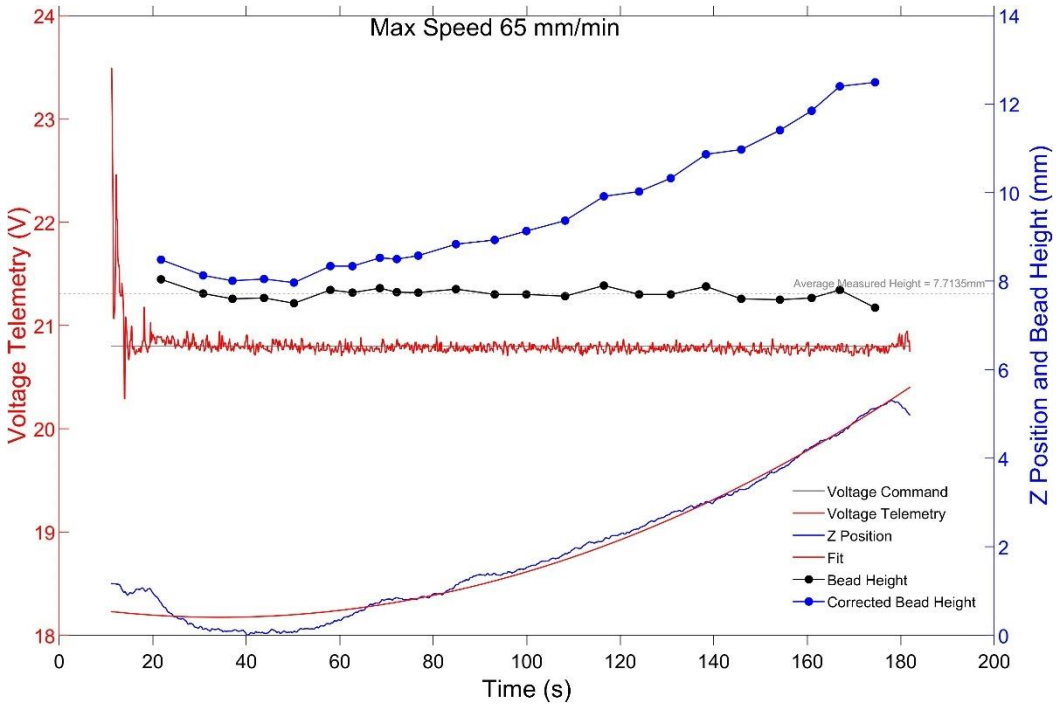

Figure 6-25: Z-position, bead height (measured and corrected), and voltage vs time for max speed of 65 mm/min

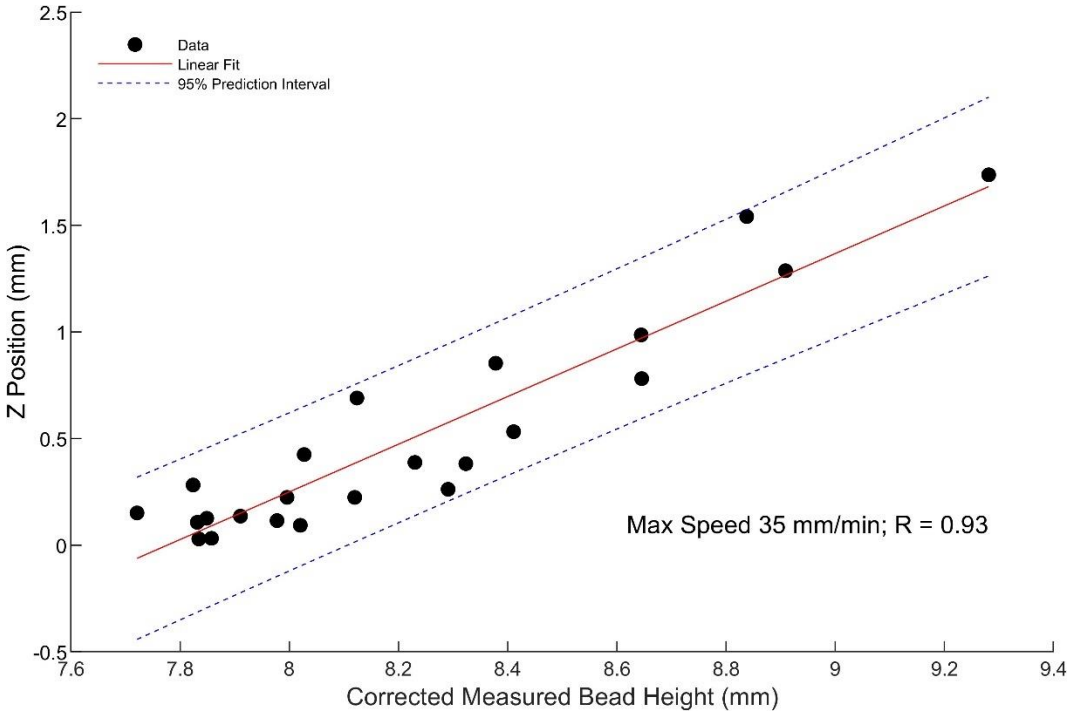

Figure 6-26: Z-position vs corrected measured bead height, showing the line of best fit with a correlation coefficient of 0.93 for a max speed of 35 mm/min

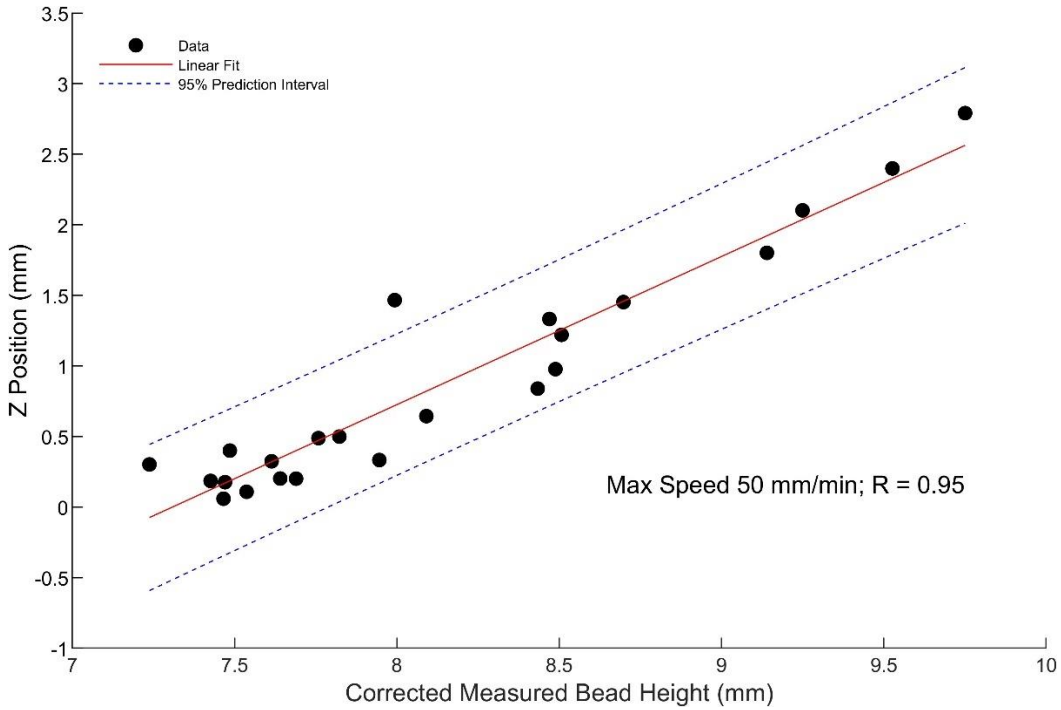

Figure 6-27: Z-position vs corrected measured bead height, showing the line of best fit with a correlation coefficient of 0.96 for a max speed of 50 mm/min

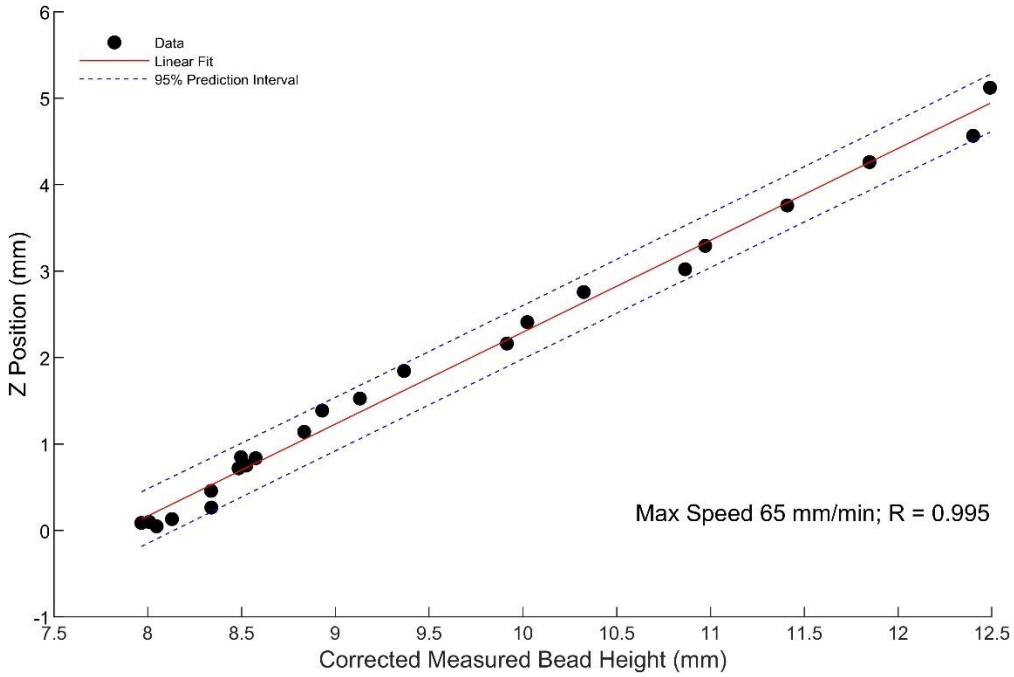

Figure 6-28: Z-position vs corrected measured bead height, showing the line of best fit with a correlation coefficient of 0.995 for a max speed of 65 mm/min

6.4.4 Response to Step Change

Assessing the performance of the AVC when introduced with a sudden step change in height difference during deposition is an important criterion for reliability. Deposition was performed on a layer that had a sudden 1 mm drop in layer height. The voltage and Z-position were monitored versus time for gains of 1.0, 0.8, and 1.2, as shown in *Figure 6-29*. It was found that the Z-position was quick to be modified by the AVC for all gains in response to sudden spike in voltage telemetry as a result of the 1 mm bump. This shows no particular difference in terms of AVC response to a step change irrespective of the gain chosen.

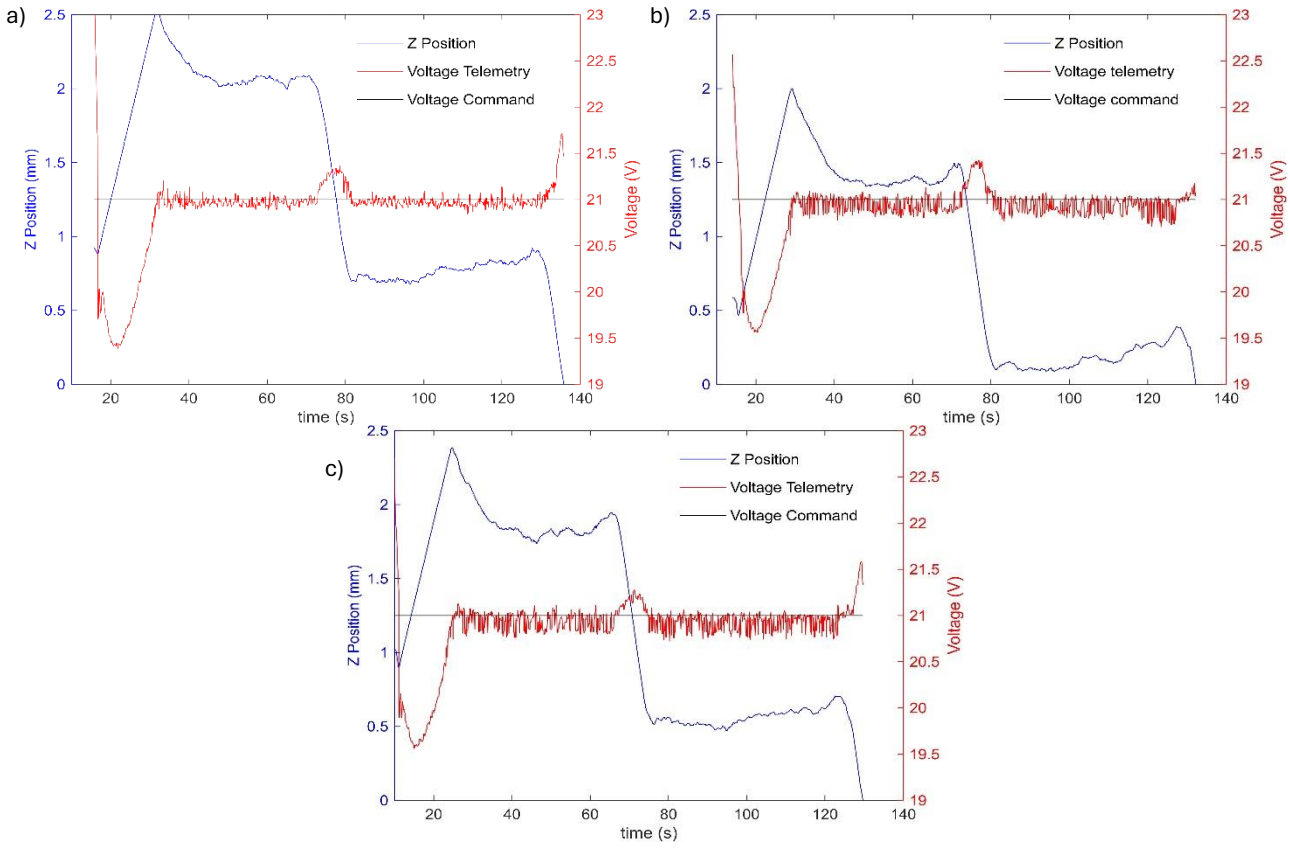

Figure 6-29: Voltage and Z position responses to 1 mm step change during deposition for a) G=0.8, b) G=1.0, and c) G=1.2

6.5 Summary

In summary, this chapter investigated the performance of the current AVC system as well as looking into obtaining accurate WFS ranges to properly correct layer height deviations. It also investigated optimal distances for bead overlap applications. In terms of investigating AVC performance, different gains and correction speeds were chosen to assess it. It was found that the voltage telemetry followed the voltage command closely for all parameters but had a faster response for a gain of 1.0 and max speed of 65 mm/min. Z-position closely followed bead height during deposition, particularly for these same parameters, which ultimately is the basis for maintaining arc voltage arc voltage. This shows the overall fast and reliable performance of the AVC when surface height deviations occur during deposition.

When attempting to correct layer height deviations, the modification of the WFS accordingly based on the volume of material added for different WFS ranges was found to accurately correct deviations with an error of no more than 0.03 mm.

Overlap parameters were found to be optimal at 15% for the initial layer and 25% for subsequent layers, which were determined based on best fusion and flat surface.

Chapter 7
Conclusion and Future Works

This chapter is a conclusion of all the work that has been presented in the thesis and highlights the key points in regard to the research done. It also looks into the future works that may be investigated based on the results of the current research.

7.1 Conclusion

This work has demonstrated the use of MPAW for fabricating slender wall structures by WAAM, with nearly uniform strength and no porosity. Although MPAW offers lower deposition rates than other processes, the lack of defects and uniform properties make it suitable for repair of metal parts, in which higher precision and low heat inputs are required. This work was divided into three chapters.

The first chapter investigated the effect of anisotropy for a 3D printed component using WAAM, in which cooling times to reach an interpass temperature of 150ºC were found to be around one minute as a result of the low heat input, making the process especially suitable for part repair applications where embrittled materials are used for example. The strength properties of the fabricated material exhibited nearly uniform yield strength properties of 318 to 326 MPa, and 526 to 564 MPa ultimate tensile strength values for the build and transverse directions respectively. Likewise, the hardness varied from 183 to 200 HV across different locations in the built plate. The uniformity in properties is desirable in repair applications as well. However, the stiffness of the material exhibited fairly anisotropic properties ranging from 79.5±6.8 GPa along the build direction to 105.2±20.7 GPa in the travel direction. This stiffness anisotropy was confirmed to be due to the strong preferred orientation of the <001> crystals during solidification along the build direction, which were observed by EBSD analysis and

quantitatively confirmed to have produced a lower stiffness value which correlated well with the observed measurement.

The presence of columnar grains in the WAAM process motivated the investigation of methods to eliminate these grains. Hence, the second chapter investigated the application of vibration during the deposition process and its effect on grain size for both stainless-steel and titanium samples. Different frequencies and amplitudes were investigated, and it was found that the vibration process initiated an increase in nucleation sites near the substrate, leading to a fragmentation of columnar grains during the solidification process and ultimately increasing the presence of equiaxed grains which are more refined. Amplitude was found to have no significant effect on the change in grain size near the substrate or near the top layer. This was not the case for different frequencies from 50 to 100 Hz, which were found to modify grain size around the substrate, particularly for stainless-steel.

Finally, despite the lower heat input of the MPAW process, layer height deviations were still present following WAAM deposition. This led to the investigation of the sensitivity of the AVC controller through analyzing two parameters, the gain, and the correction speed, leading to the conclusion that while the AVC provides reliable voltage control according to the desired voltage based on close following of the Z-position with the bead height. The chapter also investigated the manual correction of layer deviations through the accurate determination of the volume of material added for WFS of 100, 250, and 400 mm/min. These were used as a basis to calculate the necessary WFS according to different height deviations, revealing highly accurate correction with an error of 0.03 mm. Also, this chapter investigated the optimal bead overlap parameters for bead-on-plate and subsequent layers based on flat surface and best fusion. Overlap parameters were found to be optimal at 15% for the initial layer and 25% for subsequent layers.

7.2 Future Works

The present work performed may be extended for future research and future works may include:

- Building different more complex parts using the WAAM process by MPAW and investigating if the effect of anisotropy becomes more pronounced and if the mechanical properties become less uniform. Anisotropy would be expected to increase with more complex shapes.
- Building an additional wall using the WAAM process and performing fatigue tests to evaluate the fatigue life of the part.
- Utilizing the volumes of material added for WFS of 100, 250, and 400 mm/min as a basis when developing an improved control strategy to automatically correct layer height deviations.
- Utilizing the overlap percentages obtained for bead-on-plate and subsequent layers for additive component requirements.
- Performing additional tests for VWC in multi-layer MPAW using similar frequencies and amplitudes investigated and analyzing the mechanical properties and residual stresses induced, particularly comparing the difference in properties between top and bottom regions of the deposited material. Since equiaxed grains were noticed in the current work, properties are expected to improve as well.

Letters of Copyright Permission

Figs. 1-1 and 1-3

SPRINGER NATURE LICENSE
TERMS AND CONDITIONS

Apr 25, 2024

This Agreement between Mr. Rami Hakim ("You") and Springer Nature ("Springer Nature") consists of your license details and the terms and conditions provided by Springer Nature and Copyright Clearance Center.

License Number	5724410023000
License date	Feb 08, 2024
Licensed Content Publisher	Springer Nature
Licensed Content Publication	The International Journal of Advanced Manufacturing Technology
Licensed Content Title	Wire and arc additive manufacturing of metal components: a review of recent research developments
Licensed Content Author	Jienan Liu et al
Licensed Content Date	Sep 24, 2020
Type of Use	Thesis/Dissertation

Requestor type	academic/university or research institute
Format	electronic
Portion	figures/tables/illustrations
Number of figures/tables/illustrations	2
Will you be translating?	no
Circulation/distribution	500 - 999
Author of this Springer Nature content	no
Title of new work	Parameter Investigation and Properties for WAAM builds using MPAW
Institution name	University of Waterloo
Expected presentation date	Apr 2024
Portions	Figures 2 and 3 Mr. Rami Hakim
Requestor Location	Waterloo, ON Canada Attn: University of Waterloo
Total	0.00 CAD

Fig. 1-2

ELSEVIER LICENSE
TERMS AND CONDITIONS

Apr 26, 2024

This Agreement between Mr. Rami Hakim ("You") and Elsevier ("Elsevier") consists of your license details and the terms and conditions provided by Elsevier and Copyright Clearance Center.

License Number	5776611013214
License date	Apr 26, 2024
Licensed Content Publisher	Elsevier
Licensed Content Publication	Materials Today: Proceedings
Licensed Content Title	Wire arc additive manufacturing of aluminium alloys: A review
Licensed Content Author	K.E.K. Vimal,M. Naveen Srinivas,Sonu Rajak
Licensed Content Date	Jan 1, 2021
Licensed Content Volume	41

Licensed Content Issue	n/a
Licensed Content Pages	7
Start Page	1139
End Page	1145
Type of Use	reuse in a thesis/dissertation
Portion	figures/tables/illustrations
Number of figures/tables/illustrations	1
Format	electronic
Are you the author of this Elsevier article?	No
Will you be translating?	No
Title of new work	Parameter Investigation and Properties for WAAM builds using MPAW
Institution name	University of Waterloo
Expected presentation date	Apr 2024
Portions	Figure 1
	Mr. Rami Hakim
Requestor Location	Waterloo, ON Canada Attn: University of Waterloo
Publisher Tax ID	GB 494 6272 12
Total	0.00 CAD

Figs. 2-1 and 2-2

ELSEVIER LICENSE
TERMS AND CONDITIONS

Apr 25, 2024

This Agreement between Mr. Rami Hakim ("You") and Elsevier ("Elsevier") consists of your license details and the terms and conditions provided by Elsevier and Copyright Clearance Center.

License Number	5724390791252
License date	Feb 08, 2024
Licensed Content Publisher	Elsevier
Licensed Content Publication	Journal of Manufacturing Processes
Licensed Content Title	Plasma arc welding: Process, sensing, control and modeling
Licensed Content Author	C.S. Wu,L. Wang,W.J. Ren,X.Y. Zhang
Licensed Content Date	Jan 1, 2014
Licensed Content Volume	16

Licensed Content Issue	1
Licensed Content Pages	12
Start Page	74
End Page	85
Type of Use	reuse in a thesis/dissertation
Portion	figures/tables/illustrations
Number of figures/tables/illustrations	2
Format	electronic
Are you the author of this Elsevier article?	No
Will you be translating?	No
Title of new work	Parameter Investigation and Properties for WAAM using MPAW
Institution name	University of Waterloo
Expected presentation date	Apr 2024
Portions	Figures 1 and 3
Requestor Location	Mr. Rami Hakim Waterloo, ON Canada Attn: University of Waterloo
Publisher Tax ID	GB 494 6272 12
Total	0.00 CAD

Fig. 2-6

ELSEVIER LICENSE
TERMS AND CONDITIONS

Apr 25, 2024

This Agreement between Mr. Rami Hakim ("You") and Elsevier ("Elsevier") consists of your license details and the terms and conditions provided by Elsevier and Copyright Clearance Center.

License Number	5724400167717
License date	Feb 08, 2024
Licensed Content Publisher	Elsevier
Licensed Content Publication	Journal of Manufacturing Processes
Licensed Content Title	A review of the wire arc additive manufacturing of metals: properties, defects and quality improvement
Licensed Content Author	Bintao Wu,Zengxi Pan,Donghong Ding,Dominic Cuiuri,Huijun Li,Jing Xu,John Norrish
Licensed Content Date	Oct 1, 2018
Licensed Content Pages	13

Start Page	127
End Page	139
Type of Use	reuse in a thesis/dissertation
Portion	figures/tables/illustrations
Number of figures/tables/illustrations	1
Format	electronic
Are you the author of this Elsevier article?	No
Will you be translating?	No
Portions	Figure 6
Requestor Location	Mr. Rami Hakim Waterloo, ON Canada Attn: University of Waterloo
Publisher Tax ID	GB 494 6272 12
Total	0.00 USD

Figs. 2-7 and 2-8

ELSEVIER LICENSE
TERMS AND CONDITIONS

Apr 25, 2024

This Agreement between Mr. Rami Hakim ("You") and Elsevier ("Elsevier") consists of your license details and the terms and conditions provided by Elsevier and Copyright Clearance Center.

License Number	5776110210147
License date	Apr 25, 2024
Licensed Content Publisher	Elsevier
Licensed Content Publication	Journal of Manufacturing Processes
Licensed Content Title	Potentials and strategies of solid-state additive friction-stir manufacturing technology: A critical review
Licensed Content Author	F. Khodabakhshi,A.P. Gerlich
Licensed Content Date	Dec 1, 2018
Licensed Content Volume	36

Licensed Content Issue	n/a
Licensed Content Pages	16
Start Page	77
End Page	92
Type of Use	reuse in a thesis/dissertation
Portion	figures/tables/illustrations
Number of figures/tables/illustrations	2
Format	electronic
Are you the author of this Elsevier article?	No
Will you be translating?	No
Title of new work	Parameter Investigation and Properties for WAAM builds using MPAW
Institution name	University of Waterloo
Expected presentation date	Apr 2024
Portions	Figures 12 and 13
Requestor Location	Mr. Rami Hakim Waterloo, ON Canada Attn: University of Waterloo
Publisher Tax ID	GB 494 6272 12
Total	0.00 CAD

Fig. 2-9

ELSEVIER LICENSE
TERMS AND CONDITIONS

Apr 25, 2024

This Agreement between Mr. Rami Hakim ("You") and Elsevier ("Elsevier") consists of your license details and the terms and conditions provided by Elsevier and Copyright Clearance Center.

License Number	5776110617489
License date	Apr 25, 2024
Licensed Content Publisher	Elsevier
Licensed Content Publication	Materials Science and Engineering: A
Licensed Content Title	Correlation between arc mode, microstructure, and mechanical properties during wire arc additive manufacturing of 316L stainless steel
Licensed Content Author	Leilei Wang,Jiaxiang Xue,Qiang Wang
Licensed Content Date	Mar 28, 2019
Licensed Content Volume	751

Licensed Content Issue	n/a
Licensed Content Pages	8
Start Page	183
End Page	190
Type of Use	reuse in a thesis/dissertation
Portion	figures/tables/illustrations
Number of figures/tables/illustrations	1
Format	electronic
Are you the author of this Elsevier article?	No
Will you be translating?	No
Title of new work	Parameter Investigation and Properties for WAAM builds using MPAW
Institution name	University of Waterloo
Expected presentation date	Apr 2024
Portions	Figure 9
Requestor Location	Mr. Rami Hakim Waterloo, ON Canada Attn: University of Waterloo
Publisher Tax ID	GB 494 6272 12
Total	0.00 CAD

Fig. 2-10

ELSEVIER LICENSE
TERMS AND CONDITIONS

Apr 25, 2024

This Agreement between Mr. Rami Hakim ("You") and Elsevier ("Elsevier") consists of your license details and the terms and conditions provided by Elsevier and Copyright Clearance Center.

License Number	5776110951725
License date	Apr 25, 2024
Licensed Content Publisher	Elsevier
Licensed Content Publication	Additive Manufacturing
Licensed Content Title	Effect of heat treatments on 316 stainless steel parts fabricated by wire and arc additive manufacturing : Microstructure and synchrotron X-ray diffraction analysis
Licensed Content Author	Tiago A. Rodrigues,J.D. Escobar,Jiajia Shen,Valdemar R. Duarte,G.G. Ribamar,Julian A. Avila,Emad Maawad,Norbert Schell,Telmo G. Santos,J.P. Oliveira
Licensed Content Date	Dec 1, 2021

Licensed Content Volume	48
Licensed Content Issue	n/a
Licensed Content Pages	1
Start Page	102428
End Page	0
Type of Use	reuse in a thesis/dissertation
Portion	figures/tables/illustrations
Number of figures/tables/illustrations	1
Format	electronic
Are you the author of this Elsevier article?	No
Will you be translating?	No
Title of new work	Parameter Investigation and Properties for WAAM builds using MPAW
Institution name	University of Waterloo
Expected presentation date	Apr 2024
Portions	Figure 4
	Mr. Rami Hakim
Requestor Location	Waterloo, ON Canada Attn: University of Waterloo
Publisher Tax ID	GB 494 6272 12
Total	0.00 CAD

Figs. 2-16 and 2-17

ELSEVIER LICENSE
TERMS AND CONDITIONS

Apr 25, 2024

This Agreement between Mr. Rami Hakim ("You") and Elsevier ("Elsevier") consists of your license details and the terms and conditions provided by Elsevier and Copyright Clearance Center.

License Number	5724400607932
License date	Feb 08, 2024
Licensed Content Publisher	Elsevier
Licensed Content Publication	Materials Science and Engineering: A
Licensed Content Title	The effect of harmonic vibration with a frequency below the resonant range on the mechanical properties of AA-5083-H321 aluminum alloy GMAW welded parts
Licensed Content Author	Reza Tamasgavabari,Ali Reza Ebrahimi,Seyed Mehdi Abbasi,Ali Reza Yazdipour
Licensed Content Date	Oct 24, 2018

Licensed Content Volume	736
Licensed Content Issue	n/a
Licensed Content Pages	10
Start Page	248
End Page	257
Type of Use	reuse in a thesis/dissertation
Portion	figures/tables/illustrations
Number of figures/tables/illustrations	2
Format	electronic
Are you the author of this Elsevier article?	No
Will you be translating?	No
Title of new work	Parameter Investigation and Properties for WAAM builds using MPAW
Institution name	University of Waterloo
Expected presentation date	Apr 2024
Portions	Figures 6 and 9
Requestor Location	Mr. Rami Hakim Waterloo, ON Canada Attn: University of Waterloo
Publisher Tax ID	GB 494 6272 12
Total	0.00 CAD

Chapter 4 Rights

Feb 24, 2024

This Agreement between Mr. Rami Hakim ("You") and Springer Nature ("Springer Nature") consists of your license details and the terms and conditions provided by Springer Nature and Copyright Clearance Center.

License Number	5735640504330
License date	Feb 24, 2024
Licensed Content Publisher	Springer Nature
Licensed Content Publication	Welding in the World
Licensed Content Title	Mechanical anisotropy and microstructural characterization of AISI 316LSi stainless steel using micro-plasma directed energy deposition
Licensed Content Author	R. Hakim et al
Licensed Content Date	Dec 26, 2023
Type of Use	Thesis/Dissertation
Requestor type	academic/university or research institute
Format	electronic
Portion	full article/chapter
Will you be translating?	no

Circulation/distribution	1 - 29
Author of this Springer Nature content	yes
Title of new work	Parameter Investigation and Properties for WAAM builds using MPAW
Institution name	University of Waterloo
Expected presentation date	Apr 2024
Order reference number	R2023
Requestor Location	Mr. Rami Hakim Waterloo, ON Canada Attn: University of Waterloo
Total	0.00 CAD

Bibliography

[1] F. Wilkinson, "Industrialization, labor, and life," National Geographic Society, 15 February 2023. [Online]. Available: https://education.nationalgeographic.org/resource/industrialization-labor-and-life.

[2] K. Shwab, "The Fourth Industrial Revolution: what it means, how to respond," World Economic Forum, 14 January 2016. [Online]. Available: https://www.weforum.org/agenda/2016/01/the-fourth-industrial-revolution-what-it-means-and-how-to-respond/.

[3] Arun, "10 major inventions of the industrial revolution," Learnodo Newtonic, 8 September 2022. [Online]. Available: https://learnodo-newtonic.com/industrial-revolution-inventions.

[4] "The 4 Industrial Revolutions," institute of Entrepreneurship Development, 30 June 2019. [Online]. Available: https://ied.eu/project-updates/the-4-industrial-revolutions/.

[5] V. May, "The History of Additive Mnaufacturing: From The 1980s to Today," Prototal UK, 7 October 2022. [Online]. Available: https://prototaluk.com/blog/history-of-additive-manufacturing/#:~:text=Additive%20Manufacturing%20in%20the%201980s,to%20light%20to%20create%20prototypes..

[6] B. Wu, Z. Pan, D. Ding, D. Cuiuri, H. Li, J. Xu and J. Norrish, "A review of the wire arc additive manufacturing of metals: properties, defects and quality improvement," *Journal of Manufacturing Processes 35,* pp. 127-139, 2018.

[7] D. S. Thomas and S. W. Gilbert, "Costs and Cost Effectiveness of Additive Manufacturing," *National Institute of Standards and Technology,* vol. 1176, 2014.

[8] I. Gibson, D. Rosen, B. Stucker and M. Khorasani, "Generalized Additive Manufacturing Process Chain," in *Additive Manufacturing Technologies*, Springer, 2020, pp. 53-75.

[9] E. Peterson, "Recent Innovations in Additive Manufacturing for Marine Vessels," *Maritime Technology and Research,* vol. 4, no. 4, 2022.

[10] S. C. Altiparmak and B. Xiao, "A market assessment of additive manufacturing potential for the aerospace industry," *Journal of Manufacturing Processes,* vol. 68, pp. 728-739, 2021.

[11] J. Liu, Y. Xu, Y. Ge, Z. Hou and S. Chen, "Wire and arc additive manufacturing of metal components: a review of recent research developments," *The International Journal of Advanced Manufacturing Technology 111,* pp. 149-198, 2020.

[12] K. E. Vimal, M. N. Srinivas and S. Rajak, "Wire arc additive manufacturing of aluminum alloys: A review," *materialstoday: Proceedings,* vol. 41, pp. 1139-1145, 2021.

[13] "Plasma Science and Fusion Center," Massachussets Institute of Technology, 2023. [Online]. Available: https://www.psfc.mit.edu/vision/what_is_plasma.

[14] C. S. Wu, L. Wang, W. J. Ren and X. Y. Zhang, "Plasma arc welding: Process, sensing, control, and modeling," *Journal of Manufacturing Processes 16,* pp. 74-85, 2014.

[15] S. Kou, Welding Metallurgy, Wiley, 1987.

[16] "Variables that affect weld penetration," Lincoln Electric, [Online]. Available: https://www.lincolnelectric.com/en/welding-and-cutting-resource-center/process-and-theory/variables-that-affect-weld-penetration.

[17] PWSBLOG, "The Effects of Hydrogen Gas on Plasma Welding," Process Welding Systems Inc., 1 October 2017. [Online]. Available: https://processwelding.com/blog/2017/10/01/the-effects-of-hydrogen-gas-on-plasma-welding/.

[18] J. K. Martikainen and J. T. I. Moisio, "Investigation of the Effect of Welding Parameters on Weld Quality of Plasma Arc Keyhole Welding of Structural Steels," *Welding Research Supplement,* pp. 329-340, 1993.

[19] "DCEN and DCEP similarities," Welding Info, [Online]. Available: https://www.weldinginfo.org/welding-technology/dcen-and-dcep-polarities/.

[20] R. Sarrafi and R. Kovacevic, "Cathodic Cleaning of Oxides from Aluminum Surface by Variable-Polarity Arc," *Supplement to the Welding Journal,* vol. 89, pp. 1-10, 2010.

[21] Y. Li, C. Su and J. Zhu, "Comprehensive review of wire arc additive manufacturing: Hardware system, physical process, monitoring, property characterization, application, and future prospects," *Results in Engineering,* vol. 13, no. https://doi.org/10.1016/j.rineng.2021.100330, 2022.

[22] D. Ding, Z. Pan, D. Cuiuri and H. Li, "Wire-feed additive manufacturing of metal components: technologies, developments, and future interests," *International Journal of Advanced Manufacturing Technology 81,* pp. 465-481, 2015.

[23] F. Khodabakhshi and A. P. Gerlich, "Potentials and strategies of solid-state additive friction-stir manufacturing: A review," *Journal of Manufacturing Processes,* vol. 36, pp. 77-92, 2018.

[24] Z. Brytan, W. Borek and T. Tanski, "Introductory chapter: Why austenitic stainless steels are continuously interesting for science?," in *Austenitic Stainless Steels - New Aspects*, IntechOpen, 2017.

[25] L. P. Belotti, J. A. W. van Dommelen, M. G. D. Geers, C. Goulas, W. Ya and J. P. M. Hoefnagels, "Microstructural characterisation of thick-walled wire arc additively manufactured stainless steel," *Journal of Materials Processing Tech.,* 2022.

[26] X. Chen, J. Li, X. Cheng, B. He, H. Wang and Z. Huang, "Microstructure and mechanical properties of the austenitic stainless steel 316L fabricated by gas metal arc welding," *Materials Science & Engineering A 703,* pp. 567-577, 2017.

[27] L. Wang, J. Xue and Q. Wang, "Correlation between arc mode, microstructure, and mechanical properties during wire arc additive manufacturing of 316L stainless steel," *Materials Science and Engineering A,* vol. 751, pp. 183-190, 2019.

[28] C. R. Cunnigham, J. Wang, V. Dhokia, A. Shrokani and S. T. Newman, "Characterization of Austenitic 316LSi Stainless Steel Produced by Wire Arc Additive Manufacturing with Interlayer Cooling," in *International Solid Freeform Fabrication Symposium - An Additive Manufacturing Conference Proceedings*, Austin, 2019.

[29] T. A. Rodrigues, J. D. Escobar, J. Shen, V. R. Duarte, G. G. Ribamar, J. A. Avila, E. Maawad, N. Schell, T. G. Santos and J. P. Oliveira, "Effect of heat treatments on 316 stainless steel parts fabricated by wire and arc additive manufacturing: Microstructure and synchrotron X-ray diffraction analysis," *Journal of Additive Manufacturing,* vol. 48, no. 102428, 2021.

[30] T. A. Rodrigues, J. D. Escobar, J. Shen, V. R. Duarte, G. G. Ribamar, J. A. Avila, E. Maawad, N. Schell, T. G. Santos and J. P. Oliveira, "Effect of heat treatments on 316 stainless steel parts fabricated by wire and arc additive manufacturing: Microstructure and synchrotron X-ray diffraction analysis," *Journal of Additive Manufacturing,* vol. 48, no. 102428, 2021.

[31] C. Wang, T. G. Liu, P. Zhu, Y. H. Lu and T. Shoji, "Study on microstructure and tensile properties of 316L stainless steel fabricated by CMT wire and arc additive manufacturing," *Materials Science & Engineering A,* 2020.

[32] P. Wang, M. L. S. Nai, X. Tan, W. J. Sin, S. B. Tor and J. Wei, "Anisotropic Mechanical Properties in a Big-Sized Ti-6Al-4V Plate Fabricated by Electron Beam Melting," in *TMS2016 Annual Meeting Supplemental Proceedings*, 2016.

[33] B. E. Carroll, A. T. Palmer and A. M. Beese, "Anisotropic tensile behavior of Ti-6Al-4V components fabricated with directed energy deposition additive manufacturing," *Acta Materialia,* vol. 87, pp. 309-320, 2015.

[34] P. Wang, M. L. S. Nai, X. Tan, W. J. Sin, S. B. Tor and J. Wei, "Anisotropic Mechanical Properties in a Big-Sized Ti-6Al-4V Plate Fabricated by Electron Beam Melting," in *TMS2016 Annual Meeting Supplemental Proceedings*, 2016.

[35] F. Ji, Z. Hu, X. Qin, F. Yin, M. Ni and X. Xiong, "Grain refinement and mechanism of steel in ultrasound assisted wire arc additive manufacturing," *International Communications in Heat and Mass Transfer,* vol. 143, no. 106724, 2023.

[36] J. Tao and P. Levick, "Assessment of Feedback Variables for Through the Arc Seam Tracking in Robotic Gas Metal Arc Welding," in *International Conference on Robotics and Automation*, Detroit, MI, 1999.

[37] "Selecting the right seam tracking solution," Bancroft, 2024. [Online]. Available: https://bancrofteng.com/selecting-right-seam-tracking-solution/.

[38] "Intelligent Robotic Arc Sensing," Lincoln Electric, [Online]. Available: https://www.lincolnelectric.com/en/welding-and-cutting-resource-center/process-and-theory/intelligent-robotic-arc-sensing.

[39] T. Lehmann, D. Rose, E. Ranjbar, M. Ghasri-Khouzani, M. Tavakoli, H. Henein, T. Wolfe and A. Jawad Qureshi, "Large-scale metal additive manufacturing: A Holistic Review of the state of the art and Challenges," *International Materials Reviews,* vol. 67, no. 4, pp. 410-459.

[40] S. Takushima, D. Morita, N. Shinohara, H. Kawano, Y. Mizutani and Y. Takaya, "Optical in-process height measurement system for process control of laser metal-wire deposition," *Precision Engineering,* vol. 62, pp. 23-29, 2020.

[41] H. Shen, T. Lin, S. Chen and L. Li, "Real-Time Seam Tracking Technology of Welding Robot with Visual Sensing," *Journal of Intelligent Robot Systems,* vol. 59, pp. 283-298, 2010.

[42] J. Xiong, Y. Zhang and Y. Pi, "Control of deposition height in WAAM using visual inspection of previous and current layers," *Journal of Intelligent Manufacturing,* vol. 32, no. 8, pp. 2209-2217, 2021.

[43] Y. Yokomizu, T. Matsumura, R. Henmi and Y. Kito, "Total voltage drops in electrode fall regions of SF6, argon and air arcs in current range from 10 to 20 000 A," *Journal of Physics D: Applied Physics,* vol. 29, pp. 1260-1267, 1996.

[44] C. McIntosh and P. Mendez, "Experimental Measurements of Fall Voltages in Gas Metal Arc Welding," *Welding Research,* vol. 96, pp. 121-132, 2017.

[45] P. Koseyaporn, G. E. Cook and A. M. Strauss, "Adaptive Voltage Control in Fusion Arc Welding," *IEEE Transactions on Industry Applications,* vol. 36, no. 5, 2000.

[46] J. B. Bjorgvinsson, "Adaptive voltage control in gas tungsten arc welding," MS Thesis, Vanderbilt University, Nashville, TN, 1992.

[47] B. Jaescke, "Description of AVC/seam tracking for TIG welding," Lorch, Auenwald, Germany, 2015.

[48] C. Xia, Z. Pan, J. Polden, H. Li, Y. Xu, S. Chen and Y. Zhang, "A review on wire arc additive manufacturing: monitoring, control and a framework of automated system," *Journal of Manufacturing Systems,* vol. 57, pp. 31-45, 2020.

[49] A. Heralic, A.-K. Christiansson, M. Ottoson and B. Lennartson, "Increased stability in laser metal wire deposition through feedback from optical measurements," *Optics and Lasers in Engineering 48,* pp. 478-485, 2010.

[50] J. Xiong and G. Zhang, "Adaptive control of deposited height in GMAW-based layer additive manufacturing," *Journal of Materials Processing Technology 214,* pp. 962-968, 2014.

[51] A. Scetinec, D. Klobcar and D. Bracun, "In-process path replanning and online layer height control through deposition arc current for gas metal arc based additive manufacturing," *Journal of Manufacturing Processes,* vol. 64, no. https://doi.org/10.1016/j.jmapro.2021.02.038 , pp. 1169-1179, 2021.

[52] N. Li, D. Fan, J. Huang, S. Yu, W. Yuan and M. Han, "Self-Adaptive Control System for Additive Manufacturing Using Double Electrode Micro Plasma Arc Welding," *Chinese Journal of Mechanical Engineering,* pp. 34-59, 2021.

[53] J. Xu, L. Chen and C. Ni, "Effect of vibratory weld conditioning on the residual stresses and distortion in multipass girth-butt welded pipes," *International Journal of Pressure Vessels and Piping,* vol. 84, no. 5, pp. 298-303, 2007.

[54] D. L. Rao, Z. Q. Zhu, L. G. Chen and C. Ni, "Reduce the Residual Stress of Welded Structures by Post-Weld Vibration," *Materials Science Forum,* Vols. 490-491, pp. 102-106.

[55] J. R. Cho, B. Y. Lee, Y. H. Moon and C. J. Van Tyne, "Investigation of residual stress and post weld heat treatment of multi-pass welds by finite element method and experiments," *Journal of Materials Processing Technology,* Vols. 155-156, pp. 1690-1695, 2004.

[56] S. Roy, J. W. Fisher and B. T. Yen, "Fatigue resistance of welded details enhanced by ultrasonic impact treatment (UIT)," *International Journal of Fatigue,* vol. 25, no. 9-11, pp. 1239-1247, 2003.

[57] M. J. Jose, S. S. Kumar and A. Sharma, "Vibration assisted welding processes and their influence on quality of welds," *Science and Technology of Welding and Joining,* vol. 21, no. 4, pp. 243-258, 2016.

[58] R. Tamasgavari, A. R. Ebrahimi, S. M. Abbasi and A. R. Yazdipour, "The effect of harmonic vibration with a frequency below the resonant range on the mechanical properties of AA-5083-H321 aluminum alloy GMAW welded parts," *Materials Science & Engineering 736,* pp. 248-257, 2018.

[59] J. Kalpana, P. S. Rao and P. G. Rao, "Influence of Amplitude on the Tensile Strength of Welded Joints Fabricated under Vibratory Weld Conditioning," *Journal of Mechanical Engineering Research and Developments,* vol. 39, no. 3, pp. 757-762, 2016.

[60] C. R. Cunnigham, J. Wang, V. Dhokia, A. Shrokani and S. T. Newman, "Characterization of Austenitic 316LSi Stainless Steel Produced by Wire Arc Additive Manufacturing with

Interlayer Cooling," in *International Solid Freeform Fabrication Symposium - An Additive Manufacturing Conference Proceedings*, Austin, 2019.

[61] L. Hagen, Z. Yu, A. Clarke, A. Clarke, S. Tate, A. Petrella and J. Klemm-Toole, "High deposition rate wire-arc directed energy deposition of 316L and 316LSi: Process exploration and modelling," *Materials Science and Engineering A,* vol. 880, no. 145044, 2023.

[62] Y. Li , Y. Luo, J. Li, D. Song, B. Xu and X. Chen, "Ferrite formation and its effect on deformation mechanism of wire arc additive manufactured 308 L stainless steel," *Journal of Nuclear Materials 550,* no. 152933, 2021.

[63] Y. Kok, X. P. Tan, P. Wang, M. L. S. Nai, N. H. Loh, E. Liu and S. B. Tor, "Anisotropy and heterogeneity of microstructure and mechanical properties in metal additive manufacturing: A critical review," *Materials and Design,* vol. 139, pp. 565-586, 2018.

[64] M. Rappaz and J. A. Dantzig, Solidification, EPFL Press, 2009.

[65] C. Wang, P. Zhu, F. Wang and Y. H. Lu, "Anisotropy of microstructure and corrosion resistance of 316L stainless steel fabricated by wire and arc additive manufacturing," *Corrosion Science,* vol. 206, no. 110549, 2022.

[66] A. A. Antonysamy, J. Meyer and P. B. Prangnell, "Effect of build geometry on the β-grain structure and texture in additive manufacture of Ti6Al4V by selective electron beam melting," *Materials Characterization,* vol. 84, pp. 153-168, 2013.

[67] M. Rabiei, A. Palevicius, A. Dashti, S. Nasiri, A. Monshi, A. Vilkauskas and G. Janusas, "Measurement Modulus of Elasticity Related to the Atomic Density of Planes in Unit Cell of Crystal Lattices," *Materials,* vol. 13, no. 4380, 2020.

[68] B. Hutchinson, M. Malmstrom, J. Lonnqvist, P. Bate, H. Ehteshami and P. Korzhavyi, "Elasticity and wave velocity in fcc iron (austenite) at elevated temperatures – Experimental verification of ab-initio calculations," *Ultrasonics,* vol. 87, pp. 44-47, 2018.

[69] A. R. H. Midawi, N. Huda, C. H. M. Simha and A. P. Gerlich, "Characterization of anisotropy of strength in API-X80 line pipe welds through instrumented indentation," *Mteallography, Microstructure, and Analysis,* vol. 9, pp. 884-894, 2020.

[70] E. B. F. Dos Santos, L. H. Kuroiwa, A. F. C. Ferreira, R. Pistor and A. P. Gerlich, "On the visualization of gas metal arc welding plasma and the relationship between arc length and arc voltage," *Applied Sciences,* vol. 7, no. 503, 2017.

[71] Z. Brytan, W. Borek and T. Tanski, "Introductory chapter: Why austenitic stainless steels are continuously interesting for science?," in *Austenitic Stainless Steels - New Aspects*, IntechOpen, 2017.

[72] L. P. Belotti, J. A. W. van Dommelen, M. G. D. Geers, C. Goulas, W. Ya and J. P. M. Hoefnagels, "Microstructural characterisation of thick-walled wire arc additively manufactured stainless steel," *Journal of Materials Processing Tech.,* 2022.

[73] X. Chen, J. Li, X. Cheng, B. He, H. Wang and Z. Huang, "Microstructure and mechanical properties of the austenitic stainless steel 316L fabricated by gas metal arc welding," *Materials Science & Engineering A 703,* pp. 567-577, 2017.

[74] L. Wang, J. Xue and Q. Wang, "Correlation between arc mode, microstructure, and mechanical properties during wire arc additive manufacturing of 316L stainless steel," *Materials Science and Engineering A,* vol. 751, pp. 183-190, 2019.

[75] C. Wang, T. G. Liu, P. Zhu, Y. H. Lu and T. Shoji, "Study on microstructure and tensile properties of 316L stainless steel fabricated by CMT wire and arc additive manufacturing," *Materials Science & Engineering A,* 2020.

[76] B. E. Carroll, A. T. Palmer and A. M. Beese, "Anisotropic tensile behavior of Ti-6Al-4V components fabricated with directed energy deposition additive manufacturing," *Acta Materialia,* vol. 87, pp. 309-320, 2015.

[77] "Selecting The Right Seam Tracking Solution," Bancroft Engineering, [Online]. Available: https://bancrofteng.com/selecting-right-seam-tracking-solution/. [Accessed February 2024].

[78] A. R. H. Midawi, N. Huda, C. H. M. Simha and A. P. Gerlich, "Characterization of anisotropy of strength in API-X80 line pipe welds through instrumented indentation," *Mteallography, Microstructure, and Analysis,* vol. 9, pp. 884-894, 2020.

Appendices

Appendix A: Chapter 4 Data

Stress Strain Curves of Individual Samples With 0.2 % Offset for Yield Strength

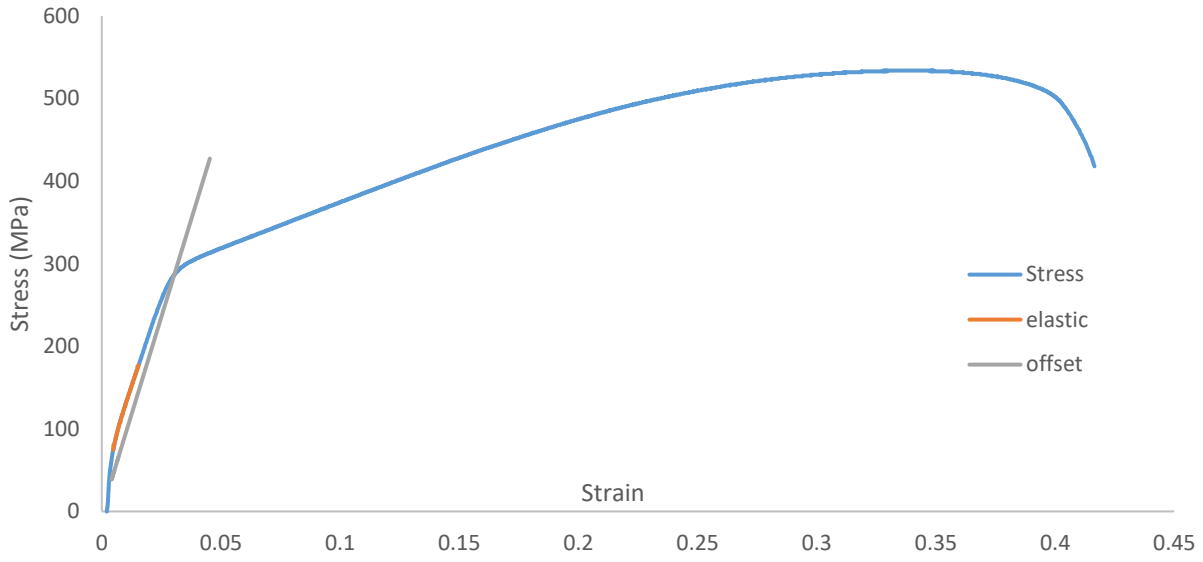

Stress strain curve of sample B1

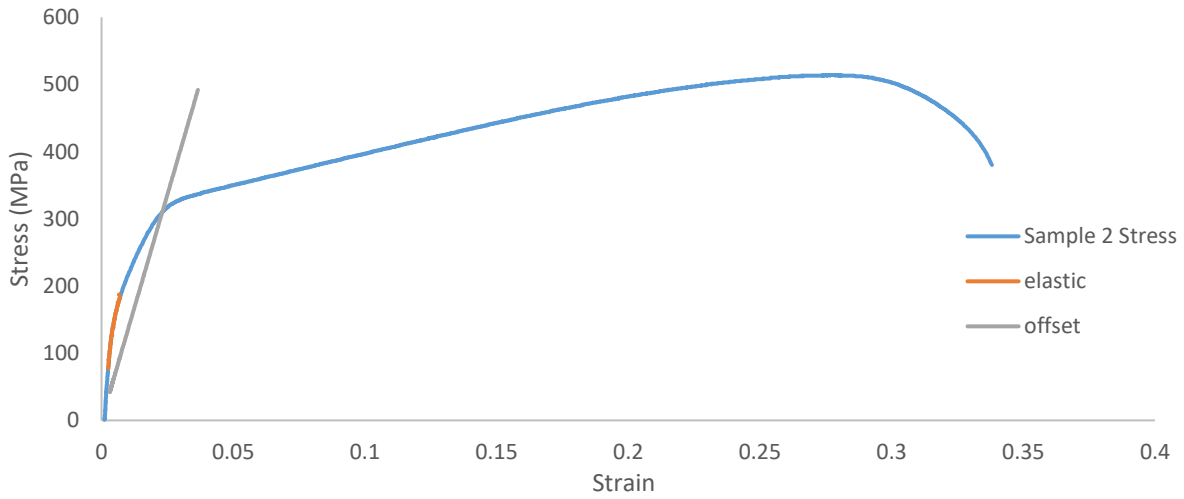

Stress strain curve of sample B2

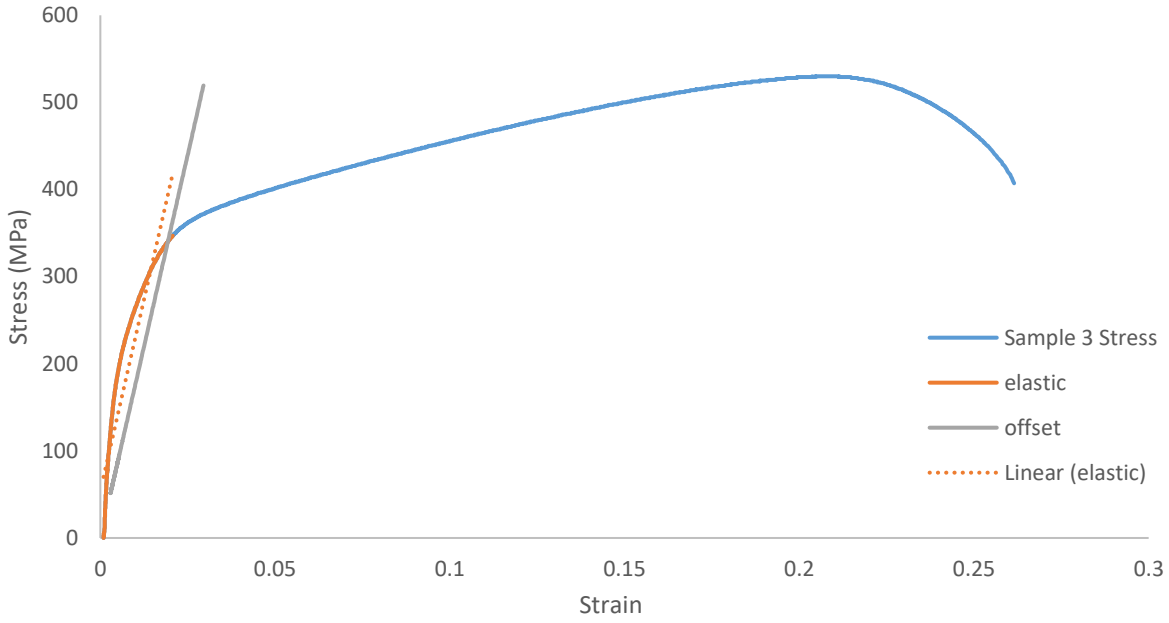

Stress strain curve of sample B3

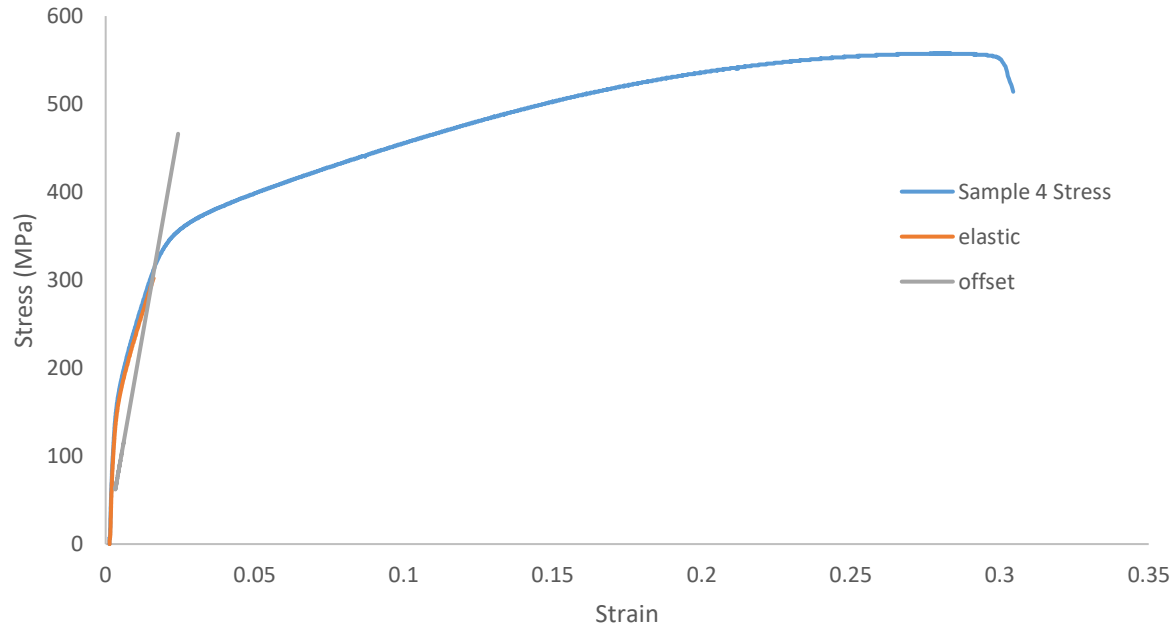

Stress strain curve of sample T1

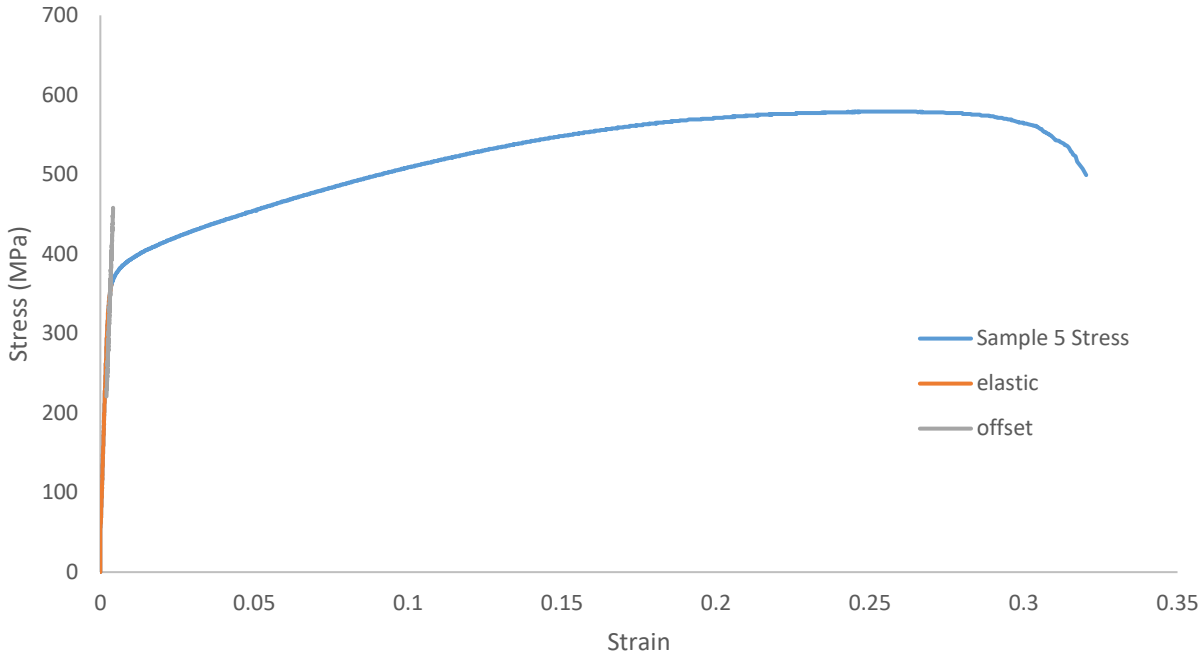

Stress strain curve of sample T2

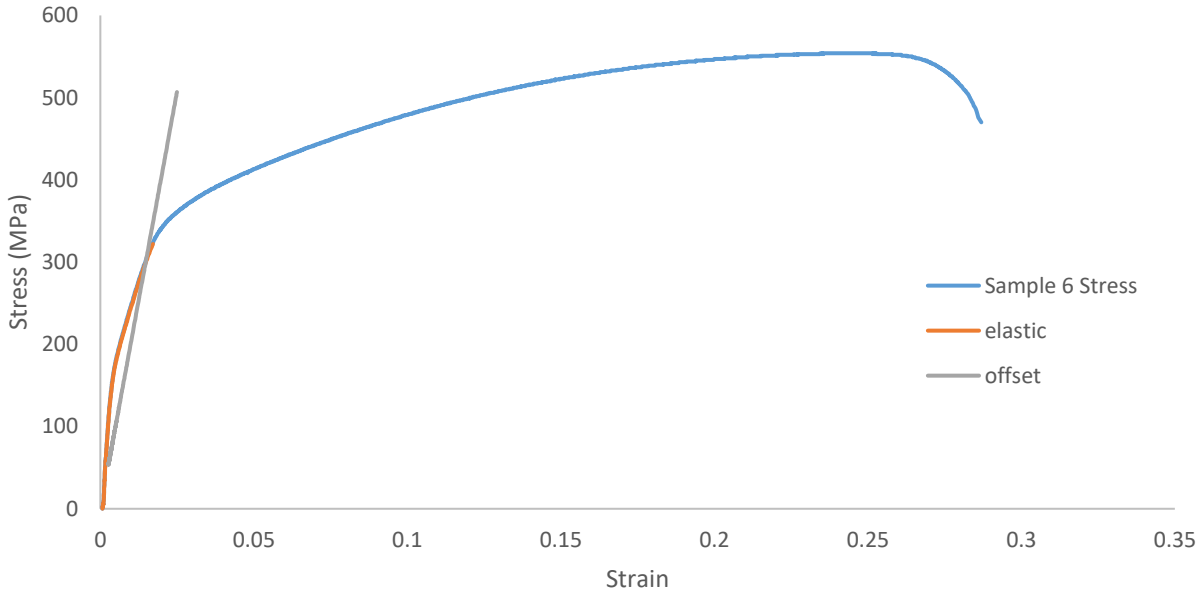

Stress strain curve of sample T3

Mechanical properties of individual samples

Sample	B1	B2	B3	T1	T2	T3
Modulus of Elasticity (GPa)	71.30	81.54	85.64	106.7	126.9	82.10
Yield Strength (MPa)	290	318	340	302	341	282
Ultimate Tensile Strength (MPa)	534	514	530	558	579	554
Elongation	0.416	0.338	0.261	0.304	0.319	0.287

Appendix B: Chapter 5 Data

Stainless Steel Samples: MATLAB Code for SDAS Plots

```
clc
clear all

Frequency=[55 70 82 95];
Distance=[3500 600];

%Amplitude 0.5 V
SDAS_600_05=[14.14 15.02 13.20 16.28];
SDAS_3500_05=[7.64 10.90 8.80 8.45];

%Amplitude 1.0 V
SDAS1=[10.27 12.82; 9.67 17.43; 10.18 9.48];
SDAS_600_1=[12.82 13.20 17.43 9.48];
SDAS_3500_1=[10.27 9.44 9.67 10.18];

figure(1)
plot(Frequency, SDAS_600_05,'r-
','LineWidth',2,'Marker','o','MarkerSize',5,'MarkerFaceColor','k','MarkerEdgeColor','
k')
hold on
plot(Frequency, SDAS_3500_05,'b-
','LineWidth',2,'Marker','o','MarkerSize',5,'MarkerFaceColor','k','MarkerEdgeColor','
k')
legend('600 um distance','3500 um distance','Position',[0.25 0.75 0.1
0.2],'Orientation','vertical',FontSize=9,Box='off',TextColor='k')
xlabel('Frequency (Hz)')
ylabel('Average SDAS (um)')

xlim([45 100])

figname = ['0.5 V Amplitude' '.jpg'];
exportgraphics(figure(1),figname,'Resolution',600);

figure(2)
plot(Frequency, SDAS_600_1,'r-
','LineWidth',2,'Marker','o','MarkerSize',5,'MarkerFaceColor','k','MarkerEdgeColor','
k')
hold on
```

```
 plot(Frequency, SDAS_3500_1,'b-
','LineWidth',2,'Marker','o','MarkerSize',5,'MarkerFaceColor','k','MarkerEdgeColor','
k')
 legend('600 um distance','3500 um distance','Position',[0.25 0.75 0.1
0.2],'Orientation','vertical',FontSize=9,Box='off',TextColor='k')
 xlabel('Frequency (Hz)')
 ylabel('Average SDAS (um)')

 xlim([45 100])

 figname = ['1.0 V Amplitude' '.jpg'];
 exportgraphics(figure(2),figname,'Resolution',600);
```

Titanium Samples: MATLAB Code for Average Grain Size Plots

```
 clc
 clear all

 %Distances from substrate considered: 400 and 3000 um

 Frequency=[50 63 75 88];

 %Amplitude of 0.5 V
 Grain_400_05=[413 468 487 422];
 Grain_3000_05=[614 749 637 735];

 %Amplitude of 1.0 V
 Grain_400_1=[473 437 462 511];
 Grain_3000_1=[830 730 875 860];

 %Amplitude of 1.25 V
 Grain_400_125=[336 496 499 566];
 Grain_3000_125=[644 733 784 558];

 figure(1)
 plot(Frequency, Grain_400_05,'r-
','LineWidth',2,'Marker','o','MarkerSize',5,'MarkerFaceColor','k','MarkerEdgeColor','
k')
 hold on
 plot(Frequency, Grain_3000_05,'b-
','LineWidth',2,'Marker','o','MarkerSize',5,'MarkerFaceColor','k','MarkerEdgeColor','
k')
 legend('400 um distance','3000 um distance','Position',[0.7 0.7 0.1
0.2],'Orientation','vertical',FontSize=9,Box='off',TextColor='k')
```

```
 xlabel('Frequency (Hz)')
 ylabel('Average Grain Size (um)')
 ylim([300 950])
 xlim([45 95])

 figname = ['0.5 V Amplitude' '.jpg'];
 exportgraphics(figure(1),figname,'Resolution',600);

 figure(2)
 plot(Frequency, Grain_400_1,'r-
','LineWidth',2,'Marker','o','MarkerSize',5,'MarkerFaceColor','k','MarkerEdgeColor','
k')
 hold on
 plot(Frequency, Grain_3000_1,'b-
','LineWidth',2,'Marker','o','MarkerSize',5,'MarkerFaceColor','k','MarkerEdgeColor','
k')
 legend('400 um distance','3000 um distance','Position',[0.7 0.5 0.1
0.2],'Orientation','vertical',FontSize=9,Box='off',TextColor='k')
 xlabel('Frequency (Hz)')
 ylabel('Average Grain Size (um)')
 ylim([300 950])
 xlim([45 95])

 figname = ['1.0 V Amplitude' '.jpg'];
 exportgraphics(figure(2),figname,'Resolution',600);

 figure(3)
 plot(Frequency, Grain_400_125,'r-
','LineWidth',2,'Marker','o','MarkerSize',5,'MarkerFaceColor','k','MarkerEdgeColor','
k')
 hold on
 plot(Frequency, Grain_3000_125,'b-
','LineWidth',2,'Marker','o','MarkerSize',5,'MarkerFaceColor','k','MarkerEdgeColor','
k')
 legend('400 um distance','3000 um distance','Position',[0.7 0.7 0.1
0.2],'Orientation','vertical',FontSize=9,Box='off',TextColor='k')
 xlabel('Frequency (Hz)')
 ylabel('Average Grain Size (um)')
 ylim([300 950])
 xlim([45 95])

 figname = ['1.25 V Amplitude' '.jpg'];
 exportgraphics(figure(3),figname,'Resolution',600);
```

Appendix C: Chapter 6 Data

Generic MATLAB Code for all AVC Parameter Plots

```
close all
clear all
format short
%Insert file name here (must be .xlsx)
runnum='AVC Gain 1.2 Sp 50';
filename = [runnum '.xlsx'];
%Choose row at which data will start to load
ndata = readmatrix(filename,'NumHeaderLines',42);
```

Gain 1.0

```
beadgain1length=227;
timeg1 = ndata(:,3);
v_commandg1 = ndata(:,12);
v_telemetryg1 = ndata(:,14);
z_positiong1 = ndata(:,62);

%Measured Bead Heights for all gains and max speeds
beadhg11=[4.62 4.82 4.72 4.80 4.92 4.96 4.80 4.94 4.76 4.71 5.05 4.78 4.65 4.82 4.74
4.82 4.78 4.82 4.62 4.76 4.77 4.80 4.75]; %Gain 1.0
beadhg12=[6.38 6.42 6.32 6.36 6.90 6.50 6.67 6.53 6.50 6.46 6.54 6.62 6.62 6.74 6.62
6.57 6.70 6.56 6.50 6.52 6.54 6.68 6.34]; %Gain 1.2
beadhg08=[5.96 5.56 5.78 5.94 6.04 6.06 6.12 6.10 6.05 6.06 6.20 6.28 6.1 6.14 5.95
6.16 5.9 5.95 5.72 5.95 6.04 6.02 6.12]; %Gain 0.8
beadhg35=[7.77 7.56 7.46 7.51 7.6 7.56 7.64 7.68 7.61 7.78 7.98 7.88 7.79 7.89 7.96
8.04 7.97 7.74 7.76 7.79 7.60 7.68 7.80]; %MS=35 mm/min
beadhg50=[7.28 6.94 7.24 7.06 7.16 7.28 7.40 7.38 7 7.22 7.65 7.45 7.30 7.50 7.68
7.56 7.40 7.14 7.12 7.26 7.10 7.12 7]; %MS=50 mm/min
beadhg65=[8.04 7.72 7.60 7.62 7.50 7.80 7.74 7.84 7.75 7.74 7.82 7.70 7.70 7.66 7.90
7.70 7.70 7.88 7.60 7.58 7.62 7.80 7.40]; %MS=65 mm/min

%Set Values of bead height according to parameter desired for testing
beadhg1=beadhg11;

min_z=min(z_positiong1);
z_positiong1 = z_positiong1-min_z;
g1length=[14.25 26.2 34.55 43.5 52 62.35 68.6 76.4 81.2 87.3 98 109 118 129 140 150
159 169 179 190 199 207 217];
g1time=timeg1(1)+(g1length/(beadgain1length/(timeg1(end)-timeg1(1))));
```

```
nofmeasurements=23;

Index_1n=zeros(nofmeasurements,1);
for i=1:nofmeasurements
    for j=1:(length(timeg1)-1)
        if (abs(g1time(i)-timeg1(j))) < 0.1
            if ((abs(g1time(i)-timeg1(j))) > (abs(g1time(i)-timeg1(j+1)))) &&
((abs(g1time(i)-timeg1(j+1))) < 0.1)
            Index_1n(i)=j+1;
            continue
            end
        Index_1n(i)=j;
        else
            continue
        end
    end
end

Zmeasured=zeros(1,nofmeasurements);

for i=1:1:nofmeasurements
    Zmeasured(i)=z_positiong1(Index_1n(i));
end
```

Plots

```
MainFig1=tiledlayout('flow','TileSpacing','tight','Padding','tight');
set(gcf,'units','inches','position',[1,1,6,4])

nexttile([4 12]);
set(gca,'FontSize',8,'color','w')
ax1=gca;
xax = ax1.XAxis;
ax1.XColor = 'k';
set(xax,'TickDirection','out')
ax1.LineWidth=0.3;
xlabel('Time (s)','FontSize',10);

yyaxis left
plot(timeg1,v_commandg1,'Color',[0.5 0.5 0.5])
xlim([0 200]);
ax1.YColor = 'r';
hold on
plot(timeg1,v_telemetryg1,'r-')
ylabel('Volatge Telemetry (V)','Color','r','FontSize',10);
```

```
 ylim([18 24]);

 note1 = "Gain 1.0";
 text(120,23.75,note1,"HorizontalAlignment","right","VerticalAlignment","bottom")

 yyaxis right

 g1fit = fit(timeg1,z_positiong1,'poly2');
 plot(g1fit,timeg1,z_positiong1,'b-')

 hold on
 plot(g1time,beadhg1,'k-o',MarkerSize=3,MarkerFaceColor='k')
 hold on
 avgbhg1=mean(beadhg1);
 bhg1_error=beadhg1-avgbhg1;
 avgbhg1_line=yline(avgbhg1,'--',['Average Measured Height = ' [num2str(avgbhg1)]
'mm'],'Fontsize',4.5,'Color',[0.5 0.5 0.5],
'LineWidth',0.25,'LabelVerticalAlignment','top','LabelHorizontalAlignment','right');
 avgbhg1_line.Annotation.LegendInformation.IconDisplayStyle = 'off';
 hold on

 cor_bhg1=g1fit.p1.*g1time.*g1time+g1fit.p2.*g1time+g1fit.p3;
 cor_bhg1=avgbhg1+cor_bhg1;
 for i=1:nofmeasurements
     cor_bhg1(i)=cor_bhg1(i)+bhg1_error(i);
 end

 plot(g1time,cor_bhg1,'b-o',MarkerSize=3,MarkerFaceColor='b')

 ylim ([0 14])
 ax1.YColor = 'b';
 ylabel('Z Position and Bead Height (mm)','Color','b','FontSize',10);

 xlabel('Time (s)','FontSize',10);
 legend({'Voltage Command','Voltage Telemetry','Z Position','Fit','Bead
Height','Corrected Bead Height'},'Position',[0.75 0.25 0.1
0.2],'Orientation','vertical',FontSize=6,Box='off',TextColor='k')

 figname = ['FigRun' num2str(runnum) '.jpg'];
 exportgraphics(MainFig1,figname,'Resolution',600);


 MainFig2=tiledlayout('flow','TileSpacing','tight','Padding','tight');
 set(gcf,'units','inches','position',[1,1,6,4])

 nexttile([4 12]);
```

```
 set(gca,'FontSize',8,'color','w')
 ax1=gca;
 xax = ax1.XAxis;
 ax1.XColor = 'k';
 set(xax,'TickDirection','out')
 ax1.LineWidth=0.3;
 xlabel('Time (s)','FontSize',10);

 regtab=[cor_bhg1' Zmeasured'];
 regtab=sortrows(regtab,1);

 scatter(regtab(:,1), regtab(:,2),'k','filled')

 [p,S] = polyfit(regtab(:,1),regtab(:,2),1);
 [y_fit,delta] = polyval(p,regtab(:,1),S);

 hold on
 plot(regtab(:,1),y_fit,'r')
 plot(regtab(:,1),y_fit+2*delta,'b--',regtab(:,1),y_fit-2*delta,'b--')
 note2 = "Gain 1.0; R = 0.96";
 text(max(cor_bhg1),min(Zmeasured),note2,"HorizontalAlignment","right","VerticalAlign
ment","bottom")

 ax1.YColor = 'k';
 ylabel('Z Position (mm)','Color','k','FontSize',10);
 xlabel('Corrected Measured Bead Height (mm)','FontSize',10);
 legend({'Data','Linear Fit','95% Prediction
Interval'},'Location','northwest','Orientation','vertical',FontSize=6,Box='off',TextC
olor='k')

 figname = ['FigRun' num2str(runnum) 'Scatter.jpg'];
 exportgraphics(MainFig2,figname,'Resolution',600);
```

AVC Step Responses MATLAB Code

```
clc
clear all

format short
runnum1='AVC Gain 1.0 Sp 50';
runnum12='AVC Gain 1.2 Sp 50';
runnum08='AVC Gain 0.8 Sp 50';
filename1 = [runnum1 '.xlsx'];
filename12 = [runnum12 '.xlsx'];
filename08 = [runnum08 '.xlsx'];

ndata1 = readmatrix(filename1,'NumHeaderLines',42);
ndata12 = readmatrix(filename1,'NumHeaderLines',43);
ndata08 = readmatrix(filename1,'NumHeaderLines',42);

time_1 = ndata1(:,3);
v_comm1 = ndata1(:,12);
v_telem1 = ndata1(:,14);
z_1 = ndata1(:,62);

time_12 = ndata1(:,3);
v_comm12 = ndata1(:,12);
v_telem12 = ndata1(:,14);
z_12 = ndata1(:,62);

time_08 = ndata1(:,3);
v_comm08 = ndata1(:,12);
v_telem08 = ndata1(:,14);
z_08 = ndata1(:,62);

%Plot for G=1.0
figure(1)

yyaxis left
plot(time_1, Z_1,'b')
xlim([10 140])
ylim([0 2.5])

ax1=gca;
ax1.YColor = 'b';
ylabel('Z Position (mm)','Color','b','FontSize',10);

hold on
yyaxis right
```

```
 plot(time_1, V_telem1, 'r-');

 ax2=gca;
 ax2.YColor = 'r';
 ylabel('Voltage','Color','r','FontSize',10);

 xlabel('time (s)')
 yyaxis right
 plot (time_1, V_comm1,'k-')
 ylabel ('Voltage (V)')
 ylim ([19 23])
 legend('Z Position', 'Voltage telemetry', 'Voltage command','Position',[0.7 0.7 0.2
0.2],'Orientation','vertical',FontSize=6,Box='off',TextColor='k')

 figname = ['Step Response G=1.0','.jpg'];
 exportgraphics(figure(1),figname,'Resolution',600);

 %Plot for G=0.8
 figure(2)

 yyaxis left
 plot(time_08, Z_08,'b')
 xlim([10 140])
 ylim([0 2.5])
 ylabel('Z position (mm)')

 ax1=gca;
 ax1.YColor = 'b';
 ylabel('Z Position (mm)','Color','b','FontSize',10);

 hold on
 yyaxis right

 plot(time_08, V_telem08, 'r-')
 xlabel('time (s)')

 ax2=gca;
 ax2.YColor = 'r';
 ylabel('Voltage','Color','r','FontSize',10);

 yyaxis right
 plot (time_08, V_comm08,'k-')
 ylabel ('Voltage (V)')
 ylim ([19 23])
 legend('Z Position', 'Voltage Telemetry', 'Voltage Command','Position',[0.7 0.7 0.2
0.2],'Orientation','vertical',FontSize=6,Box='off',TextColor='k')
```

```
figname = ['Step Response G=0.8','.jpg'];
exportgraphics(figure(2),figname,'Resolution',600);

%Plot for G=1.2
figure(3)

yyaxis left
plot(time_12, Z_12,'b')
xlim([10 140])
ylim([0 2.5])
ylabel('Z position (mm)')

ax1=gca;
ax1.YColor = 'b';
ylabel('Z Position (mm)','Color','b','FontSize',10);

hold on
yyaxis right
plot(time_12, V_telem12, 'r-')

ax2=gca;
ax2.YColor = 'r';
ylabel('Voltage','Color','r','FontSize',10);

xlabel('time (s)')
yyaxis right
plot (time_12, V_comm12,'k-')
ylabel ('Voltage (V)')
ylim ([19 23])
legend('Z Position', 'Voltage Telemetry', 'Voltage Command','Position',[0.7 0.7 0.2
0.2],'Orientation','vertical',FontSize=6,Box='off',TextColor='k')

figname = ['Step Response G=1.2','.jpg'];
exportgraphics(figure(3),figname,'Resolution',600);
```